# The Effect of State of Charge and Charge Rate on the Formation and growth Deposit Layer on the Anode Electrode of the Lithium Ion Battery

by

Victor Anafo Agubra

A dissertation submitted to the Graduate Faculty of
Auburn University
in partial fulfilment of the
requirements for the degree of
Doctor of Philosophy

Auburn, Alabama
December 13, 2014

Keywords: Lithium ion batteries, graphite anode, electrolyte decomposition

Approved by

Jeffrey W. Fergus, Professor of Materials Engineering
Song-Yul (Ben) Choe, Professor of Mechanical Engineering
Bart C. Prorok, Professor of Materials Engineering
ZhongYang Cheng (Z.Y), Professor of Materials Engineering

# Abstract

The lithium ion battery technology has for the past two decades received a lot of attention because of its high energy density and excellent cycle life compared to other battery chemistries such as lead acid and Ni-Cd. These attributes of the lithium ion battery have positioned it as the preferred portable energy source for most consumer appliances and for electric/hybrid electric vehicles. However, several reported battery failures during its operation, have raised some safety concerns. These failures of the lithium ion batteries are linked to the degradation of its components: electrodes, current collectors, separator and electrolyte. In particular, the carbon-based anode has been associated with many aging mechanisms. The formation of the solid electrolyte interphase (SEI) layer on the surface of the anode electrode prevents further electrolyte decomposition reaction, however, at certain battery operating parameters the SEI breakdown gives way to more electrolyte solvent and salt decomposition reactions to form several species that are non-uniform and electronically insulating on the anode electrode.

The research described in this dissertation focuses on investigating the effect of battery potential and charge rate on the decomposition reaction on the anode electrode of a lithium ion polymer battery. This relationship is important for understanding how charging protocols are related to performance degradation. The investigation showed that at high potential and charge rate the metastable species $ROCO_2Li$ within the SEI layer decomposes into more stable compounds –$Li_2CO_3$ and LiF. This therefore created a defective SEI structure thereby exposing the graphite surface to more electrolyte decomposition reaction. The overall impedance of batteries increased, particularly the charge transfer resistance. This was attributed to deposit layer formed at the electrode/electrolyte interface which affected the lithium intercalation kinetics at the interface. A direct link between the capacity fade during cycling and the progressive deposit layer thickness growth resulting from side reaction at the anode was established.  Analysis of the crystal structure of the graphite electrode showed an increasing amount of lithium residing in the graphite sheets as the batteries are aged at higher SOC. The “trapped” lithium in the crystal structure of the graphite led to reduction/isolation of recyclable lithium taking part in the electrochemical process.

Cycling the batteries at high charge rate of 4C induce some stresses in the electrode matrix during the intercalation/de-intercalation process that led to loss and isolation of carbon particles from the current collector that could make these particles electrochemically inactive. At high potential, the depletion of the recyclable lithium via trapping of lithium in the crystal structure of the graphite, deposit layer formation, and the partial loss of graphite active materials were predominant regardless of the charge rate and these factors contributed to the high capacity loss of the lithium ion batteries.

# Acknowledgement

The author wish to express his sincere thanks and deepest gratitude to Dr. Jeffrey Fergus for his constant, day-to-day support and guidance, and invaluable advice rendered throughout this study. The author extends special thanks to the members of his advisory committee, Drs. Song-yul Choe, Bart Prorok, Zhongyang Chen for their invaluable critique and support that help shape this dissertation, in particular Dr. Choe for providing me with funding, unlimited access to his laboratory, and the numerous opportunities he provided me in the various fora. It worth mentioning that without his support this research would not have seen the light of day. Special gratitude is expressed to his wife,- Joycelyn Apepeh and daughter Asumbono Alexis, parents and siblings for their understanding and encouragement during the extended time over which this work took place. Special thanks My battery research group mates : Xuayan Li, Yinyin Zhao and Meng Xiao and most specially Rujian Fu, who carried out all the battery cycling test ; and lastly to the following people: Honglong Wang, Zhizhi, Naved, Patrick, and Maryanne for all the assistance and friendship they provided. The author would also like to thank special persons for their support and day-to-day assistance: Mr. Steve Moore and Mike Crumpler. Finally, the author would like to acknowledge the support from the General Motor company for providing the batteries and funding for this research.

# Table of Contents

## List of Figures

# List of Tables

# Chapter 1

# Introduction

## 1.0 Background

In the early twentieth century, nickel-cadmium, alkaline, and lead acid batteries were the popular portable energy batteries. However, the advent of the lithium ion battery (LIB) in the late twentieth century has become the fastest growing and most promising battery chemistry.  The high energy/ power density (typically twice that of the standard nickel-cadmium batteries), and excellent cycle life of the lithium ion battery have positioned it as the preferred portable energy source for most consumer appliances and in the automotive industry for electric vehicles (EV) and hybrid electric vehicles (HEV). However, several reported batteries failures during its application have raised concerns about its safety that has fast become a major concern for its wide application. The performance of the LIB depends on the development of materials for the various components of the LIB [1-3]. The degradation of these components during operation adversely affects the energy delivery of the LIB.

## 1.1 Motivation for Research

Charging the LIB with high currents aimed at reducing the battery charging time rather present a lot of challenges. High charge rate can cause large amount of lithium deposition on the anode electrode surface. This large amount of $Li^+$ may exceed the rate at which the $Li^+$ can intercalate into the anode material crystal structure. When this condition rises, the $Li^+$ may deposit as metallic lithium on the surface of the anode. The metallic lithium will react with the electrolyte and form a surface film layer.

The formation of this surface film layer on the anode results in partial consumption lithium ion in the LIB, thereby reducing the amount lithium involved in the electrochemical process [4-6]. In addition, the formed surface layer on the anode could clog pores on the carbon anode electrode that may limit the accessibility of lithium ions into the anode surface [7, 8] that could lead to an increased in the charge transfer/Ohmic resistance, and overall impedance of the battery [9-11]. This surface layer affects the electrochemical reaction on the surface of the anode and thus impacts on the reversible capacity of the LIB.

This research is motivated by the need to cycle the battery in an appropriate potential window and charge rate without inducing injurious degradation mechanisms that could cause the built-up of the surface layer deposited on the anode electrode and in the worst case, initiate lithium plating - that tends to affect the energy delivery of the lithium ion battery. This study will be helpful in understanding how charging protocols are related to performance degradation. This will aid in the development of an optimum charge/discharge protocol, as well establishing the state of charge range for cycling the LIB that will minimize the formation of the surface film layer on the anode of electrode that is a source of recyclable lithium ion loss.

## 1.2 Objectives of the Research

The overall objective of this research is aimed determining how potential and charge rate influence the decomposition reaction on the anode electrode. Lithium ion batteries employ porous electrodes to increase the active area between the electrolyte and the active carbon particles to facilitate the electrochemical reactions process. Electrolyte decomposition side reaction deposit a surface layer on the surface of the active carbon materials, which clogs the pores of the electrode. The blocking of the electrode pores by the growing surface layer on the electrode thus affects the electrochemical energy conversion process, resulting in a rise in the charge transfer resistance, Ohmic resistance, and the SEI film resistance culminating into the overall batteries impedance.

The hypothesis is that a high battery potential during charging creates a region of high polarization on the surface of the anode electrode. At this region of high polarization, the ethylene carbonate (EC) two-electron reduction kinetics on the graphite –particles follow the Butler-like kinetics equation.

During the battery charging process, the reaction rate occurring on the surface of the anode is proportional to the migration and concentration of lithium ions. Through this process, the anode potential is raised thus subjecting the electrode to polarization and passivation reaction. Therefore a high charge rate coupled with a high electrode potential will accelerate the passivation reaction resulting in the formation of the surface layer. The solid electrolyte interphase (SEI) layer formed from the initial electrolyte decomposition at the battery fabrication (formation stages), allows $Li^+$ intercalation into the graphite structure even if the carbon electrode potential is lower than the electrolyte decomposition potentials and thus prevents further electrolyte decomposition,. The SEI layer, however, becomes ineffective as the battery is cycled at high potential and charge rate. The initial thickness of the SEI layer which is initially about 3nm [12, 13] increases during use and thus become ineffective at preventing further electrolyte decomposition reactions. Therefore exposes the graphite electrode to more electrolyte reduction reaction. A series of electrochemical tests were designed to evaluate this hypothesis.

Electrochemical data such as; the battery capacity fade, the overall battery impedance, the

Ohmic, SEI film, and double layer capacitance were extracted from the equivalent circuit model after the electrochemical cycling of the LIB.  A postmortem analysis of the anode electrode was carried out and included a quantitative analysis of the thickness of the formed surface layer using analytical tools such as SEM. The composition and amount of the compounds constituting the surface film layer formed on the carbon particles was analyzed using complementary tools such as the Fourier Transform infrared spectroscopy (FTIR) and X-ray photoelectron spectroscopy.

### 1.3 Dissertation Organization

This dissertation consists of seven chapters. The first chapter is an introduction that gives an initial overview of the dissertation and includes the objectives and motivation to undertake the investigation into the subject of this dissertation. The second chapter reviews the literature on the subjects closely related to the dissertation that include subject areas such as: lithium ion battery fundamentals, lithium ion intercalation into the carbon anode electrode, and batteries degradation mechanisms. In the third chapter, the experimental details for each of the process and procedures used to successfully carry out the entire investigation. The results/discussion of the effect of state of charge on the formation and growth of the deposit layer and its influence on the batteries capacity are discussed into detail in chapter 4, while that of the charging current is presented in chapter 5.  The conclusion and discussion of the effect of both potential and charge rate are presented in chapter 6, while the recommendations for future works are discussed in chapter 7.

# Chapter 2

# Literature Review

## 2.0 Lithium- ion Battery Fundamentals

The lithium-ion polymer battery is made of many layers in series. One layer consist of several components namely; anode and cathode electrodes, two current collectors, copper and aluminum for the anode and cathode electrodes respectively, the separator, electrolyte, and binder material. Carbon is the most commonly used material for the anode electrode while the cathode electrode mainly consist metal oxides such as manganese, nickel, cobalt, Iron, titanium, chromium, etc. There is still active research on the electrode materials and new electrode materials are added periodically to this list. At the early stage of the LIB development, polyvinylidene fluoride (PVDF) was commonly used for the binding materials for the anode electrode [3]. However, styrene-butadiene copolymer (SBR) has become more popular. The binding materials are generally used to either bind the active materials of the electrodes or between active materials layers and the current collectors. One of the requirements of the binding agent is for it to be an oxidation-resistant especially in an unstable oxidizing environment of the cathode electrode. The separate has a dual function of keeping the anode and cathode apart to prevent them from electrical short-circuiting and allow the rapid transport of ionic charge carriers across the electrodes for electrochemical reaction process. The lithium-ion polymer battery uses a solid polymer electrolyte rather than gel or liquid organic salt solvent. The electrolyte generally is the transport medium completes the electro-chemical circuit by carrying only ions between the active cathode and anode materials. The electrolyte salt, $LiPF_6$ and solvent ethylene carbonate (EC) and dimethyl carbonate (DMC) are commonly used electrolyte.

Charging the LIB causes the $Li^+$ to leave the cathode electrode and enter the lattice structure of the graphite electrode. While during the discharge process, $Li^+$ moves from the anode electrode back to the cathode electrode. This process of ions moving in and out of the interstitial sites of the electrodes is known as intercalation. The term C-rate is a measure of the rate at which a battery is discharged relative to its maximum capacity in an hour. So the amount of charge required to discharge the battery in an hour is defined as 1C. During discharge, $Li^+$ ions diffuse to the surface of carbon particles of the anode electrode where they de-intercalate from the crystal lattice and transfer to an electrolyte solution as shown in Figure 2.1. The positively charged ions travel via diffusion and migrate through the electrolyte solution, where they again react and diffuse into metal oxide active material particles. Electrons produced in the negative electrode reaction are consumed in the positive electrode reaction. These electrochemical reactions are depicted in reaction Equations 3 through 5 below;

Reduction reaction

$$\mathrm{Li_{1-x}MnO_2 + xLi^+ + xe^- \rightarrow LiMnO_2} \tag{3}$$

Oxidation reaction

$$\mathrm{Li_xC_6 \rightarrow xLi^+ + xe^- + 6C} \tag{4}$$

Overall battery reaction

$$\mathrm{Li_{1-x}MnO_2 + C_6Li_x \rightarrow LiMnO_2 + 6C} \tag{5}$$

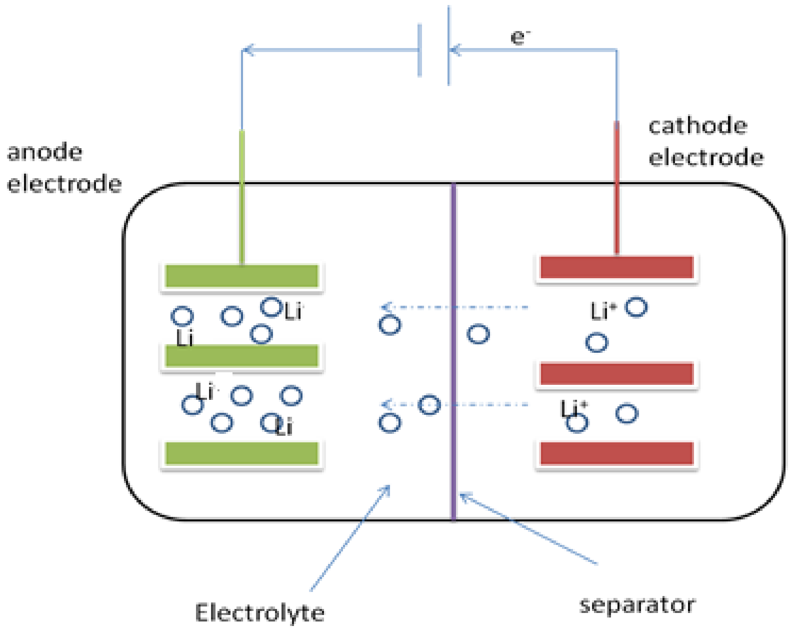

Figure 2.1: Schematic diagram of battery charging process

## 2.1 Carbon Anode Electrode

Its light weight, high voltage and high energy density once made lithium metal the preferred anode electrode for the lithium ion battery. However, the close proximity of the reversible potential of the lithium metal makes it susceptible to lithium plating, moss and dendrite formation during charge cycles [14-16]. In addition, plating/stripping in organic electrolyte solvents make it unsafe due to its high reactivity in these solvents. In place of the lithium metal, graphite and non-graphitizable carbon have gradually replaced it as the preferred anode material for the lithium ion battery because of their high capacity, good cycleability, high conductivity, which depends on; carbon microstructure, potential, and surface morphology of the carbon [18], low thermal expansion, and low electrode potential relative to other anode materials. In addition, the graphite anode generally has a relatively flat potential profile near the redox potential of the Li/Li$^+$ during charge-discharge processes compared to other anode materials that enable lithium intercalation.

The layered structure of graphite makes it suitable for lithium to intercalate/ de-intercalate into the graphite sheet. The lithium intercalation makes graphite intercalation compound (GIC) with a stoichiometry of $Li_xC_6$ with $x \leq 1$[19]. Furthermore the graphite also has both the hexagonal and rhombodedral symmetry in its crystal structure. The rhombodedral symmetry could suppress the exfoliation effect during co-intercalation of solvated Li$^+$ into the graphite layer for the PC electrolyte system [17]. The electrochemical process of lithium ions intercalation into graphite lattices is similar to the under potential deposition process and generally described by the electrochemical reaction:

$$xLi^{+} + 6C + xe^{-} \leftrightarrow L_x iC_6 \qquad (6)$$

This electrochemical reaction is a complex process which involves some phase transition process, related to the staging phenomenon of the GIC. The electrochemical kinetics of this reaction determines the power densities of carbonaceous anode electrode of the lithium battery. During the first electrochemical lithium intercalation reaction, the carbon electrode potential is lower than the electrolyte decomposition potentials, thus causing electrolyte decomposition reaction with the lithium ions to form what is generally referred to as the solid electrolyte interphase (SEI) layer.

## 2.2 Kinetics of Lithium- Ion Intercalation in Carbon Electrode

The random alignment of small-dimensional graphite layers in disordered carbon provides many voids to accommodate lithium. Disordered carbons is classified into two type: soft carbon, whose turbostratic disorder can be removed by heating the carbon at high temperature (3000℃), while that of hard carbon its turbostratic disorder is difficult to remove even at high temperatures. The micropores and defects in soft disordered carbon can retard $Li^+$ diffusion while enhances activation energy. The unfavorable orientation graphite particle leads to sluggishness of $Li^+$ intercalation and inadequate electronic contact between graphite particles and the copper substrate. Sato et al [20] believe that lithium ions occupy the nearest neighbor sites in intercalated carbon, while Tokumitsu et al [21, 22] in their study established that extra lithium ions can resides in the nano-sized cavities of carbon sheets.

When the carbon electrode in LIB is polarized from open circuit voltage (OCV) to low potentials ($Li/Li^+$) in the vicinity of the organic lithium salt and solvent, the processes that take place on the surface of the electrode are as follows; below 2V ($Li/Li^+$) the electrolyte components are reduced. The reduced species $PF_6^-$ from salt $LiPF_6$ and the contaminates on the carbon electrode in the presence of the $Li^+$ ion initiate the formation of an insoluble Li organic and inorganic species which precipitate on the surface of the electrode (SEI layer). The precipitated SEI layer on the surface of the carbon electrode is a Li ion conductor but an insulator to electrons. As the polarization of the carbon electrode continues, this surface film continues to form on the carbon surface until it reaches a thickness that prevents electron tunneling through it. This action stops further electrolyte reduction and passivation of the carbon electrode.

## 2.3 Formation of SEI Layer

The formation of the solid electrolyte interphase (SEI) depends largely on the electrode materials, electrolyte salts, and solvents involved [23-25]. The surface film passivation, which generally follows a classical diffusion-limited process [25], is also influenced by electrolyte additives and the potential window [26-30]. Most electrolyte solvents of high purity have a decomposition potential of 4.6-4.9V vs. $Li/Li^+$, although for lithium ion batteries a potential greater than 5V is desired.

The solvent reduction process generally proceeds either with one-electron [27, 31] or two-electrons [32, 33] transfer between the electrode and the solvent molecules, while that of the salt reduction is initiated by anodic polarization to generate an unstable radical anion [29, 34, 35, 36, 37]. The salt anion then undergoes a ring opening decomposition reaction with the solvent to produce inorganic species that precipitate on the surface of the electrode [29, 38]. These precipitated inorganic species together with solvated $Li^+$ are trapped in existing pores on the electrode as the electrode is polarized to potentials below 2.5V vs. $Li/Li^+$ [39-42]. The specific potential is a function of electrode type and solvent [43, 44]. The lifetime of the trapped solvated $Li^+$ within a growing SEI depends on the donor-acceptor properties of the solvent molecules [45]. On the edge plane of a highly oriented pyrolytic graphite (HOPG) electrode, which has more reactive sites than the basal plane, these reduction species form a dense and homogeneous SEI layer that consists of sub-layers [47,48]. The binder materials such PVDF and SBR, holding the electrode particles together is reported not to affect SEI formation, but rather react favorably with decomposition species to form species that contribute to the SEI layer [46].The reduction species have “sticky fingers” which improves its adhesion to the graphite particles to improve the robustness of the SEI layer [49, 50] as shown in Figure 2.2. The positively charged alkyl organic moiety aligns with the SEI in such a way that those atoms bearing the partially positive charge serve as the adhesion point and the next layer will attach itself to the SEI layer via coulombic attraction from the negatively charged graphite surface [51].

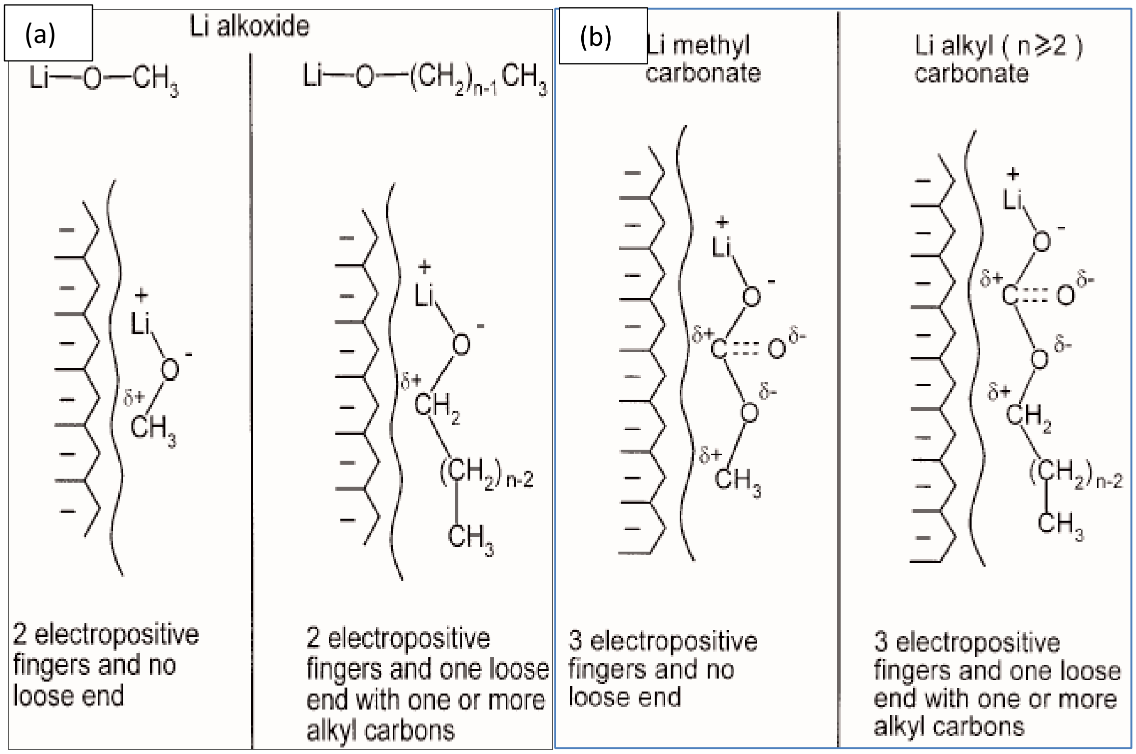

Figure 2.2 : Schematic of the sticky-fingers model of the (a) Li methyl and alkyl carbonate, and (b) methoxide and alkoxide from reduction of the alkyl carbonate on the graphite particles [49]

The composition of the SEI layer resulting from this electrolyte decomposition reaction generally depend on the salt and solvents of the electrolyte system employed in the battery. The SEI layer generally consists of species such as $ROCO_2Li$, $CO_2OLi$. The $ROCO_2Li$ can undergo reduction reaction with $CO_2$ and traces of $H_2O$ in the electrolyte to form lithium carbonate [51] which further reacts with EC to form transesterification products such dimethyl-2, 5-dioxahexane carboxylate (DMDOHC), ethyl methyl-2,5-dioxahexane carboxylate (EMDOHC) and diethyl methyl-2,5-dioxahexane carboxylate (DECDOHC). In addition, the metastable specie $ROCO_2Li$ within the SEI decomposes into more stable compounds $–LiC_2CO_3$ and LiF at elevated temperature. Thus altering the SEI microstructure and exposes the graphite-lithium surface to more electrolyte decomposition reaction.

The SEI layer formed on the anode electrode surface plays a critical role in the cycle life of the Li-ion batteries, as it prevents further electrolyte reduction reaction from occurring. However, when the lithium ion battery is subjected to several electrochemical cycles, the SEI layer grows in thickness leading to several aging mechanism occurring which ultimately affect the energy delivery of the lithium ion battery.

## 2.4 Factors Influencing SEI Growth

The SEI growth is generally expected to be affected by the electrolyte flow rate, electrolyte composition [52], the charging current, voltage, temperature, [29, 53], and to a lesser degree, the anode to cathode contact pressure [54]. The SEI has also been reported to grow linearly with the square root of the time for a range of current densities for carbonaceous anode materials [53, 55, 56, 57]. However, on the microstructure level the thickness of the SEI on the carbonaceous anode differs. The SEI layer is thicker on the edge plane compared to the basal plane after the first electrochemical cycle [58]. In addition, the SEI layer thickness is independent on the current density at least at 20˚C but evolves as the temperature increases ( >35˚C) [59,60] thereby aging the SEI film faster. An unfavorable formation temperature (< -30°C and > 60°C) can cause structural changes to the pores and create a number of defective sites in the SEI layer [61]. This also creates species accumulation at these defective sites to increase the amounts of reduction products constituting the SEI layer [62, 63]. The temperature changes, which influence the kinetic of the electrolyte decomposition, affect directly the spatial uniformity of the SEI Layer [58]. In this case, a denser SEI would be formed on the edge plane compare to the basal plane of the graphite anode electrode at high temperature. Whereas, a moderate to low temperature, will promote the formation of a uniform and less dense SEI layer. Adding dilithiumphthalocyanine additive significantly controls the imbalances in the SEI layer in thickness on the graphite and enhances Li ions transport rate [64]. The onset temperature for thermal breakdown of the passive film (SEI) in any given type of carbon is electrolyte salt dependent [65]. The SEI layer is also reported to partially dissolve during cell over discharge [66, 67]. Thus deep battery discharge at the formation stage is not desirable, as a partially dissolved SEI layer may not function effectively.

The electrode potential and temperature are the other factors that greatly influence the variation of the thickness of the SEI layer [68-70]. A thick SEI layer is formed at a deep discharge state and high formation temperature (i.e. >45˚C) [65, 71, 72]. This deep discharge and high formation temperature affects the microstructure of the SEI layer which greatly influences the cell performance [73]. The breakdown of the SEI layer leads to further electrolyte decomposition reaction resulting the formation of various species on the surface of the anode electrode.

## 2.5 Degradation of the of SEI Layer

An ineffective SEI layer is a source for trapped solvated lithium ions in the growing layer and the origin of metallic lithium clusters [72, 74, 75, 76]. The trapped solvated Li ions in the growing SEI react with electrolyte to increase reduction species surface concentration [77] that significantly increase charge transfer resistance [78-83]. The accumulated reduction species on the graphite surface decrease the pores of SEI layer that lead to a sluggish $Li^+$ intercalation/de-intercalation kinetics at the electrode/SEI layer interface.

The reaction of the SEI layer with $H_2O$ leads to the generation of $OPF_2OR$,( when R= $CH_2$) an autocatalytizer, to accelerate the decomposition of the salt to alter SEI layer composition and distorts its structure [35]. This structural change in the SEI layer decreases its ion conductivity at cell storage conditions [53, 84]. At high cell operating temperatures, the SEI completely breaks down [59, 60]. The breakdown of the SEI layer results in the percolation of solution inside the bulk graphite between the particles and is usually governed by salt reaction [85].

### 2.5.1 Electrolyte decomposition

A detailed analysis of the electrolyte decomposition mechanism is presented in the ensuing discussion. This discussion will provide an insight into how the various types of reaction species that are formed on the anode electrode/electrolyte interface during the decomposition reaction process.

### 2.5.1.2 Solvent reduction

The carbonate solvents reduction follows either one-electron reduction process. As in the case of ethyl methyl carbonate (EMC), which is reduced by one-electron process in Equation 7.

$$CH_3CH_2O(C=O)OCH_3 + e^- \rightarrow CH_3CH_2O(C^{\bullet}-O^-)OCH_3 \qquad (7)$$

to produce an intermediary ; $CH_3CH_2O(C^{\bullet}-O^-)OCH_3$ which then reacts with $Li^+$ to produce the species $CH_3CH_2OLi$ according to Equation 8.

$$CH_3CH_2O(C^{\bullet}-O^-)OCH_3 + e^- + 2Li^+ \rightarrow LiO(C=O)CH_3 + CH_3CH_2OLi \qquad (8)$$

Alternatively, by a two electron reduction process, as in the case of dimethyl carbonate (DMC), (Eq. 9)

$$CH_3OCO_2CH_3 + 2e^- + 2Li+ \rightarrow Li_2CO_3 + C_2H_{6(g)} \qquad (9)$$

can occur, where the reduction process involves the solvent molecule, a transfer of two-electrons, and $Li^+$ to produce a lithium carbonate species and a gas [66, 86, 87]. The ensuing discussion will however focus on the reduction of EC solvents and the salt $LiPF_6$ which are commonly used electrolytes solvents.

### 2.5.1.3 Ethylene carbonate (EC)

In a mixture with other carbonate solvents, ethylene carbonate (EC) is preferably reduced due to its high polarity and dielectric constant [88]. Like the DMC and DEC solvents, the reduction of EC also involves a two-electron [79] transfer to one mole EC molecules and a reaction with $Li^+$:

$$(CH_2O)_2CO + 2e^- + 2Li^+ \rightarrow Li_2CO_3 + C_2H_4\ (g) \qquad (10)$$

to produce $Li_2CO_3$ and $C_2H_4$ gas (Eq. 10) or a two-electron transfer to two moles of EC and $Li^+$ to form a lithium alkyl carbonate specie, which is deposited on the graphite particles and $CH_2$ gas that remains in solution with the electrolyte (Eq.11).

$$2EC + 2e^- + 2Li^+ \rightarrow (CH_2OCO_2Li)_2 \downarrow + CH_2 = CH_2 \uparrow \qquad (11)$$

Where ↑ gas evolution in solution and ↓ species deposited on the particles surface. The species $(CH_2OCO_2Li)_2$ can readily react with traces of $H_2O$ in solution to produce $Li_2CO_3$, $(CH_2OH)_2$ and $CO_2$ gas (Eq. 12) [87,79].

$$(CH_2OCO_2Li)_2 + H_2O \rightarrow Li_2CO_3 \downarrow + CO_2 + (CH_2OH)_2 \qquad (12)$$

The EC solvent reduction, however, depends on the applied cell potential which ranges between 4.6-4.9V vs. $Li/Li^+$ [89] to overcome the decomposition reaction barrier [88]. The high polarity of the EC makes it an easy target for electrophilic and nucleophilic reaction [90, 91]. In a presence of salt reduction anionic species $PF_6^-$, $ClO^-_4$, $BOB^-$, $F_2OB^-$ $AsF_6^-$, and $CF_3SO_3^-$ from electrolyte salts, such as $LiPF_6$, $LiClO_4$, LiBOB, $LiF_2OB$, $LiAsF_6$ and $LiCF_3SO_3$, the ring opening and bond breaking of ethylene carbonate molecules are triggered to form various species on the surface of the electrode. In particular, the decomposition species of $POF_3$ from $LiPF_6$ reduction (Eq. 13):

$$PF_5 + H_2O \rightarrow 2HF + POF_3 \qquad (13)$$

form $POF_3$, which reacts with EC to produce an intermediary $CH_2FCH_2OCOOPF_2O$ species by Equation 14

$$POF_3 + EC \rightarrow CH_2FCH_2OCOOPF_2O \qquad (14)$$

The intermediary then further dissociates to form $CH_2FCHOCOOPF_2O$ and $CO_2$ according to Equation 15.

$$CH_2FCH_2OCOOPF_2O \rightarrow CH_2FCH_2OPF_2O + CO_{2\,(g)} \qquad (15)$$

Another possible reaction involves the salt anion $PF_6^-$ and the species $POF_3$, which simultaneously can attack the EC molecule to form a bulk anion $CH_2FCH_2OCOOPF_3O^-$ and a Lewis acid according to Equation 16,

$$POF_3 + EC + PF_6^- \rightarrow CH_2FCH_2OCOOPF_3O^- + PF_5 \qquad (16)$$

which can dissociates further to form an additional anion in solution (Eq.17)

$$CH_2FCH_2OCOOPF_3O^- + PF_5 \rightarrow CH_2FCHOCOOPF_2O + PF_6^- \qquad (17)$$

to perpetuate the decomposition reaction [90]. This initiated autocatalytic process can be suppressed by adding a Lewis base complex such as hexamethoxycyclotriphosphazene and hexamethylphosphoramide to the chemical species $PF_5$ to form a stable acid-base [92].

Furthermore, the $LiPF_6$ salt, which is thermodynamically unstable [93], can react with species $Li_2CO_3$ from EC reduction to produce LiF, $POF_3$ and $CO_2$ (Eq. 18).

$$LiPF_6 + Li_2CO_3 \rightarrow 3LiF + POF_3 + CO_2 \qquad (18)$$

Alternatively, the $LiPF_6$ reduction species $PF_5$, readily reacts with $Li_2CO_3$ (Eq. 19):

$$PF_5 + Li_2CO_3 \rightarrow 2LiF + POF_3 + CO_2 \qquad (19)$$

On the other hand, the HF species reacts with the $Li_2CO_3$, to produce $CO_2$ and $H_2O$ (Eq. 20)

$$Li_2CO_3 + 2HF \rightarrow 2LiF + CO_2 + H_2O \qquad (20)$$

The trace impurities of $H_2O$ and $CO_2$ in solution are reported [94] to react with $Li^+$ to form $Li_2CO_3$, LiOH and $Li_2O$ that form part of the SEI layer to suppress further electrolyte reduction. The LiF species from these reactions with $Li_2CO_3$, however, is deposited on the electrode forms an insoluble, non-uniform and electronically insulating layer on the graphite particle surfaces [95-97].

These reaction products on the electrode surface may crack due to the difference in thermal expansivity between the deposit layer and the graphite particles during the de-insertion of the lithium ions [89, 98]. This phenomenon could allow further reaction at these newly created crevices on the electrode surface.

#### 2.5.1.4 Decomposition of $LiPF_6$ Salt

The $LiPF_6$ salt is the most commonly used salt in lithium ion batteries. The decomposition of $LiPF_6$ follows a two-step process in which the decomposition is related to the release of free acid followed by decomposition of the salt [99]. The initial reaction for the salt decomposition is electron transfer from the electrode to the salt molecule [100, 101] to produce toxic alkyfluorophosphates (A). The alkyfluorophosphates is initiated through autocatalytic from aprotic impurities of water or alcohol [36, 38,102] which accelerates the decomposition of $LiPF_6$ (B), as illustrated reaction in Figure 2.3.

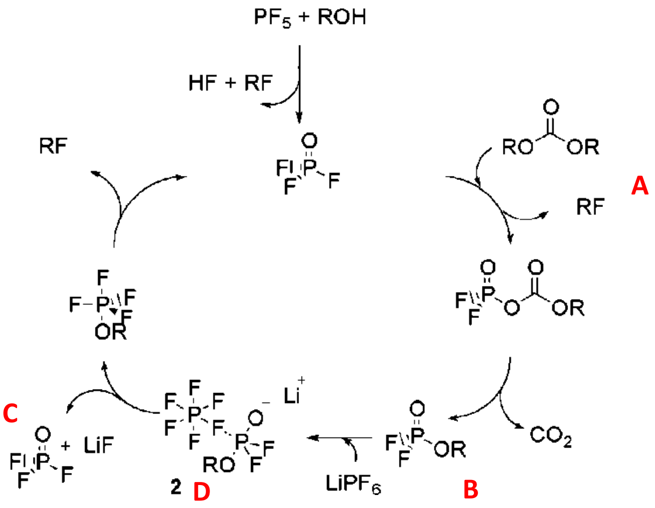

Figure 2.3: Schematic of autocatalytic reaction mechanism for the $LiPF_6$ [57]

In the reaction mechanism in Fig. 2.3 the salt dissociates into several chemical species: LiF (C), and the Lewis acid $PF_5$ (Eq. 21);

$$\mathrm{LiPF}_6 \leftrightarrow \mathrm{LiF} + \mathrm{PF}_5 \tag{21}$$

or a $Li^+$ and the anion $PF_6^-$ as shown in Equation 22.

$$\mathrm{LiPF}_6 \leftrightarrow \mathrm{Li}^+ + \mathrm{PF}_6^- \tag{22}$$

The dissociated Lewis acid $PF_5$ can react with $H_2O$ (Eq.23 and 24), existing as an impurity in solution or alcohol to form the species; $POF_3$, $PF_4OH$, and HF [79, 98, 99]

$$\mathrm{PF}_5 + \mathrm{H}_2\mathrm{O} \rightarrow 2\mathrm{HF} + \mathrm{POF}_3 \tag{23}$$

$$\mathrm{PF}_5 + \mathrm{H}_2\mathrm{O} \rightarrow \mathrm{PF}_4\mathrm{OH} + \mathrm{HF} \tag{24}$$

The species $PF_4OH$ can further dissociates to produce $POF_3$ and HF that remain in solution [102, 38];

$$\mathrm{PF}_4\mathrm{OH} \rightarrow \mathrm{POF}_3 + \mathrm{HF} \tag{25}$$

The Lewis acid $PF_5$ can also react with dialkylcarbonate to form a variety of decomposition products; ethers ($R_2O$), alkylflorides, and phosphorus oxyfluoride ($OPF_3$) [99, 103, 104, 105]. The generated $POF_3$ reacts with the solvent DEC to produce

$OPF_2OC_2H_5$ along with $CO_2$ and $C_2H_5F$. The generated ethylfluorophosphate in solution interacts with the anion $PF_6^-$ and forms the complex labeled as D in Figure 2.3. However, the stability of $PF_5$ in solution depends on the solvent, it is stable in polar sterically compact solvents, such as EC, while in less polar and bulky solvents such as DMC and DEC [103], the $PF_5$ species is often unstable.

The decomposition of $LiPF_6$ is further promoted by solvents with large dielectric constants and high viscosity [105, 106], such as EC. Such high dielectric constant solvents increased the ionization of the salt and accelerate its reduction reaction and its subsequent reaction with water to form the LiOH species. When the salt anion and solvent are reduced simultaneously, their reduction reaction interferes to produce a less passive SEI film that is less protective [107]. This will cause the salt and solvent compositional change that eventually reduces the ionic conductivity of the electrolyte [108] and thus degrades its transport properties via conducting species depletion [109]. This however, depends on the electrode potential and the electrolyte composition [45]. This phenomenon is usually corrected through proper electrode materials and electrolyte selection and electrode design, therefore does not often arise in most lithium ion batteries chemistries.

Some of the methods employed to minimize the thermal instability of the salt $LiPF_{6,}$ include inhibiting the transesterification of dialkylcarbonate [38, 105] and lowering the concentrations of protic impurities of $H_2O$ and EtOH in the carbonate solvents [102, 109, 110, 71]. The addition of inorganic compounds, such as tris (2, 2, 2-trifluroethyl) phosphite (TTFP) and low concentration of Lewis bases; pyridine, hexamethoxycyclotriphosphazene and hexamethylphosphoramide to the salt has also been used to improved thermal stability. The inorganic compounds inhibit the reactivity of the Lewis acid $PF_5$, which is the main cause of the instability of $LiPF_6$, to effectively improve the stability of $LiPF_6$ salt [1, 2, 3, 109]. The lithium ion batteries undergo a multitude of aging mechanisms, which are large attributed to the failure of the various battery components. Some of these aging mechanism especially those occurring at the anode electrode will be discussed in section 2.6.

## 2.6 Battery Degradation Mechanisms

The performance of the battery depends on the development of materials for the various components of the lithium ion battery [110-112]. The degradation of these components during the battery operation adversely affects the energy delivery of the battery. The various battery components undergo different aging mechanisms; the binder and electrolyte decompose, the current collector corrodes, the separator melts (at high operating temperatures >80° C) and corrodes and the cathode undergoes structural disorder and metal dissolution, while the anode electrode undergoes a multitude of degradation compared to the cathode electrode; lithium plating, dendrite formation, deposition of reaction products on its surface, etc. All these degradation mechanisms on the various components of the lithium ion battery affect the electrochemical performance of the battery. The anode electrode, in particular can undergo a multitude of aging mechanisms that degrade the electrochemical performance of the lithium ion battery.

The most commonly used anode materials include carbon-based compounds and lithium-alloys. The microstructure, texture, crystallinity and morphology of the anode electrodes of the battery directly influence the battery performance [113]. By design, the anode electrode has a large geometry dimension compared to the cathode electrode so as to prevent edge lithium plating. Also, the anode electrode generally has excess anode capacity compared to the cathode so that the battery can deliver high energy density [114]. A reduced anode capacity will polarize the anode to a potential close to lithium deposition potentials.

The anode electrode microstructure plays a key role in the total battery performance. It therefore not surprising that over the last decade many more research efforts are aimed at improving the microstructure of the anode electrode.

Several methods have been explored, including the inclusion of stabilizing compounds into the graphite matrix, formulations of dendrite and lithium plating suppression electrolyte systems.

### 2.6.1 Loss of lithium ions

The amount of lithium ions in the lithium ion battery involved in an electrochemical cycle is conserved under ideal conditions. However, the lithium ions are irreversibly loss-lithium ions which isolated from the electrochemical process, during the electrochemical aging process of the lithium ion battery. This irreversible lithium ion loss is generally attributed to two phenomena, namely; i) solid electrolyte interphase (SEI) layer formation via electrolyte decomposition at the formation stage, ii) side reaction of lithium ion with decomposed electrolyte compounds and water (e.g. 10-1500 ppm) in the electrolyte at the later stage of the battery operation [115].

The loss and /or consumption of recyclable lithium ions at the anode by the passive layer is a major cause of the reduction in the reversible capacity of the lithium ion battery [116, 117]. As the layer grows, lithium ions are consumed in the reaction and the increased thickness inhibits $Li^+$ transfer. The formed layer is less conductive compared to the SEI layer thus the lithium ions must tunnel through the layer. This phenomenon is the main degradation mechanism in fully charged batteries under storage conditions [118-121], where the electronic insulating surface layer formed clogs the pores and isolate graphite particles. The irreversible lithium ion loss is also a function of the specific area of the graphite particles, since an increase in area increases the volume of reaction products [122, 123]. For a graphite anode with low specific area, the charge loss is low. The electrolyte additive vinylene carbonate (VC) is one such electrolyte additive that increases the lithium ion loss rate at the anode for the Li/coke electrode during storage (ambient temperature conditions). Because the VC increases the rate of SEI formation reaction at ambient temperature conditions to increase the SEI thickness. However, the benefit of using VC as an additive is seen at higher temperature (35$^o$C to 50$^o$C) and higher voltages >0.4V for Li/Coke electrode, as it slows down the side reaction rate and undergoes reduction and polymerization to form poly alkyl Li-carbonate species that suppress both solvent and salt anion reduction on the anode electrode. Similarly, in batteries stored at voltages greater than 3.6V, electrolyte oxidation at the cathode can also induce surface reaction deposits that cover the active cathode electrode area. These covered areas are insulating, which could result in a non-homogeneous local current distribution in the cathode electrode. These reaction deposits are also sources of lithium ion loss in the electrochemical process.

### 2.6.2 Metallic lithium plating

Common anode materials currently in use in lithium ion batteries include graphite, coke, hard carbon, highly ordered pyrolytic graphite and lithium titanate. Among these families of anode materials, the unmodified graphite (Mag-10) electrode is most susceptible to lithium plating because of the close proximity of its reversible potential to that of $Li^+/Li$ [124, 125]. Lithium plating by itself is reversible, as the plated lithium oxidizes at potential of about 100mV, a potential much lower than that of lithium de-intercalation potential at the anode electrode, causing a voltage overshoot during the discharge cycle (over potential) [126] as shown in Figure 2.4. Well-ordered carbon and non-graphitizable carbon have gradually replaced lithium metal as the preferred anode material for the lithium ion battery because of their superior capacity, good cycleability, lower susceptibility to lithium plating, and low electrode potential relative to $Li^+/Li$.

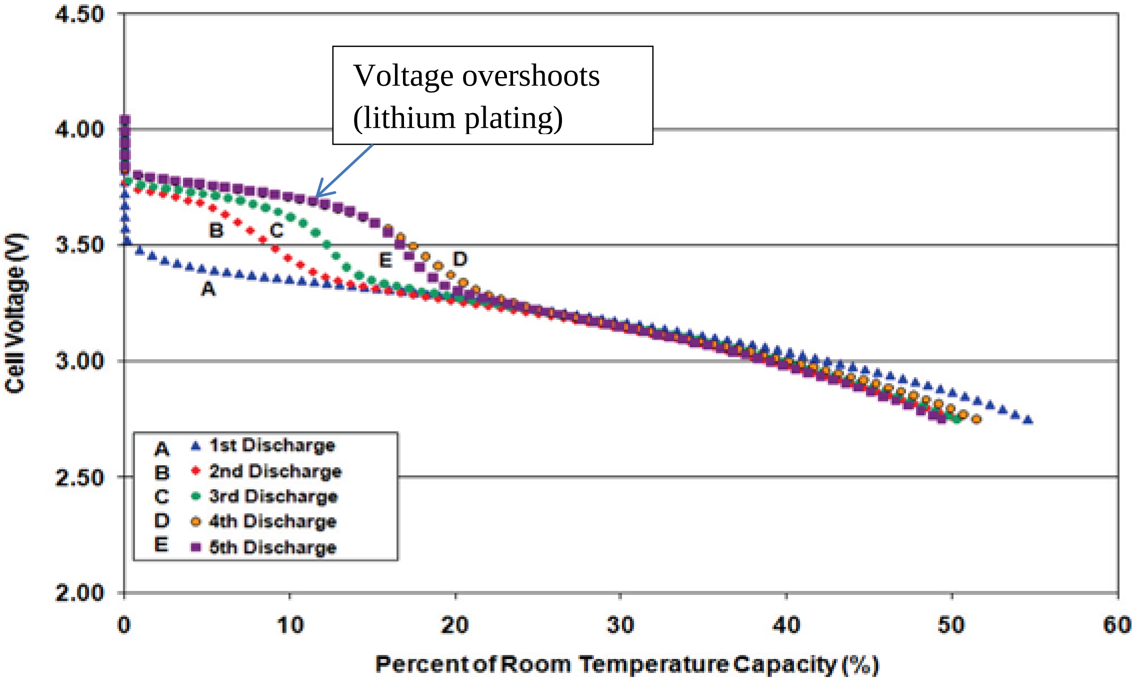

Figure 2.4 : Discharge voltage over-shoots showing the presence of lithium plating [126]

There are several factors that initiate the formation of metallic lithium on the surface of the anode electrode, namely: i) the nature of the electrolyte (i.e. electrolyte formulations with high EC content exhibit lithium plating), ii) the ratio between anode and cathode capacities (i.e. low anode/capacity ratio will polarize the anode and promote lithium plating), iii) the operating temperature and iv) the charge rate (i.e. low temperature (-20$^o$C) and high charge rate) all influence lithium plating on the anode. These factors affect the anode kinetics and the lithium ion diffusion rate, such that lithium plates on the surface of the electrode rather than intercalating into the lattice of the carbon.

The formed metallic lithium deposits on the graphite anode are affected by the degree of random crystallographic orientation of the particles in the crystal structure in the anode material and the non-uniformity of the current distribution which is a function of diffusion and current density [127]. The disorientation of the particles in the graphite electrode initiates inhomogeneity in the charge distribution on the anode electrode and results in the formation of moss-like deposits and dendrites [128-131]. These moss-like deposits and dendrites grow as a function of the temperature and current density between the polymer separator and the anode electrode. As the temperature and charge rate increases, the reaction rate also increases and metallic lithium is deposited on the graphite at overcharge. When the amount of dendrites formed on the anode surface grows, they begin to agglomerate thus can cause the separator to disconnect and become isolated from the electrolyte and in some instances pierce through the separator. The mat of dead lithium and dendrites can cause a short circuit and thermal runway in the battery. The signature of lithium plating in batteries is usually manifested as a voltage plateau on the discharge voltage profile and associated low battery columbic efficiency [114]. The exessive electrolyte decomposition on the anode side that results in the formation of the passive layer can also trigger lithium plating and ultimately causing battery thermal runnaway.

### 2.6.3 Formation of passivated surface layer

At higher battery potentials, during the intercalation of lithium ions into the graphite lattice structure,the graphite anode reduces. At this potential, electrolyte co-solvents, such as EC, which is highly reactive, reacts with the lithium ions and the reaction products quickly precipitate and grow on the anode surface [132-134]. The presence of these reaction products on the surface retards the intercalation kinetics of the carbon anode [135]. The surface layer grows in thickness as the decomposition reaction continues [136–142]. The layer thickness is established to be a function of operating cycles, regardless of the charging protocol (i.e., pulse charging or DC charging) [143–145].The layers become unstable and crack due to expansion and contraction of the graphite lattice during the process of insertion and de-insertion of the lithium ions [146–148]. This allows further surface reaction at these sites that may eventually isolate the graphite particles from the current collector. Figure 2.5 shows a typical surface film morphology and cracking of the layer [149]. The surface crack formed on the surface does not typically travel to the carbon electrode [146]. The growth of this surface layer on the anode electrode is prevalent in the electrolyte system with EC as the co-solvent compared to those with DEC or DMC as co-solvents [150–152].

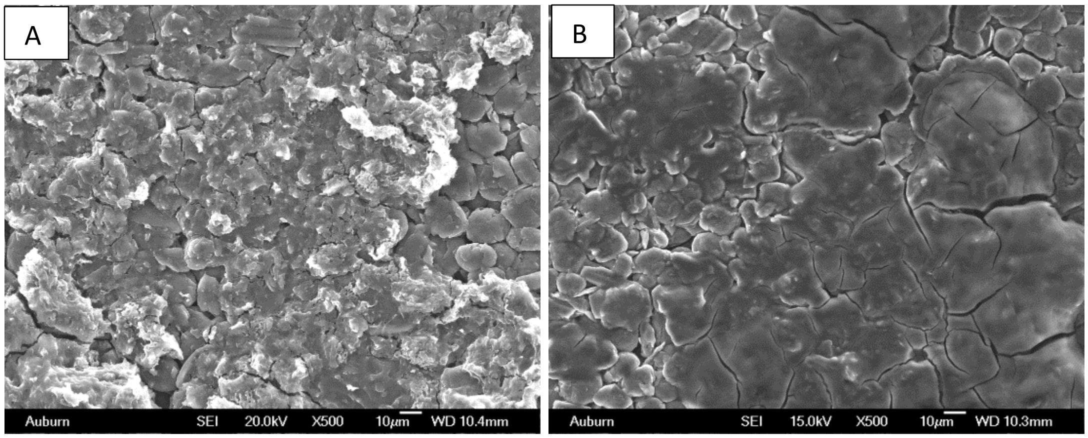

Figure 2.5: Growth of the passivation layer on the anode resulting from electrolyte decomposition (a) Surface film agglomerates (b) surface film forms a “mat” on the carbon electrode particle surface area [149].

In addition, anion contaminates, such as $F^-$ from HF and $PF_5$, readily react with lithium to form insoluble reaction products which are non-uniform, electronically insulating, and unstable on the surface of the graphite particles [153–157]. In addition, the dissolution of the cathode electrode metal from the lattice into the electrolyte due to the disproportionation of $Mn^{3+}$ (into $Mn^{2+}$ and $Mn^{4+}$) by traces of hydrofluoric acid (HF) in the electrolyte, result in the deposition of cation contaminates, such as of Mn, Co and Fe, on the anode electrode surface [158]. The formation this layer has been associated with the loss of lithium ions and continue depletion of the electrolyte in the battery pack[116], that ultimately affacts the lithium ion tranfort and diffsivity.

### 2.6.4 Degradation due to structural changes

Anode materials, such as mesosphere pitch-based carbon (MSPBC) and vapor grown carbon fibers (VGCF), have high surface area morphologies that provide large discharge capacity and high charge rate performance [117]. During battery degradation, the disordered structures of the carbon maybe affected i.e. the stacking sequence could change from AA to AB, but this structural change does not in any way affect the battery degradation [132]. Degradation can be either in the form of the lithium plating or the formation of the surface layer. Neither the particles size nor the lattice parameter change significantly with these degradation processes [159]. Cycling the lithium ion batteries at high C-rate and high state of charge (SOC) induces mechanical strain on the graphite lattice of the anode electrode due the steep gradient of lithium ions, and thus lattice parameter, in the particle. This mechanical strain caused by the insertion and de-insertion of the lithium ions cracks, fissures and splits the graphite particles thus making these particles less oriented as compared to the original platelets [160]. Pressed graphite particles improve the ionic conductivity with a trade off in increase irreversible capacity loss [161]. The nature and orientation of the graphite particles influences the reversible capacity of the anode. For instance, less-oriented graphite particles have a low reversible capacity due to more difficult lithium intercalation kinetics. In addition, cervices existing on the less-oriented particles are source of electrolyte accumulation [162–167]. While flake-like graphite particles have higher gravimetric capacity at higher C-rate compared to spherical particles [168]. Although the crystal structure of the anode typically does not change with aging, a change in the rhombohederal/hexagonal content during battery operation has been reported. The increase in the hexagonal content in the graphite crystal structure lowers Faradic efficiency especially during the initial stage of lithium ions intercalation, thereby decreasing the reversible capacity of the anode [169-171], so ideally a high ratio of rhombohederal/hexagonal content which gives a high reversible capacity is most desired.

Table 2. 1: A summary of degradation mechanism and their effects on the energy delivery of the battery

| **Cause** | **Effect** | **Reduced by** | **Enhanced by** |
|---|---|---|---|
| 1. Electrolyte decomposition( SEI) Continuous side reactions at low rate<br>2. Solvent Co-intercalation, gas formation and cracking formation in particles<br>3. Decrease of accessible surface area due to continuous SEI growth<br>4. Change in porosity due to volume changes (SEI formation and growth)<br>5. Continuous loss of active material particles due to volume changes during cycling<br>7. Metallic lithium plating and subsequent electrolyte decomposition by metallic lithium | Loss of lithium,<br>Impedance rise<br>Loss of active material (graphite exfoliation)<br>Loss of lithium<br>Impedance rise<br>Impedance rise<br>Over potentials<br>Loss of active material<br>Loss of lithium<br>Loss of electrolyte | Stable SEI(additives)<br>Rate decreases with time<br>Stable SEI(additives)<br>Carbon pretreatment<br>Stable SEI(additives)<br>External Pressure<br>Stable SEI(additives)<br>External Pressure<br>Narrow Potential Window | High Temperature<br>High SOC<br>Overcharge<br>High Temperature<br>High SOC<br>High Cycling Rate<br>High SOC<br>High Cycling Rate<br>High DOD<br>Low Temperature<br>High Cycling Rates |

These degradation mechanisms are not exhaustive, as the discussed herein and are those mostly associated with the carbonaceous anode electrode which are summarized in Table 2.1. Alloying the Li with several viable metal such as Si, S, Al, Ag, and Pb which alloy electrochemically with lithium are some anode materials that have received a lot research attention because of their viability as anode materials. Al these alternative anode materials come with their own peculiar aging mechanisms, for instance the structural instability is the biggest problem associated with the Li/Si anode. In general, the capacity fade of the battery involves a multitude of aging phenomena of its components. The degradation of the other components of the battery are shown in Figure.

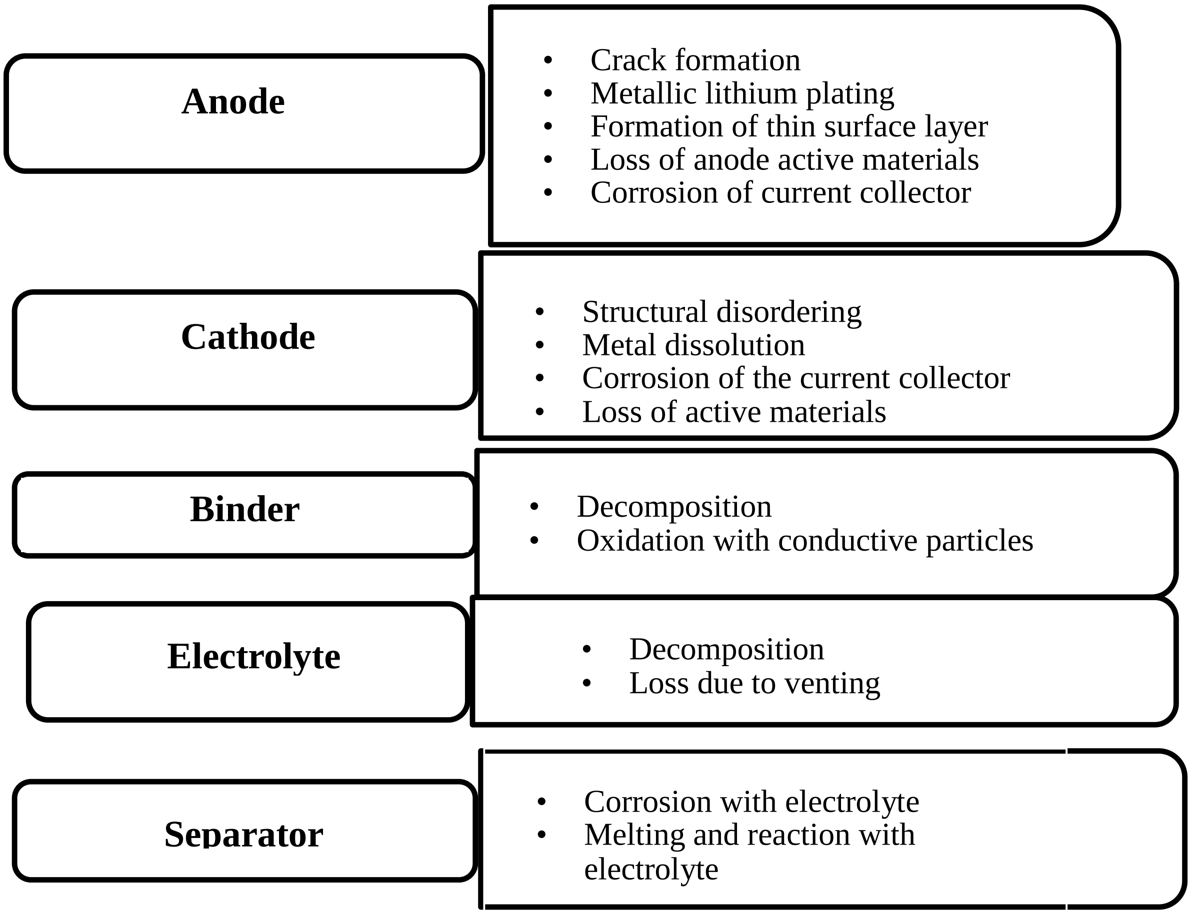

Figure 2. 6: Degradation mechanisms of the various components of the lithium ion battery

The aging mechanisms as summarized in the Figure and Table 2.1, it is obvious that battery aging is still a very active research area. While there is this parallel active research in the design and development of the new materials for energy storage, a complete understanding the aging mechanism is important in order the limit these mechanism. This research is part of this knowledge seeking in the area lithium ion battery aging. Several research groups have reported the formation and growth of the passivation layer on the carbonaceous anode electrode and it being the source of lithium ion loss.

Many of these research have not presented any experimental evidence to back their various claims but who cited sources all lead to the E. Peled [181] work on the solid electrolyte interphase. The research reported here, provides an experimental evidence based quantitative and qualitative analysis of the effect of the state of charge (SOC) on the growth of the deposit surface film layer and a quantitative analysis measurement of the loss of lithium ions.  Understanding how the battery charging protocols influence the formation of the deposit surface layer is critical to effectively controlling/limiting these operational parameters to extend the operational lifetime of the lithium ion battery.

### 2.7 Objectives of the Research

The overall objective of this research is aimed at answering the scientific question; what potential and charge rate influences the decomposition reaction on the anode electrode. Lithium ion batteries employ porous electrodes to increase the active area between the electrolyte and the active carbon particles in order to facilitate the electrochemical reaction process. Electrolyte decomposition side reaction deposit a layer on the surface of the active carbon materials, which clogs the pores of the electrode. The blocking of the electrode pores by the growing surface layer on the electrode thus affects the electrochemical energy conversion process.

The result is a loss in lithium ions and a rise in the charge transfer resistance, Ohmic resistance, and the SEI film resistance culminating into the overall batteries impedance.

The hypothesis is that, a high battery potential during charging creates a region of high polarization on the surface of the anode electrode (overpotential). At this region of high polarization, according to Butler equation (Eq.26), the current density of the anode is governed by;

$$\vec{i} = i_a = nFk_{red}C_{red}\exp\left(\frac{\alpha F}{KT}\Phi\right) \qquad (26)$$

where $i_a$ is EC reduction current density, $C_{red}$, is the EC concentration, Φ, is the graphite potential, and β is the charge transfer coefficient.

Therefore the reaction rate occurring on the electrode surface is a function of the migration or concentration electrolyte and the electrode potential. A high battery potential during charging creates a region of high polarization, thereby creating a situation where different parts of the electrode could reach different Li deposition potentials. The Tafel equation establishes the relationship between the current density at the electrode and the activation polarization as in Eq. 27;

$$\Delta E = a + bIni = a + b^{'}\log i \qquad (27)$$

Where the constant $a$ is the value for polarization at unit current density ($1mA/cm^2$) and $b$ often refer to as the Tafel slope and varies slightly with temperature; $b \approx 0.05V$

From this analysis, it logical that a high potential will polarized the electrode and subject it to passivation reaction. Therefore a high charge rate coupled with a high electrode potential will accelerate the passivation reaction resulting in the formation of the surface layer. At these conditions, the solid electrolyte interphase (SEI) layer becomes ineffective as the battery is cycled at high potential and charge rate thus allowing further decomposition reactions. A series of electrochemical test listed in Table 1, were designed to evaluate this hypothesis. Electrochemical data such as capacity fade; the overall battery impedance, the Ohmic, SEI film, and double layer capacitance were extracted from the equivalent circuit model after the electrochemical cycling of the LIB. A postmortem analysis of the anode electrode was carried out and a quantitative analysis of the thickness of the formed surface layer was carried out using analytical tools such as SEM. The composition and amount of the compounds constituting the surface film layer formed on the carbon particles was analyzed using complementary tool such as the Fourier Transform infrared spectroscopy (FTIR) and X-ray photoelectron spectroscopy.

### 2.7.1 Research Contribution

The results from this research showed evidence of the growth the deposit layer and how battery potential influenced its growth. A quantitative measurement of the loss of lithium ions resulting from two sources: trapped lithium in the graphite crystal structure and that consumed in the formation of the deposit layer was achieved. These results are ultimately to the emerging hybrid electric vehicles (HEV) industries by establishing a charge/discharge protocol that minimizes the battery degradation and promotes the longevity of the battery pack. The second phase of the project, which involves the development of a physics aging model, will be capable of predicting the growth of this layer as a function of charge/discharge rate, cycle numbers and the operating temperature of the battery. This could be integrated into any battery management system to predict the growth of the surface layer.

# Chapter 3

# Materials and Experiments

## 3.0 Lithium Ion Polymer Battery

The lithium ion batteries used in this research were the pouch type lithium ion polymer batteries with cathode chemistry Li(Mn,Ni,Co)$O_2$ and a carbon based anode. The cathode consists of aluminum current collector coated on both sides with Li (Mn,Ni,Co) $O_{2,}$ while on the other hand the anode current collector is copper coated on both sides. The binder holding the active electrode materials particles together and onto the current collector surface was styrene-butadiene copolymer (SBR) and acrylate-type copolymer respectively for the anode and cathode electrodes. The separator is a micro porous polyolefin membrane made of laminates of polyethylene and polypropylene, with an average porosity of about 30%. The electrolyte system is solid electrolyte of organic salt $LiPF_6$, with co-solvents of ethylene carbonate (EC), and dimethyl carbonate (DMC). The nominal capacity of each battery is 15.7Ah with operating voltage range of 2.5 to 4.15V.

## 3.1 Battery Cycling Test Station

The charge/discharge cycles were performed using a test station designed by a team of researchers from Dr. Choe group, which (Fig. 3.1) comprised of a programmable charging system, a programmable electronic load system, and a data acquisition system that are controlled by LabVIEW$^{TM}$ residing in a PC. The testing system allowed for the input of various charging conditions i.e. C-rate, state of charge (SOC) and external temperature variables. An environmental chamber system was employed to keep the testing environment temperature at $25^oC \pm 2^oC$. The desired data from the electrochemical cycling i.e. voltage/ current profile, charge/discharge capacity data etc. are collected by executable Labview files.

The batteries were charged by a constant current-constant voltage (CC-CV) charging protocol at room temperature. In each cycle, the batteries were discharged with a constant current until the terminal voltage decreased to the voltage corresponding to the desired lower SOC ( eg. 25% = 3.13V) and then charged with a constant current up to the voltage corresponding to the upper SOC( eg. 3.78V) followed by a constant voltage (CV) charge. A 4C rate (i.e. 62.8A) charge and discharge current were used to accelerate the aging process. After every 20 cycles, a 1C (15.7A) discharge-resting-charge profile was applied to the cell to measure its capacity. The capacity ($Q_{max}$) was calculated by integrating the current when the cell is being discharged from 100% to 0% SOC using 1C current (15.7A) at room temperature. The $Q_{max}$ data for each battery was recorded every 20 cycles. The battery was rested for 10 minutes before and after the $Q_{max}$ measurement. The volume change in the battery pack was monitored using two linear variable differential transformer (LVDT) sensor probes attached to opposite sides of the battery, as seen in Figure 3.1. The SOC levels listed in Table 1 were chosen to maintain a constant capacity of 65%. The pre-test terminal voltage for the desired SOC was determined by coulomb counting.

Table 1: Test matrix of experimental details conditions

| State of Charge | Equivalent cycling Voltage (V) | C-rate/Current (A) | Other Conditions |
|---|---|---|---|
| 25-90% | 3.13-3.78 | 4C/62.8 | 25°C @ 600 cycles |
| 15-80% | 2.88-3.36 | | |
| 5-70% | 2.63-2.94 | | |
| 5-60% | 2.63-2.52 | | |
| 25-90% | 3.13-3.78 | 3C/47.1 | |
| 5-70% | 2.63-2.94 | | |
| 25-90% | 3.13-3.78 | 2C/31.4 | |
| 5-70% | 2.63-2.94 | | |

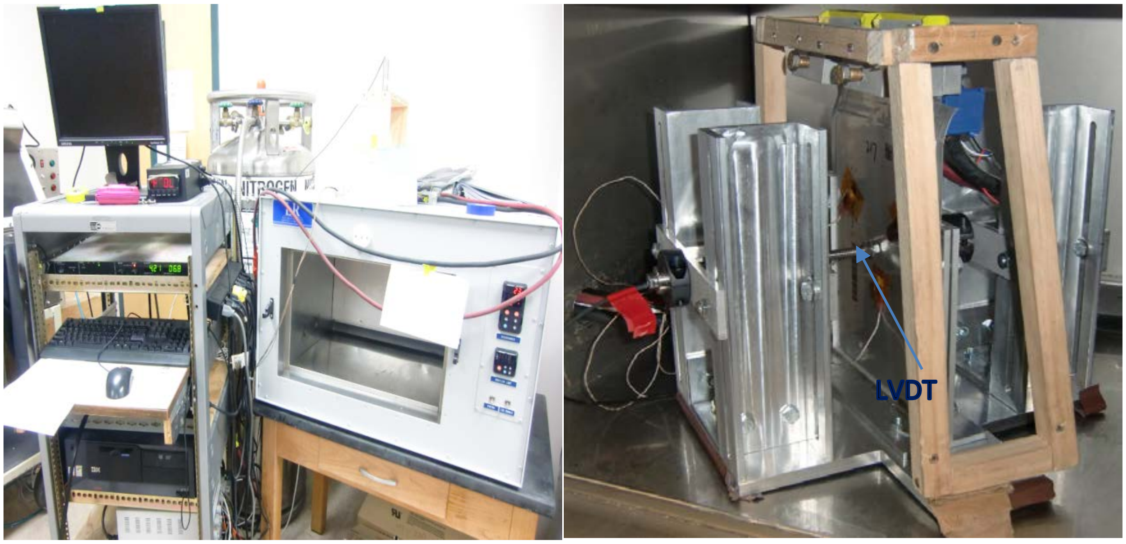

Figure 3.1: Pictorial view of the battery test station [Rujian]

### 3.2 Electrochemical Impedance Spectroscopy

The electrochemical impedance analysis of the batteries were carried out using the Gamry EIS framework in galvanostatic mode to apply different frequencies of small AC excitation current (1A) and the  battery voltage responses collected. The experimental setup for the EIS measurement consists of bipolar power supply used to supply AC current to the battery. A voltage signals is sent by the impedance measurement system to the battery and a require AC current to the power supply which senses the signal for measurement of true current flow. The system also senses the voltage of battery terminals through voltage sensing wires. The impedance data covered frequency range from 1 mHz to 1 kHz.  AC impedance measurements were carried out after 3 hours of rest in 25°C in an enclosed chamber from the electrochemical cycling for the batteries to attain voltage relaxation and thermal stability. An equivalent circuit model shown in Figure 3.3 was used to extract values of parameters that fit the experimental impedance data, which includes the SEI film resistance, the Ohmic resistance, the charge transfer resistance, the double layer capacitance and Warburg impedance of the battery.

The EIS is a valuable tool for the measurement of several phenomena occurring in the battery after several electrochemical cycles; parameters such as the electronic/ionic conduction in the electrode and electrolytes, interfacial charging at the surface films and the double-layer, charge transfer resistance and the mass transfer effects can be qualitatively determined from the measured cell impedance in the form of real and imaginary components and phase angles.  A typical impedance plots is shown in Figure 3.2. The high frequencies range; 1 kHz to 700 Hz is mostly associated with inductance of the external wires connected to the battery. This high frequency range is thus often excluded from the analysis.

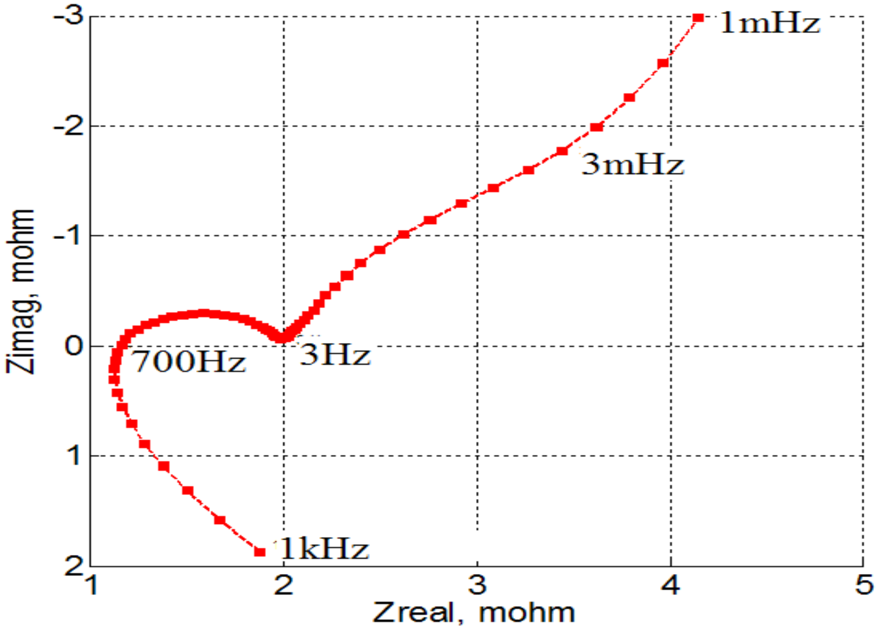

Figure 3.2: A typical Impedance plot for lithium ion battery [Rujian dissertation]

The two intersection points of the impedance spectrum with the real axis represent the Ohmic resistance of the battery. The Ohmic resistance generally consists of the electronic resistance from the electron flow through electrodes and the ionic resistance which is caused by lithium ion conduction through the electrolyte and separator. The frequency range from 700 Hz to 3 Hz, represents the impedance behavior of the solid interphase layer (SEI) between electrode and electrolyte. The third portion of the impedance spectrum in the frequency range of 3Hz to 3mHz, depicted in the second semicircle, represent combination of charge transfer resistance and double layer capacitance. Lastly, the low frequency region of 3 mHz to 1 mHz represents the diffusion behavior of lithium ions in electrolyte as well as inside the electrode particle. This region is often referred to as the Warburg impedance.

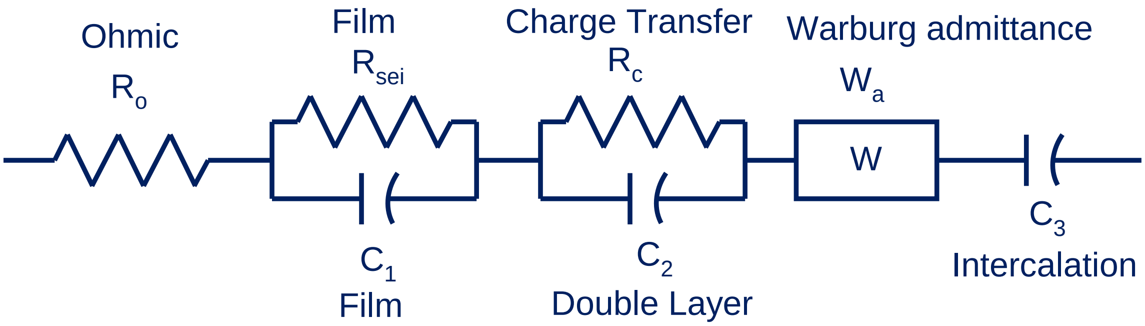

Figure 3.3: Equivalent circuit model schematic diagram [36]

## 3.3 Materials Characterization

### 3.3.1 Battery postmortem procedures

After electrochemical cycling the battery and EIS measurement were carried out, a postmortem procedure to harvest the anode electrodes of the battery was carried out. The batteries were dismantled to harvest the electrodes for further characterization. Analytical tools such as SEM, X-rays diffraction, X-rays photoelectron spectroscopy (XPS) and FTIR were used in the materials characterization of the harvested electrodes. The flowchart in Figure 3.4 shows the battery pack dismantling procedure.

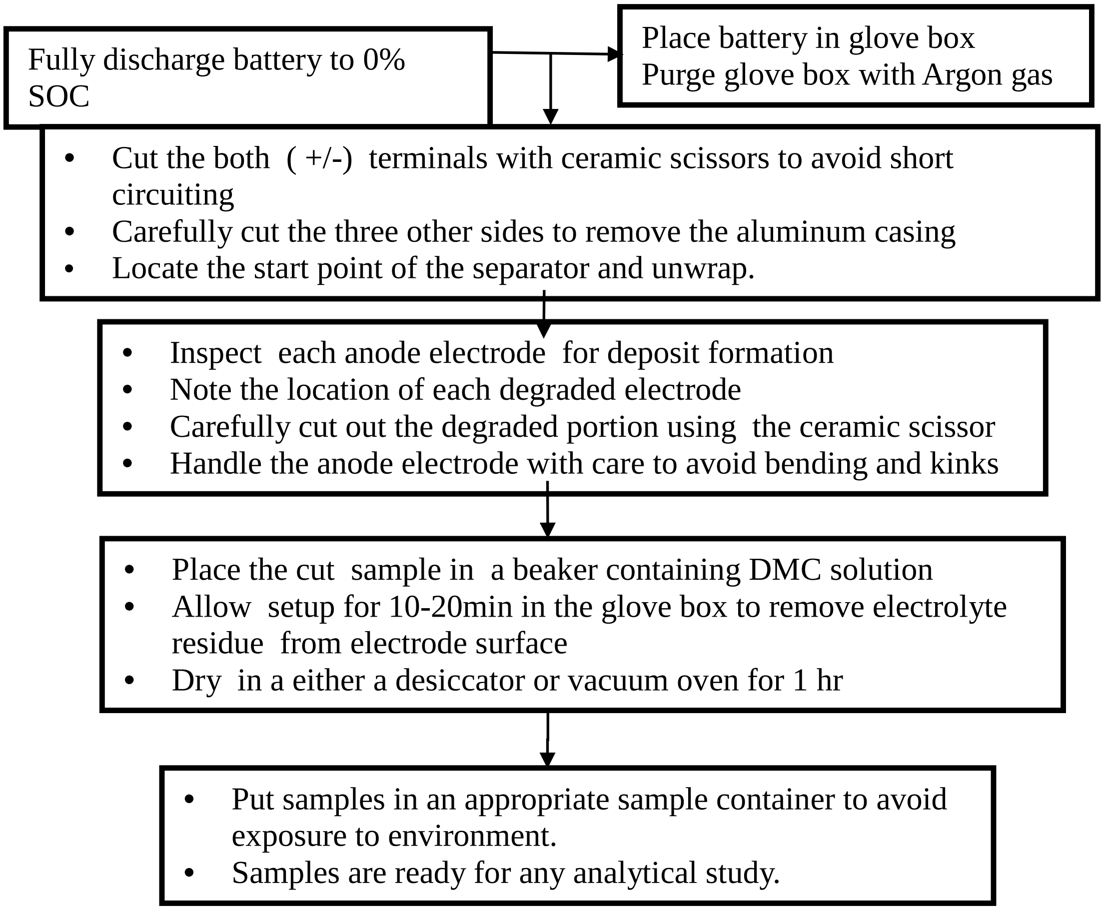

Fully discharge battery to 0% SOC

Place battery in glove box
Purge glove box with Argon gas

- Cut the both ( +/-) terminals with ceramic scissors to avoid short circuiting
- Carefully cut the three other sides to remove the aluminum casing
- Locate the start point of the separator and unwrap.

- Inspect each anode electrode for deposit formation
- Note the location of each degraded electrode
- Carefully cut out the degraded portion using the ceramic scissor
- Handle the anode electrode with care to avoid bending and kinks

- Place the cut sample in a beaker containing DMC solution
- Allow setup for 10-20min in the glove box to remove electrolyte residue from electrode surface
- Dry in a either a desiccator or vacuum oven for 1 hr

- Put samples in an appropriate sample container to avoid exposure to environment.
- Samples are ready for any analytical study.

Figure 3.4a: Flowchart of battery dismantling battery procedure

### 3.3.2 Surface morphology and thickness of deposits

The morphologies of the aged and the baseline electrodes were analyzed using a Jeol JSM-7000F Field emission SEM. A quantitative analysis of the thickness of the formed surface layer was carried out by taking the cross sectional view (Figure 3.5) of the deposited surface layer and measuring its thickness. Sample dimensions of 15mm x 15mm were cut using a precision cutter. The samples were mounted on 45° sample holder in the SEM for the imaging process. The electrodes with side reaction deposits were selected by visual examination. A total of eight electrodes were selected from each battery to represent the range of the amount of deposit distribution. Specifically four electrodes with large amounts of deposit and the other four with small to medium amounts of deposits. For each of electrode eight (8) samples, twelve different samples were taken from different location of the electrode surface as depicted in Fig. 3.4b For each of the twelve sample ($K_i$), six different deposit thicknesses were measured. Therefore for each battery, the thickness of the deposited layer was calculated by taking the mean value as follows:

$$\sum \frac{K_i/12}{8}$$

Scatter diagrams for the data points for each electrode are shown in appendix C for the different SOCs at 4C.

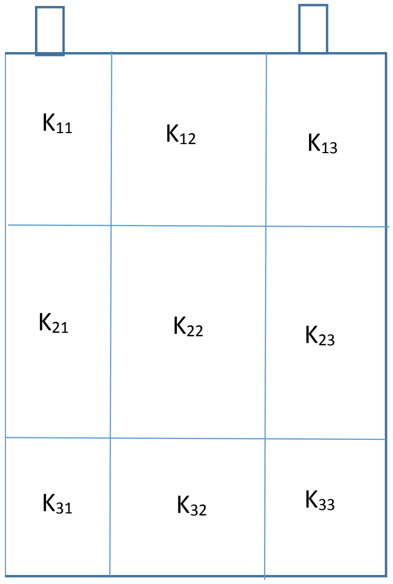

Figure 3.4b: A schematic diagram showing areas where deposit samples were taken

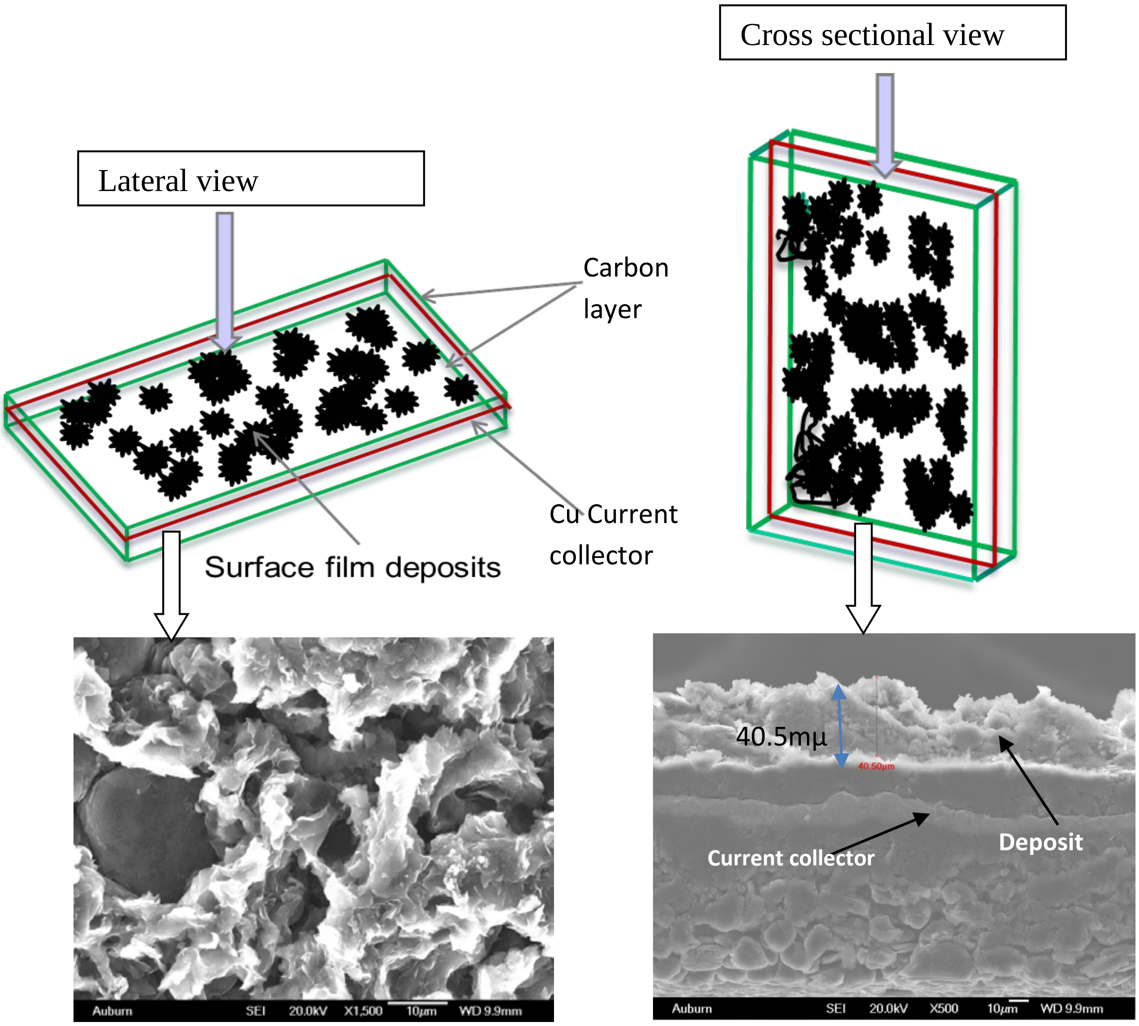

Figure 3.5: Lateral and cross sectional view of the deposit layer on anode

In the case of loss of carbon on the electrode, the electrodes with carbon particle loss were also selected by visual examination. Again, three samples, each measuring 15mm x 15mm representing a total area of 2.4% (i.e. total sample area of 675mm$^2$) of the electrode area 27840mm$^2$ (145mm x 192mm) were cut out from affected carbon loss area. The areas were measured by fitting the loss areas with discrete circles or rectangles using annotate/measurement tool on the SEM as shown in Figure 3.6. For each sample, six different area measurements were taken randomly and the total area expressed as percentage of the sample area of 225mm$^2$ and the total average carbon loss per electrode calculated by averaging the total 18 discrete areas for the three samples taken from each electrode.

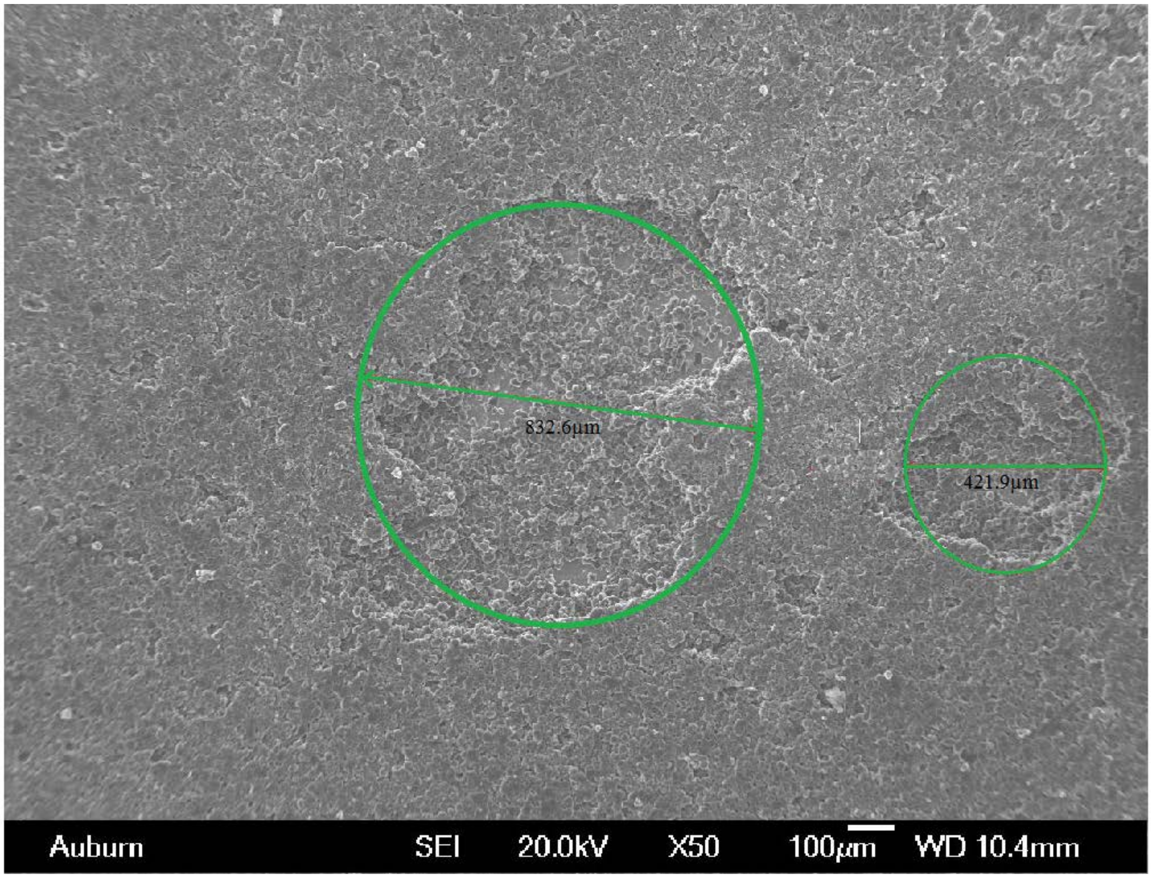

Figure 3.6 : Discrete measurement of the carbon loss area

Discrete circles and rectangular areas were calculated by finding their respective areas. The total area lost for each sample was calculated by summing the discrete areas. The number of these discrete areas varies with each sample depending on the severity of the carbon loss.

Although there was some element of bias in the selection process of the affected electrodes, the results were representative of each of the degradation mechanisms (i.e. deposit layer build-up and the loss of lithium and carbon adhesion).

### 3.3.4 Structure and surface compound analysis of the deposit layer

A Bruker D8 Discover powder diffraction was used to study the crystal structure and the phases of the electrode and that of the surface film deposits. The EVA and PDFmaint software were used to analyze and index the peaks from the aged and fresh anode electrode. To further analyze the surface film deposits composition, FTIR studies were conducted. The Bruker optics equipped with single-reflection attenuated total reflection (ATR) accessory was used. The electrode samples were adjusted such that the film deposited area was directly on the beam to provide the maximum intensity. Each spectrum was recorded by accumulating 128 scans with a resolution of 4cm. All measurements were done after purging the testing chamber with argon gas and maintained at room temperature. A total of three samples were used. The assignment of bonds were done handbook [172] of infrared spectra of inorganic compounds and from literature [173, 174].

XPS measurements for the surface film deposits were performed by using a VG ESCA Scientific Theta Probe spectrometer. Samples were prepared according to XPS sample standard (1mm x 1mm) and transferred to the XPS spectrometer inside an argon-filled sample box. The carbon 1s peak at 285eV was used as the binding energy scale reference, and the Ag 3d5/2 line at 368eV with full width at half maximum (FWHM) of 0.66eV was used to calibrate the spectrometer. To achieve high-resolution spectra, a constant pass energy of 50eV was used and the pressure in the analysis chamber was maintained at $6\text{x}10^9$ mbar. Data analyses were performed using Gaussiane Lorentzian curve fitting with Shirley background subtraction.

# Chapter 4

# Results and Discussion

## 4.0 The Effect State of Charge on Deposit Surface Layer Growth

### 4.1 Electrochemical

The measured $Q_{max}$ values of the batteries for up to 600 cycles from Figure 4.1 are plotted in Figure 4.2. The $Q_{max}$ values for both 25%-90% and 15%-80% SOC levels were similar and loss of the capacity was about 17% after 600 cycles, while the capacity fade for 5%-70% and the 5-60% SOC loss only 7.8% and 4.7% respectively. These results showed that there was over 100% difference in $Q_{max}$ when the SOC was reduced to 5-70% SOC relative to the high SOC (i.e. 25-90% SOC). The capacity of the cell cycled at 5-60% SOC was comparable (0.59Ah lower) to the baseline at 15.7Ah. These results indicate that, lowering the cell potential reduced significantly the rate at which the battery capacity fade (Fig. 4.1). To elucidate the causes of these capacity fade, materials analysis of the harvested anode electrode were carried out.

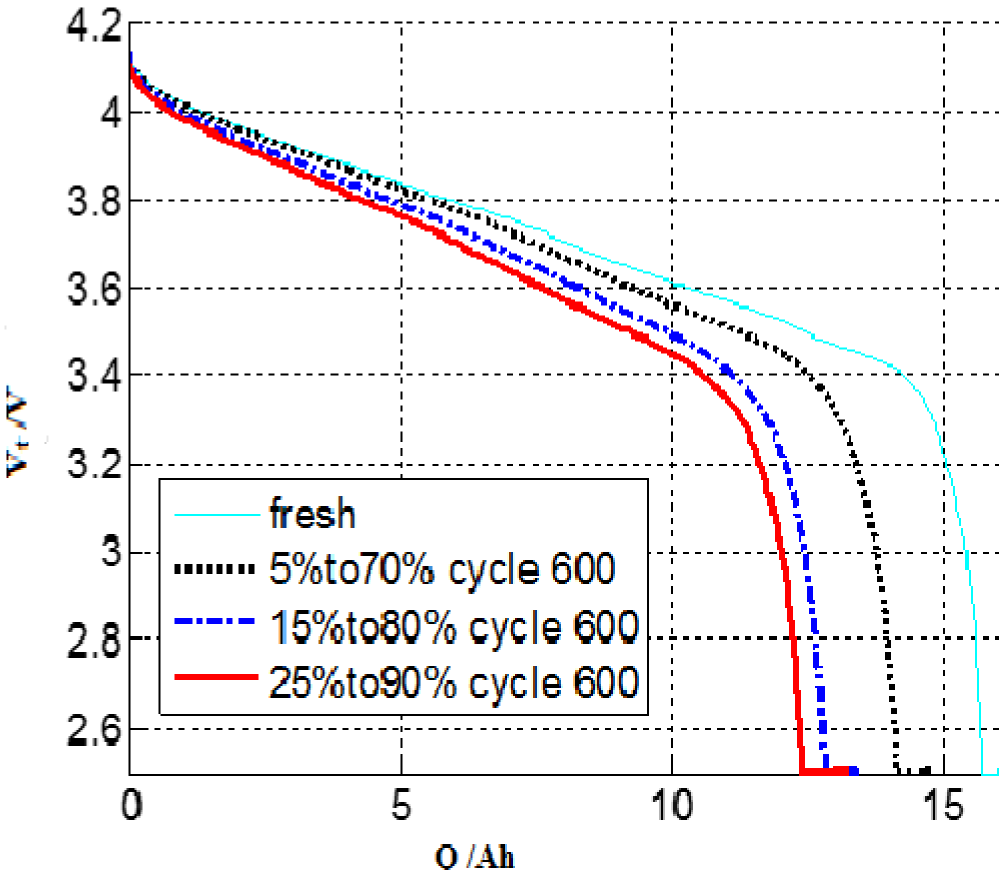

Figure 4.1: Terminal voltage Vs capacity at different SOCs and 4C rate

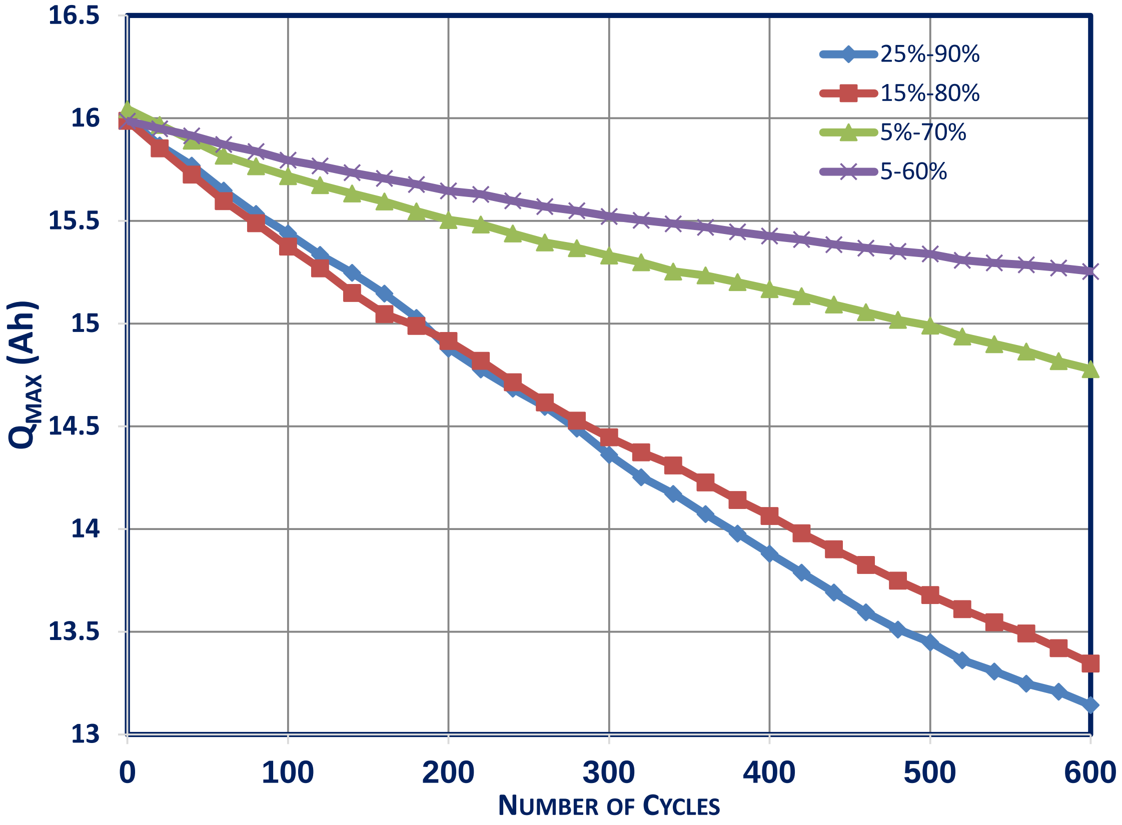

Figure 4.2: Capacity fade as a function of the state of charge for the aged batteries at different SOCs

## 4.2 Anode Electrode Materials Characterization

### 4.2.1 Deposit layer formation

SEM micrographs of the surface morphology of anode electrodes before and after aging are shown in Figure 4.3. At low magnification deposit layer formed on the batteries cycled at 5-60% SOC could not be observed, however, at high magnification (Fig.4.3b), small precipitate of deposit were observed on the carbon particles.

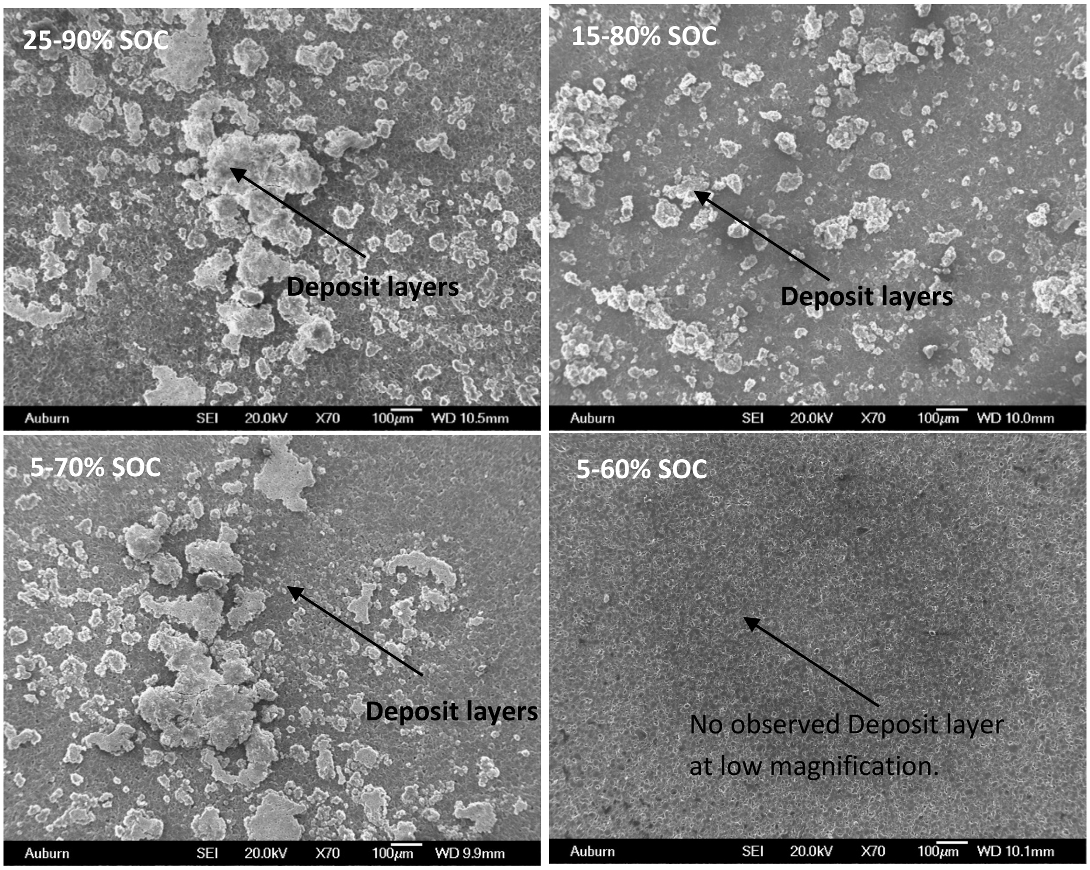

Figure 4.1a: Distribution of deposit layer on the electrode surface for the aged electrode at different SOCs

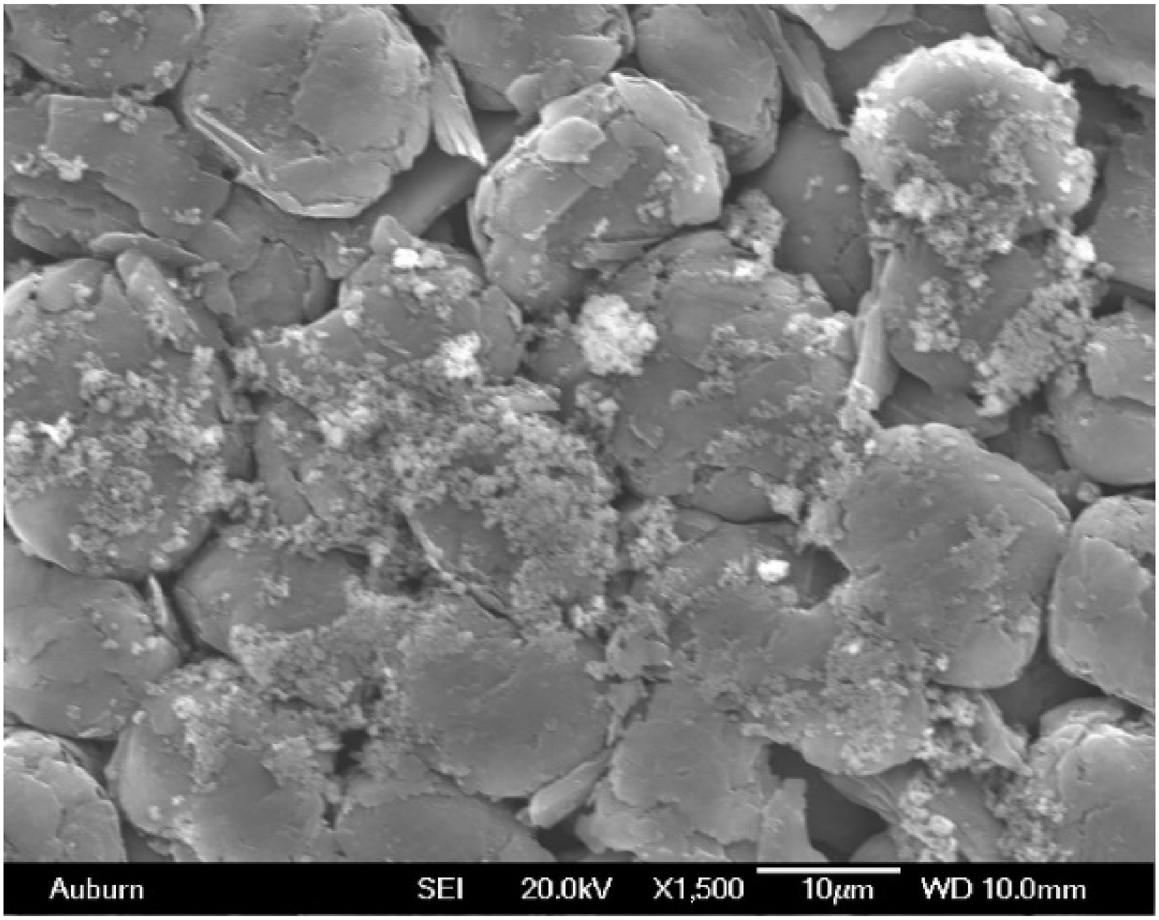

Figure 4.1b: Distribution of deposit layer on the electrode surface for the aged electrode at 5-60% SOCs

On the surface of the aged anode electrodes are the decomposition reaction products deposited on the surface of the graphite particles. The highly reactive solvent electrolyte, ethylene carbonate (EC), reported to undergo a one electron reduction reaction and was preferably solvated over DMC solvent because of it high dielectric constant and polarity [88]. The electrolyte decomposition process is initiated during the intercalation of $Li^+$ into the graphite structure, where electron transfer from the electrode to the electrolyte salt molecule initiates an autocatalytic process to produce a toxic alkyfluorophosphate, a Lewis acid, and lithium fluoride as shown in equation 26.

$$LiPF_6 \leftrightarrow LiF + PF_5 \tag{26}$$

The Lewis acid $PF_5$ reacts further with impurities of water or alcohol (Eq. 27) in the electrolyte to produce HF and $POF_3$.

$$PF_5 + H_2O \rightarrow 2HF + POF_3 \tag{27}$$

These Lewis acids trigger the ring opening and bond breaking of ethylene carbonate (EC) molecules (Eq. 28) to form various species on the surface of the electrode

$$POF_3 + EC \rightarrow CH_2FCH_2OCOOPF_2O \tag{28}$$

In particular, the decomposition species of $POF_3$ and $PF_6^-$ from $LiPF_6$ reduction react with EC. While the species $POF_3$ can react with the EC molecules to produce $CH_2FCH_2OCOOPF_2O$ and $CO_2$ in Equation 29, on the other hand, $POF_3$ and anion $PF_6^-$ can simultaneously attack the EC molecule form the anion $CH_2FCHOCOOPF_3O^-$ and a Lewis acid $PF_5$ as shown in reaction equation 30

$$CH_2FCH_2OCOOPF_2O \rightarrow CH_2FCH_2OPF_2O + CO_2 \tag{29}$$

$$POF_3 + EC + PF_6^- \rightarrow CH_2FCH_2OCOOPF_3O^- + PF_5 \tag{30}$$

The EC reduction process continues to produce a Lewis acid or salt anion (Eq. 31) at each subsequent reduction step that perpetuate the electrolyte reduction process.

$$CH_2FCH_2OCOOPF_3O^- + PF_5 \rightarrow CH_2FCHOCOOP\ F_2O + PF_6^- \tag{31}$$

At high SOC, these electrolyte decomposition reactions resulted in the formation and growth of the deposited surface layer on the surface of the graphite electrode (Figure 4.3) to form non-uniform agglomerates. The presence of these reaction products on the surface could block the pores of the anode electrode and retard the lithium ions diffusivity to the carbon anode surface. Figure 4.3 shows that the sizes and amounts of these agglomerates were dependent upon SOC and higher for the higher SOC levels, which could be due to the increased electrolyte decomposition at the higher potential during charging. At the low SOC level (5% -70%), the deposit layers were isolated. A much smaller deposit was observed on the 5-60% SOC cycled cell that could only be seen at higher magnification compared to the higher SOC ranges. The electrolyte between the separator/electrolyte interfaces for the cells tested from 25% to 90% SOC were dry as compared to those tested at 5% to 70% SOC, which was an indication of the depletion of electrolyte used in the decomposition reaction process. The continuous electrolyte reduction reaction with $Li^+$ will result in the depletion of recyclable lithium.

### 4.2.2 Effects of deposit surface layer

Lithium ion batteries electrode employs particles with pores to increase the active area between the electrolyte and the electrode to facilitate the electrochemical reaction process. A deposited layer on the surface of the active carbon materials thus blocked the electrode pores and also decreased the active surface area of the electrode. The result was a rise in the overall battery impedance. The Nyquist plots of the experimental impedance spectroscopy along the equivalent model fits results for the different SOC levels are shown in Figure 4.4.

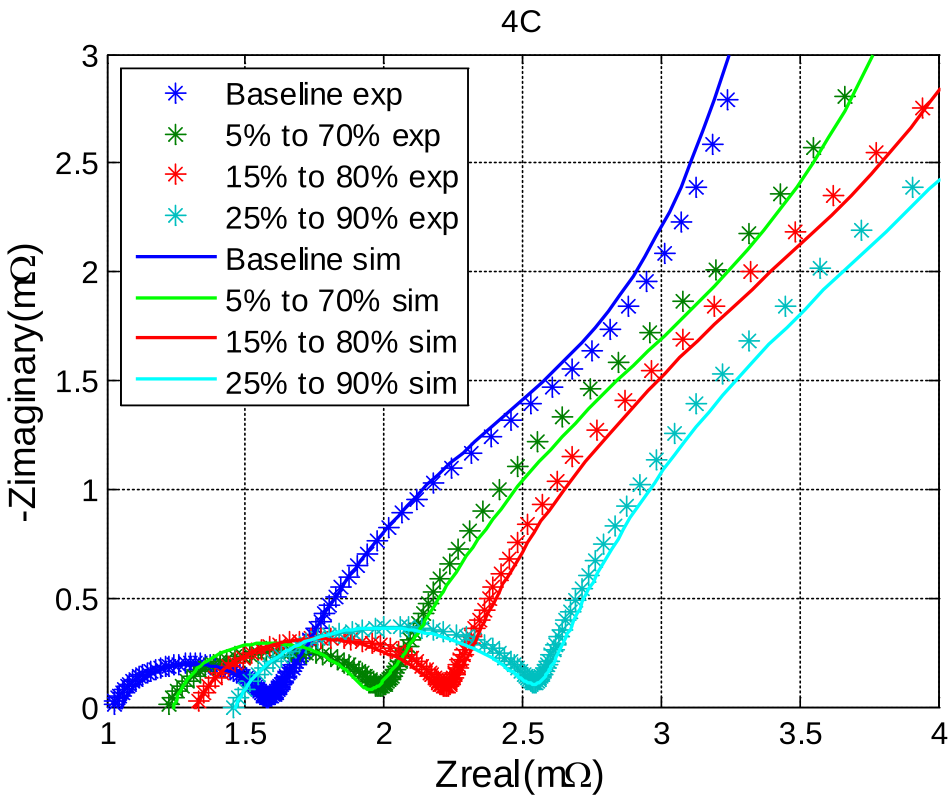

Figure 4.2: Comparison of Impedance for the aged batteries cycled at the various SOCs

The plots consist of two parts, a semicircle and a linearly increasing slope. The radius of the semicircle presents the SEI resistance, while the slope was mostly determined by diffusion effects of ions in solid. The increase in radius of the semicircles with cycling implies an increase in the SEI resistance and the amount of this growth is larger as the SOC level increased. At the same time, the high frequency intercept, which corresponds to the Ohmic resistance, increases with cycling due to the decrease in ion conductivity of the electrolytes, due to electrolyte compositional changes through the depletion conducting species [65]. The overall battery impedance was comprised of many specific battery component/interface resistances; i.e. the $Li^+$ charge transfer resistance between graphite/electrolyte interface ($R_c$), the Ohmic resistance ($R_o$) and the SEI layer resistance ($R_{sei}$). To extract these resistances, the equivalent circuit model (Figure 3.3) based on the impedance characteristics were used to extract these parameters that represent different electrochemical properties occurring in the battery. The extracted resistances parameters are plotted in Figure 4.5. The resistances tend to increase as the lower and upper end of the SOC were raised. Particularly, the increase in the charge transfer resistance was the largest.  The increases in the charge transfer resistance with increasing SOC level was attributed to the formation of the deposited surface layer on the graphite particles, which formed in greater amounts for the higher SOC level as shown in Figure 4.3.

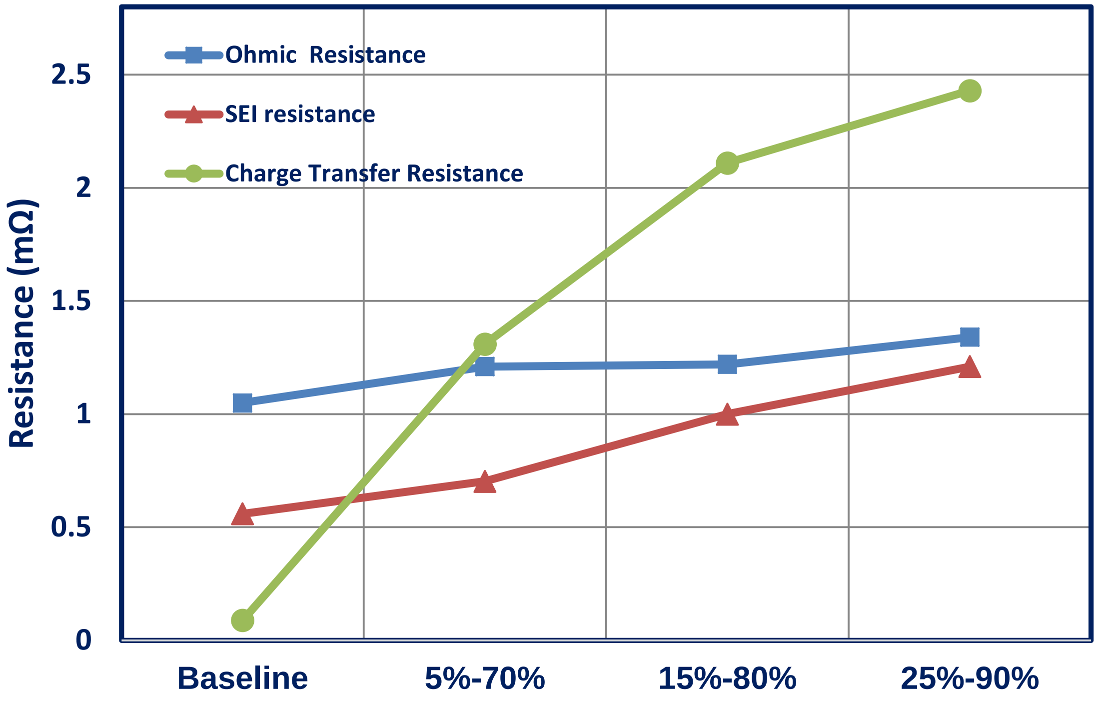

Figure 4.3: Resistance of the aged batteries extracted from the equivalent circuit model at different SOC

### 4.2.3 The growth of the deposit layer

The thicknesses of the deposit layer observed among the different SOC levels were measured from cross sectional views of the anode electrode as shown in Figure 4.4 and are plotted in Figure 4.5 for the various SOC levels. The measured deposit layer thickness shows an average thickness of 56µm for the high SOC range (25-90%) compared to 42µm for the 15-80% SOC range, and 27µm for the low SOC range (5-70%). The deposit thickness from the 5-60 % SOC were thinner compared to the higher SOC, its thickness could not be measured using the annotation tool in the SEM. However, the thickness were estimated be between 100nm and 1µm. The growing deposit layer was established to influence directly the transfer resistance during lithium intercalation into the graphite crystal structure, as shown in Figure 4.6. Interestingly, the SEI resistance appeared to not be affected significantly by the growing deposit layer at the graphite /electrolyte interface (Fig.4.6), even at high SOC range where the deposit thickness was much thicker. The charge transfer resistance, from the analysis, was the dominate factor compared to the Ohmic and SEI resistance to the overall battery impedance.

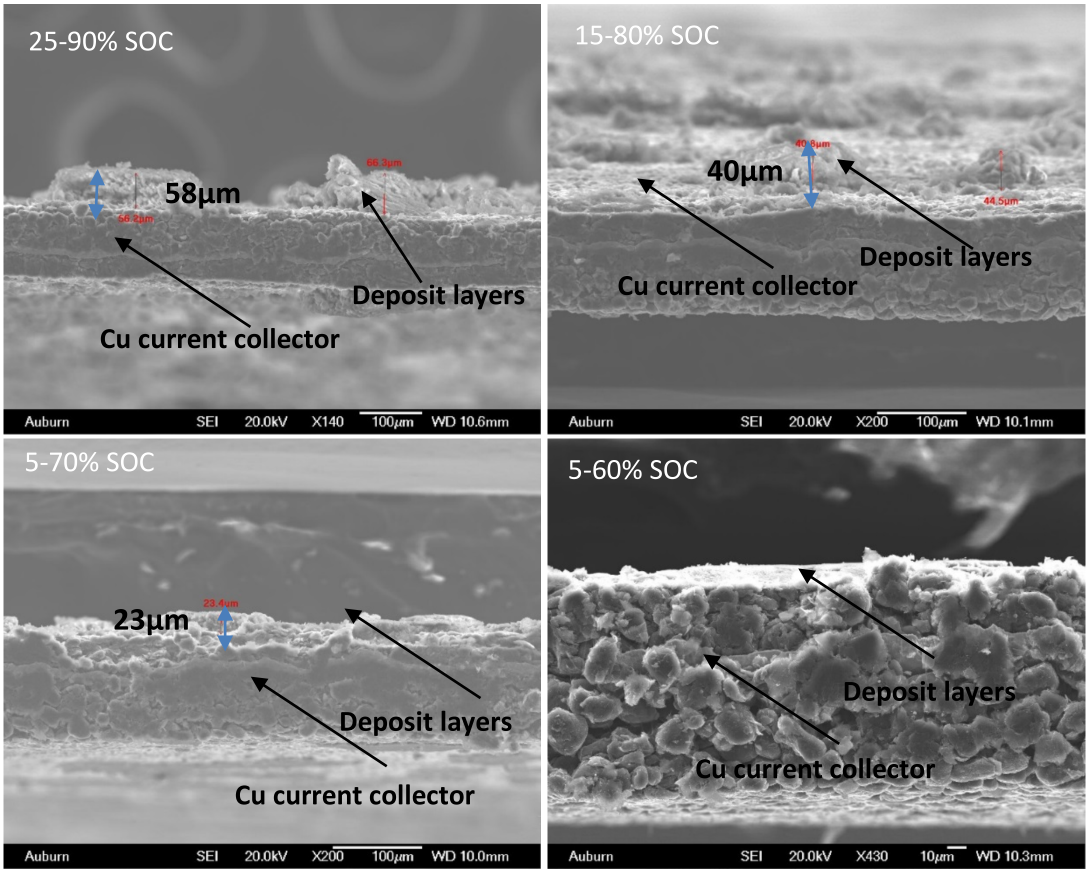

Figure 4.4: Cross sectional view of the deposit layer on the graphite particles for the different SOCs

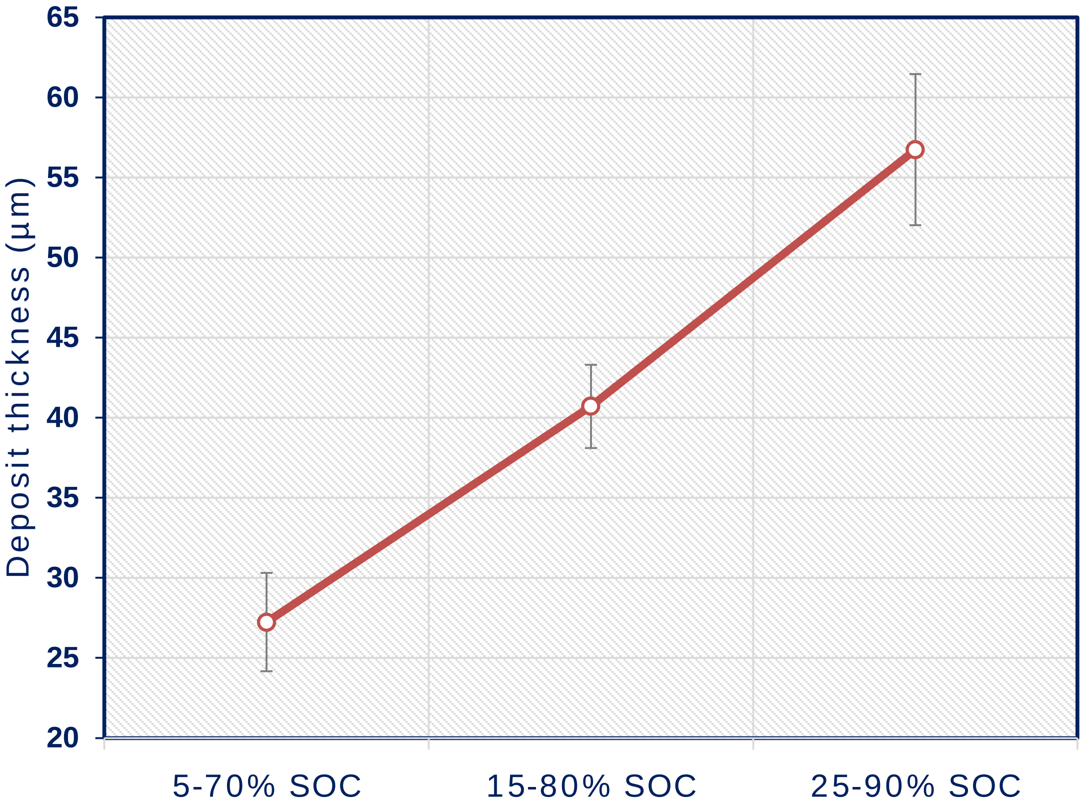

Figure 4.5: A measurement of the deposit layer thickness form on the anode for the different state of charge

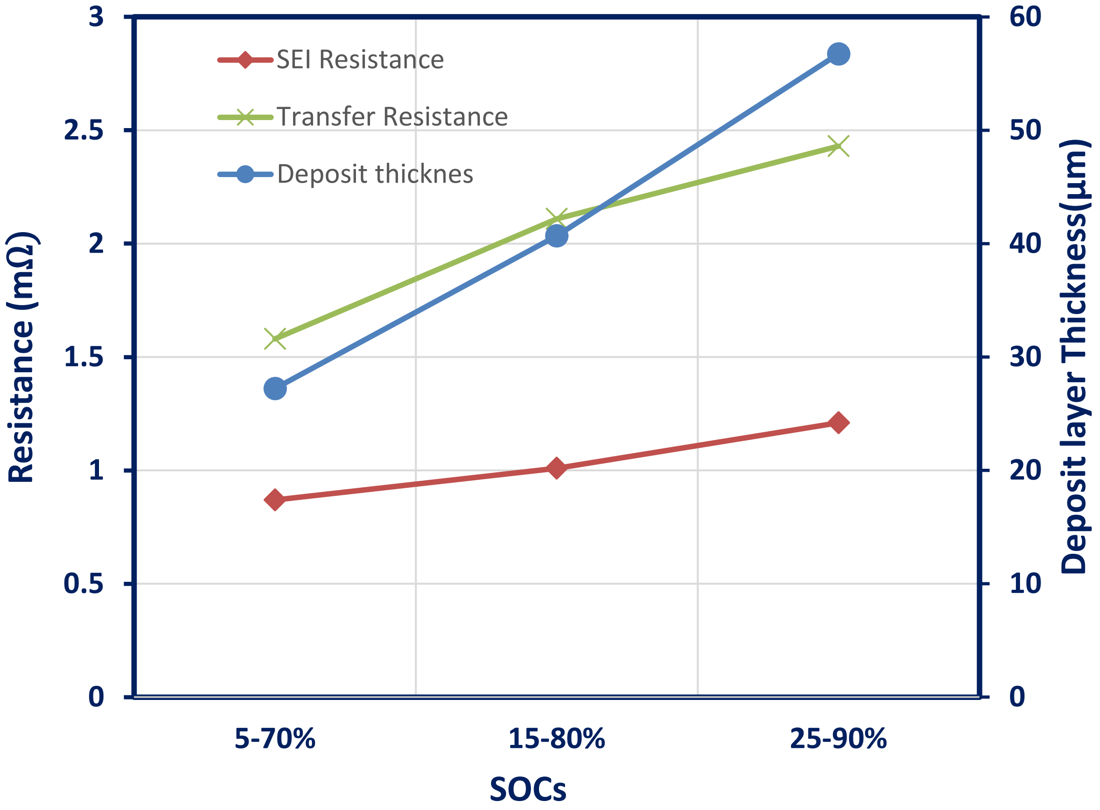

Figure 4.6: A plot showing the relationship between the deposit layer and the resistance observed from the equivalent circuit model

### 4.3 Composition of the Deposit Layer

4.3.1 X-ray diffraction analysis

The XRD spectra for the anode electrode showed a peak pattern associated with carbon and the copper current collector as indexed in Figure 4.8 where the peak (002), (101), (110), (102), and (100) are carbon peak pattern. On the other hand, the set of peak pattern (111), (200), (220) and (311) all present the copper current collector. The aged anode had two new phases in addition these set of peaks for the carbon and the copper current collector.

These additional phases emanated from the surface layer from the electrolyte decomposition products. The two additional peaks (64° and 78°), as shown in Figure 10, were attributed to the presence of the species LiF.

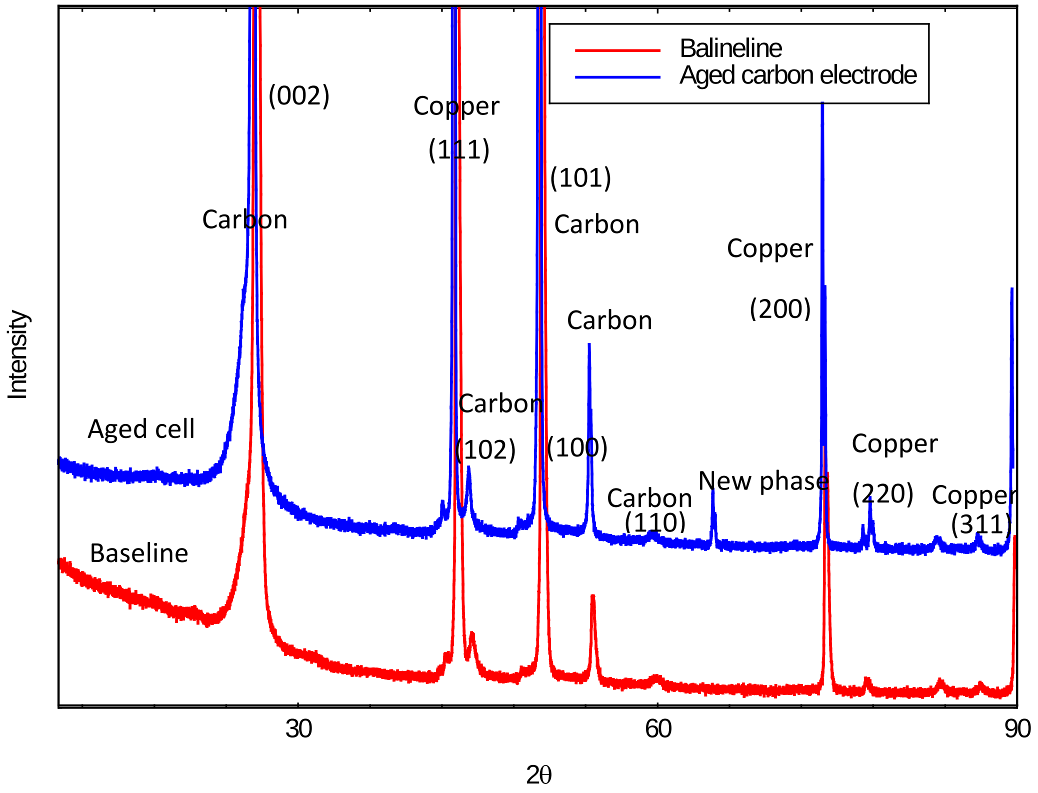

Figure 4.7: X-rays diffraction spectra for aged and baseline for the anode electrode showing a formed new phase on the aged crystal structure of the graphite.

### 4.3.2 Deposit layer composition analysis with FTIR

The deposited surface film was analyzed further with FTIR and XPS to identify the surface compounds constituting the deposited surface film layer. As shown in Figure 4.9, the absorption bands at 1750 cm$^{-1}$ represent the stretching vibration of C=O in EC, while those at 1300 cm$^{-1}$ and 1450 cm$^{-1}$ are the asymmetric stretching vibration of the C-O-C and $CH_2$ bending vibration of decomposition products of the electrolyte solution, respectively [21]. The main chemical constituents of the SEI layer in the $LiPF_6$ – EC/DMC solution are $ROCO_2Li$ and $Li_2CO_3$ [22], which generally have spectra at 1600 $cm^{-1}$ and 1300 $cm^{-1}$ for $ROCO_2Li$ and 860 $cm^{-1}$ and 1375 $cm^{-1}$ for $Li_2CO_3$. The FTIR analysis indicates that the chemical constituents of the deposited surface film layer are the same as those in the SEI layer from the electrolyte decomposition reaction lithium on the surface of the anode electrode.

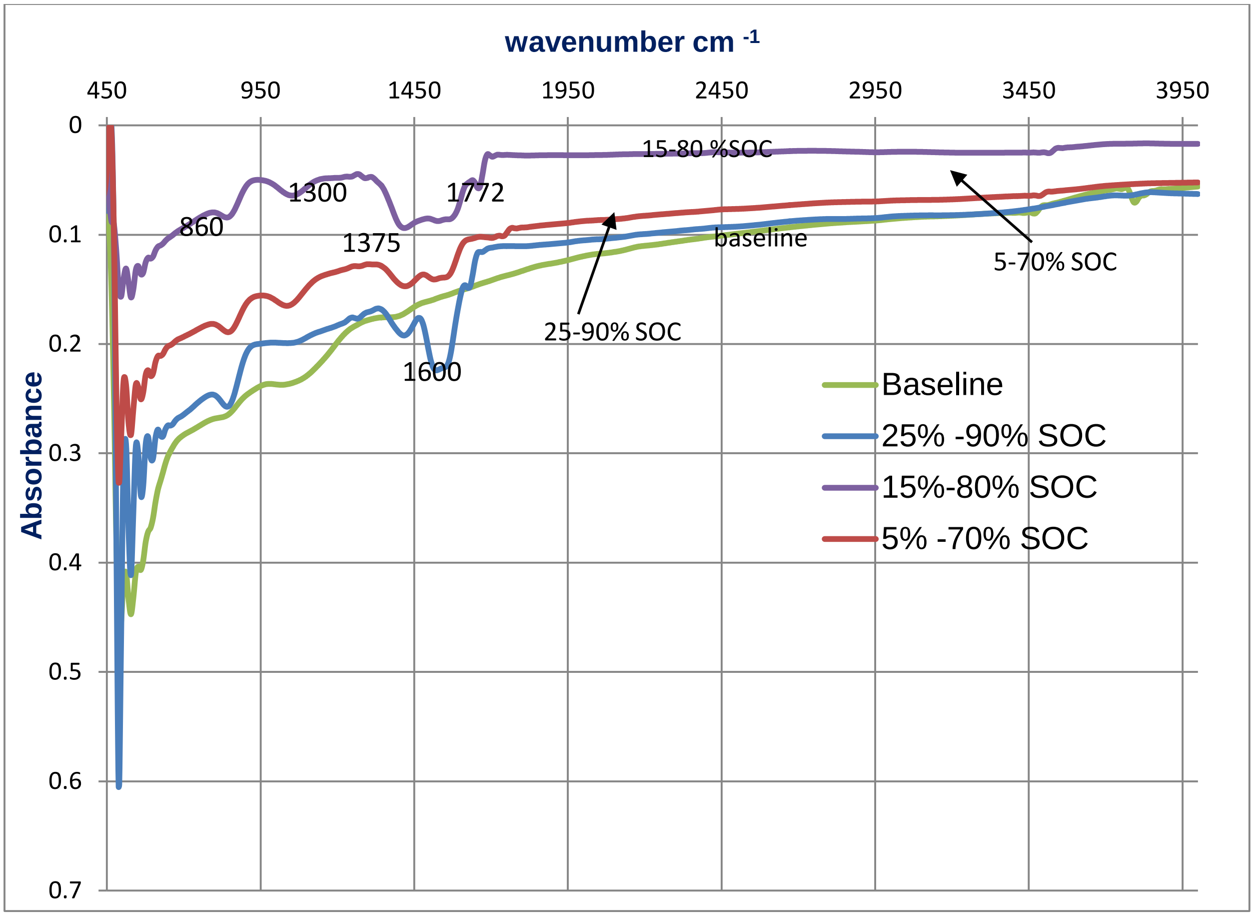

Figure 4.8: FTIR of surface compounds of the deposit surface layer

### 4.3.3 Deposit layer composition analysis with X-ray photoelectron spectroscopy

The baseline for the carbon anode clearly showed a graphite peak at 284.5eV (Fig.4.10) Some intensity was also observed in the 290-291eV range for C-F bond for the PVDF binder materials. The peak at 533eV was the most prominent peak in the O1s spectra for the aged anode electrode (Fig. 4.11). Furthermore, it may be note that $Li_2CO_3$ (expected at 531.5eV) [22], and species like $Li_2O$ and LiOH (expected <530eV) [22] were detected in the O1s spectra. An increase of the Li 1s peak for the aged cell at 55.1eV which was consistent with the existence of LiF species on the deposit.

Table 4. 1: XPS elemental surface layer composition for the baseline/aged battery (At %)

| | **Li** | **C** | **O** | **F** |
|---|---|---|---|---|
| Baseline cell | 40 | 26 | 33 | 1 |
| Aged cell | 44 | 26 | 28 | 2 |

The electrolyte contains impurities such as $H_2O$ and oxygen. The oxygen can reduce to form lithium oxide (Eq.32)

$$\frac{1}{2}O_2 + 2e^- + 2Li^+ \rightarrow Li_2O(s) \qquad (32)$$

LiOH is formed when $H_2O$ is reduced(Eq.33) on the graphite in the presence of $Li^+$, the LiOH (Eq.34) precipitates on the graphite surface and acts as blocking agent with high interfacial resistance.

$$H_2O + e^- \rightarrow OH^- + \frac{1}{2}H_2 \uparrow \qquad (33)$$

$$Li^+ + OH^- \rightarrow LiOH_{(s)} \qquad (34)$$

Although the difference in the lithium amount in the baseline and the aged battery is not significant as in seen in XPS composition analysis in Tables 4.2, it confirmed that lithium resides in the deposit layer. It is worthy to mention that XPS limit of detection was about an order of 1-2nm, therefore the lithium amount in the deposit layer (i.e. 56μm) observed from XPS analysis may not represent the entire total composition of lithium residing in the deposited layer.  The observed trend however, consistent with hypothesis that recyclable lithium ions are consumed during the formation of the surface layer as the battery is aged.

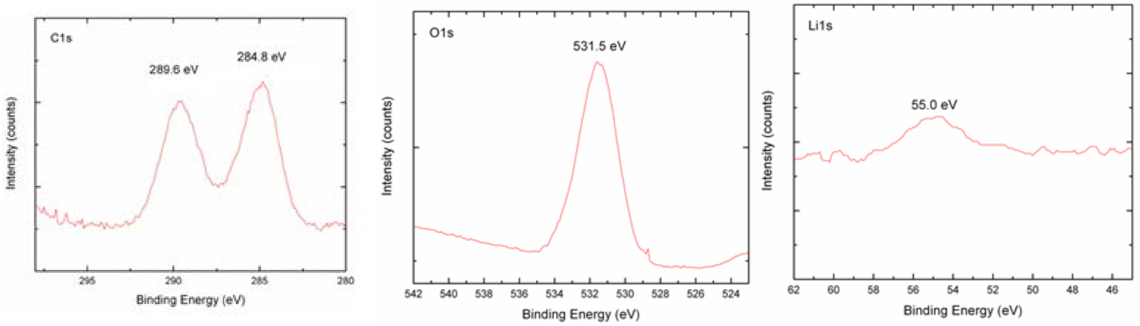

Figure 4.9: High resolution XPS spectra over the C1s, O1s, and Li1s portions regions from the baseline cell.

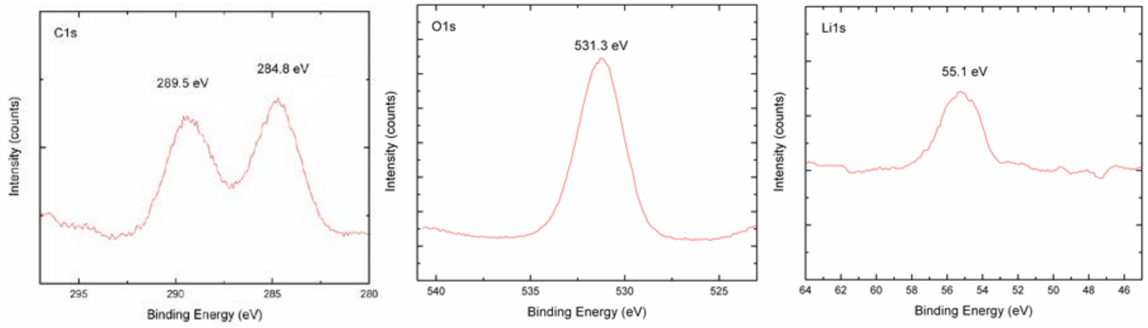

Figure 4.10: High resolution XPS spectra over the C1s, O1s, and Li1s portions regions from aged 25-90% SOC at 4C cell.

The consumed lithium were no longer available for the electrochemical reaction. Although the XPS analysis may not give a true measurements of the lithium content in the deposit layer (Table 4.1) due to its depth limitation, the lithium content it consumed was significant and directly impacted on the overall capacity fade of the batteries.

### 4.3.4 Loss of carbon particles

Figure 4.12 shows that the carbon particles were detached from the carbon electrode indicating that there was a loss of adhesion between carbon particles and between carbon particles and the current copper collector on the anode electrode surface.

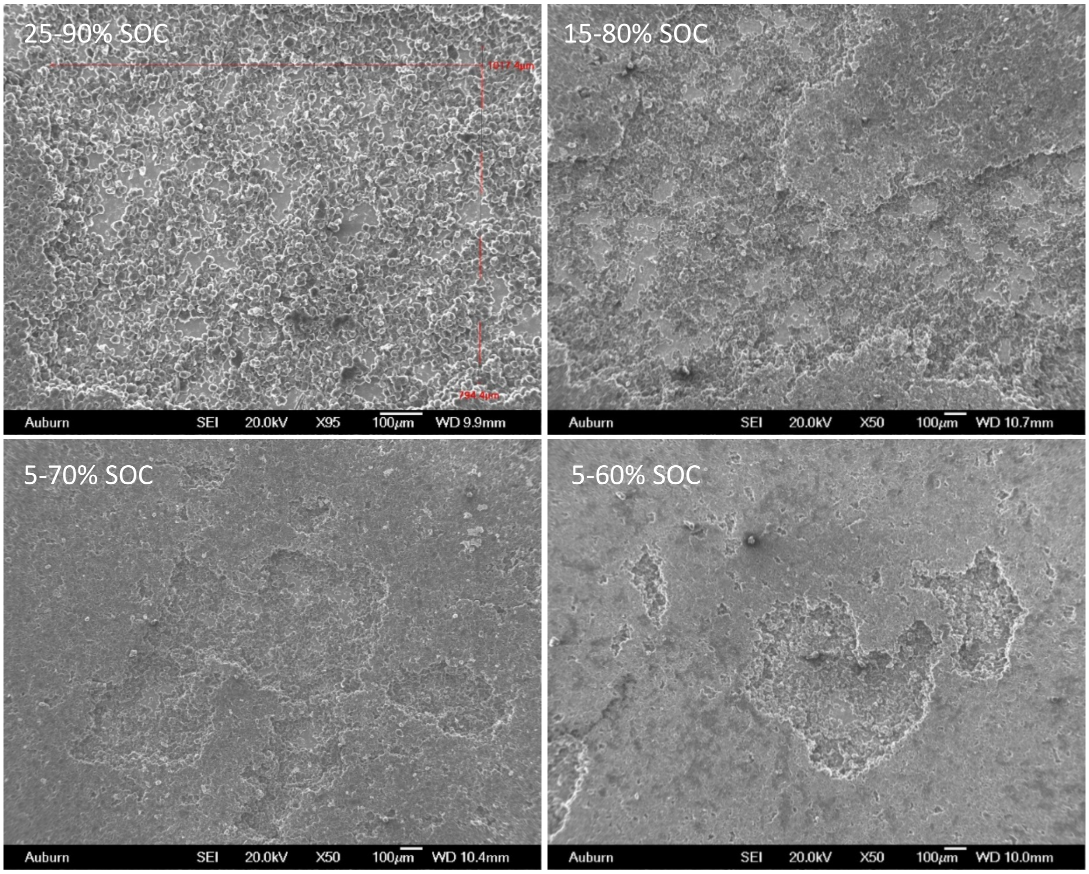

Figure 4.11: Selected example of loss of carbon particles on the electrode surface for the various SOCs

Figure 4.13 (those for the other SOCs are in Appendix A) show the volume changes for the 25-90% SOC associated charging/discharging the battery. This volume change associated with lithium intercalation/de-intercalation into the graphite structure resulted in particle expansion/contraction generated diffusion induced stresses and caused loss of adhesion of the binding material between the particles and particle and the current collector. Cycling the batteries at high charge rate - 4C, increased these volume changes, since the rate at which lithium ions were pushed into the graphite structure was greatly influenced by the charge rate which created a large concentration gradient.

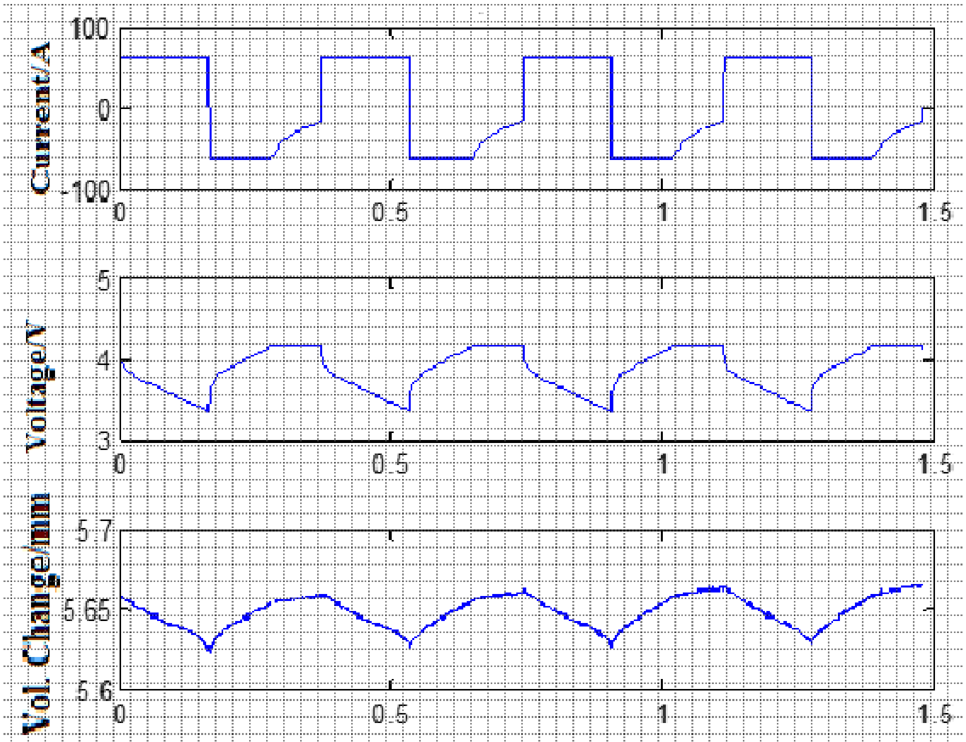

Figure 4. 12: Voltage/ current profile with corresponding cell volume change during

As a result, some of the active carbon particles lost adhesion within each particle and between the particles and the current collector could render inactive from electron-conducting matrix of the electrode and isolate from them in the electrochemical process. The loss area of these isolated carbon particles were measured and plotted for the different SOC levels in Figure 4.14. The higher SOC range (25-90%), in particular had the largest amount of carbon particles loss, and this loss decrease progressively as the SOC range is reduced. This loss in carbon particles area as a percentage of the total surface area of the anode electrode amounted to about 8% at 25%- 90% SOC level, and an even smaller area loss for the lower SOC level. However, this particle loss could significantly increase for prolonged higher cycle numbers.

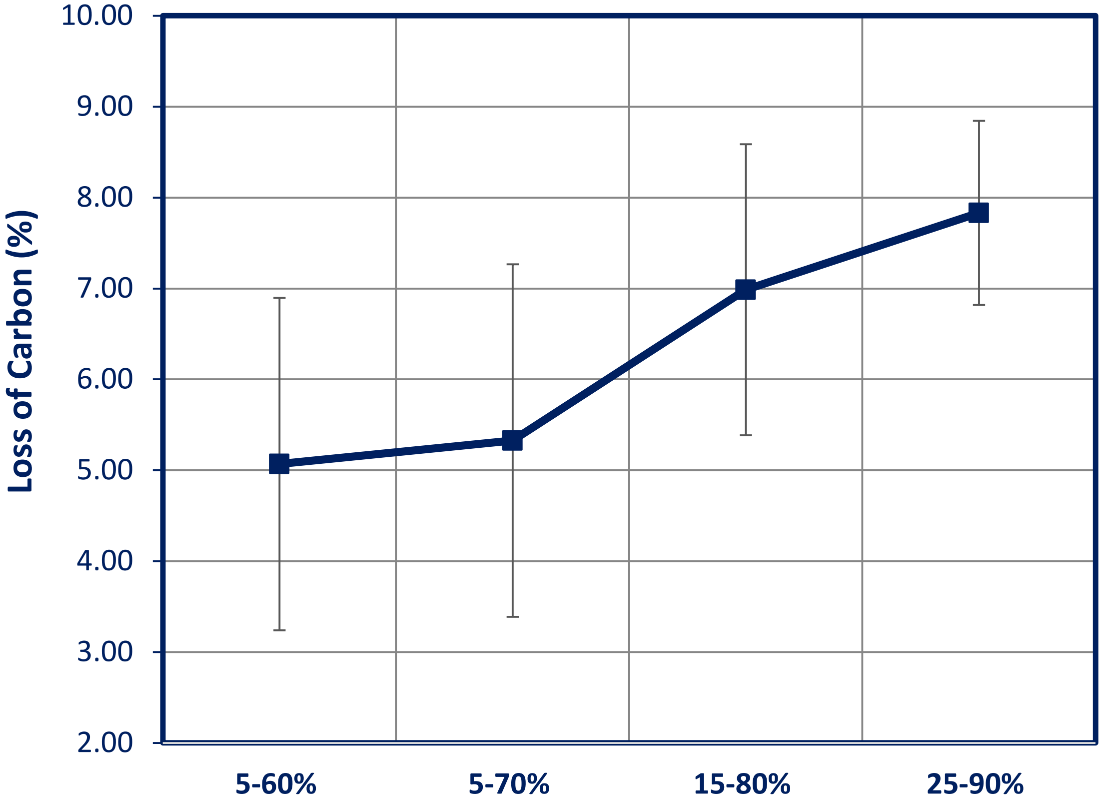

Figure 4.13: Comparison of the carbon loss area for the different SOC range

### 4.4 Characterization of the lithium content

The insertion and de-insertion of lithium into the layered graphite structure, led to volume change of the graphite anode which tends to increase the *d*-spacing between the graphite layers. When lithium intercalates into the graphite structure, it has been reported that the stacking sequence of the graphite i.e. A-B stacking prefers to change to A-A especially when d-spacing is increasing [176]. Based on this findings, the increase in lithium content in the graphite which led to an increase in lattice parameter, possibility initiated the transformation from A-B stacking sequence stacking to A-A. To investigate this, further analysis of the (002) peak (Fig. 4.15) was undertaken to understand the possible structure changes in the carbon structure for the aged anode associated with the growing deposit layer.

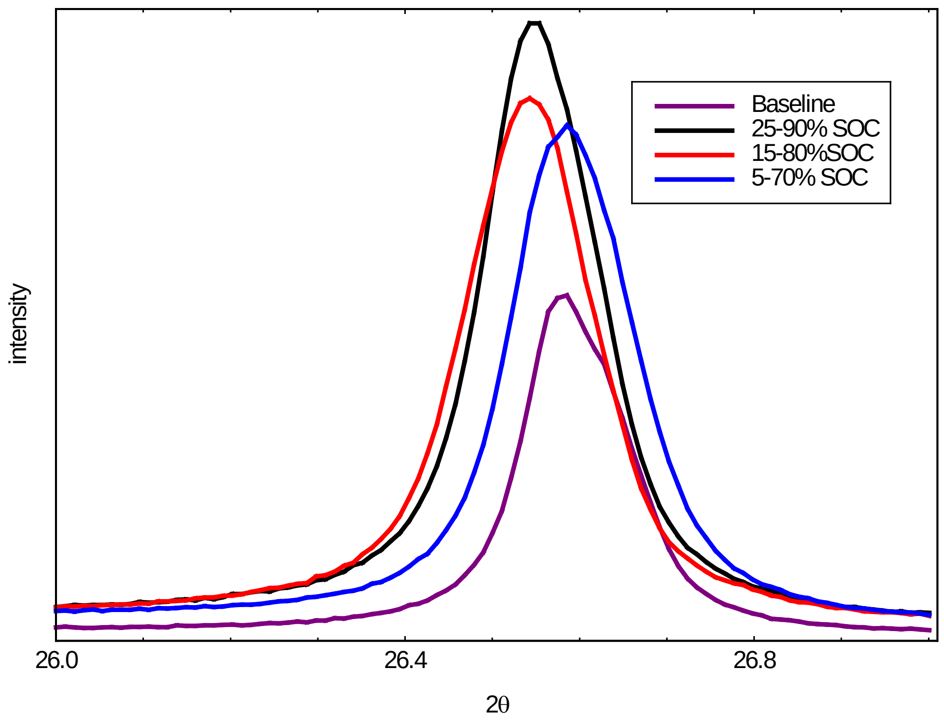

Figure 4.14: X-ray diffraction of the 002 peak for aged cell at various state of charge and baseline anode electrode

All the cells were discharged to 0% SOC (2.5V), thus some amount of lithium would remain in the graphite structure because 0% SOC does not equal to 0% Li in the crystal structure of the graphite. A total removal of the lithium content in the graphite structure would require a greater amount of energy to re-intercalate lithium back into the crystal structure. The shifts of the (002) peak to lower 2θ ° for the 25-90% SOC and 15-80% SOC relative to the baseline, implied more lithium remained in the graphite structure after discharge which correlates the increase in the *d*-spacing. Peak broadening that was attributed to the lithium content in the graphite sheets was also observed, which increased for the higher state of charge. The (002) peak for both the baseline and the aged cell had a shoulder, that was de-convoluted into two separate peaks using the Lorenz area function (Fig. 4.16). This implied that, for the graphite structure, two or a range of d-spacing were present. The existence of a range d-spacing implied that some particles had higher lithium content while other had low lithium content in the graphite electrode matrix.

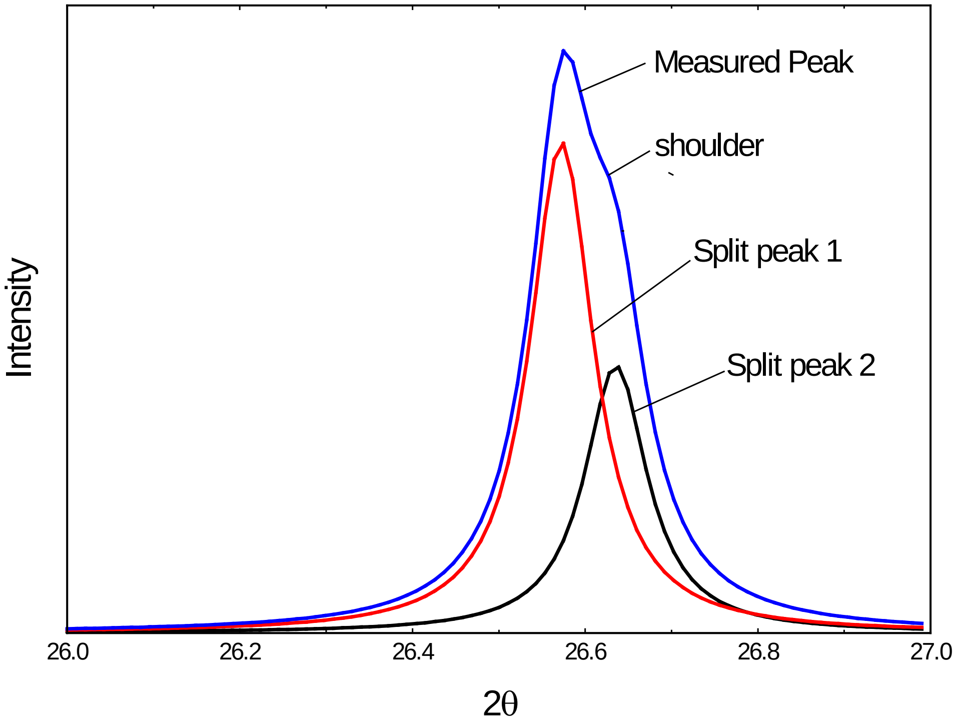

Figure 4.15: De-convoluted peaks for the shoulder on the baseline (002) peak

The lithium content in the graphite sheets which relates directly to the lattice parameter was determined for each of the aging conditions and tabulated in Table 4.1 and plotted in

Figure 4.17 for the baseline and at the various aging SOCs. There was an increase in the lithium content in the graphite for the aged anode relative to the baseline, which was an indication that some of the lithium were “trapped” in the graphite crystal structure after the discharge cycle. In the ideal case, the same level of lithium is expected to be in graphite layers for both the aged and the baseline electrode at the end of each discharged cycle. In addition, the lower $d_{002}$ values corresponding to the lower lithium content was expected not to differ from those of the baseline graphite anode. This was the case for the 70% and 80% SOC cycled batteries, the lower lithium content was statistically within those of the baseline with the uncertainty of ±0.014Å. However, for the high SOC (i.e. 25-90%), the lower lithium content significantly differed from that of the baseline. The reason for this difference could not be readily explained. The loss of adhesion between the carbon particles and that of the current collector was directly responsible for the trapped lithium in the graphite structure. The loss of carbon particles created a discontinuity in the electrical path between particle to particle contacts. In the process, these particles are isolated in the electrochemical process. The relationship between the particles loss and that of the lithium content trapped in the graphite structure shown in Figure 4.16, indicated that as a large area of the carbon particles were loss, it increased the chance of particles isolation. The net effect of the loss of carbon area was large amount of lithium trapped in these particles. This effect was great even at low SOC (70%), where the trapped lithium was significantly differed from that of the baseline.

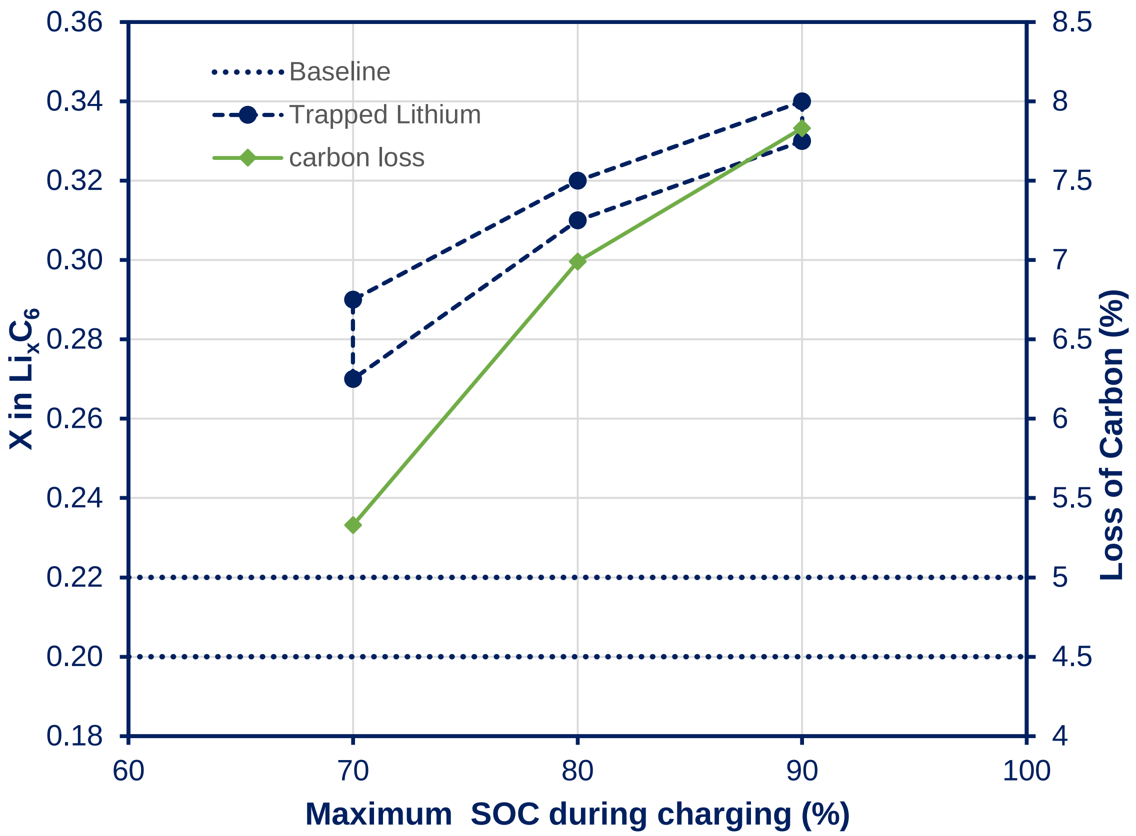

Figure 4.16: A correlation between trapped lithium in the graphite structure and the loss of carbon particles in the electrode matrix.

To estimate the amounts of lithium trapped in the graphite sheet the following assumption were made: The estimated lithium stoichiometry for the crystalline graphite: $X^{min}$ ($Li_xC_6$) =0.00 at cell assemble, while that for the crystalline graphite is: $X^{max}$ = 0.9($Li_{0.9}C_6$) at full charged that corresponds to $d_{002}$ = 3.700 [176] for the initial cycle. The lithium stoichiometry x=0.9 L( i.e. $Li_{0.9}C_6$) is usually maintained by designing the cathode electrode with greater than the theoretical amount of the positive –electrode mass, thus providing extra lithium on the cathode [180] to cater for the initial lithium ion loss due to the formation of the SEI layer. This stoichiometric for the ideal condition should be maintained. However, the occurrence of side reaction in the cell generally affects the overall anode stoichiometry, causing a reduction X<0.9 in the $Li_xC_6$ [180]. For the control cell (baseline), the composition at discharged (0%SOC) from the XRD results was $Li_{0.22}C_6$, calculated from the weighted average in Table 4.1. Although the batteries were cycled at different SOCs, they were discharged to the same voltage, 2.5V at 0% SOC, therefore the reference lithium amount in the graphite was assumed to be that in the baseline graphite sheets. The amount of lithium trapped in the graphite sheets was determined by calculating the difference between the x in the discharged baseline cell and x= 0.9 and compared to that between x in the aged discharged cell. Where x=0.9 at 100% SOC:

For example the amount of lithium trapped relative the total amount involved in the charge discharge for the 25-90% SOC is determined as follows from the weighted average of x as in Table 4.2; assuming x = 0.9 proportional to 90% and x = 0.2 proportional to 20%. For the baseline; x= 0.9-0.22= 0.68, total lithium involve in the discharge process.

Aged cell at 25-90%; x= 0.9-0.27=0.63
Amount of lithium trapped relative the total= (0.68-0.63)/0.68= 7.4%
This was done for the all the cycled batteries and in tabulated in Table 4.1.

Table 4. 2: Weighted average of lithium in the graphite sheet and the percentage lithium trapped for 002 peak from XRD studies.

| SOC | Weighted Average ( X in $Li_xC_6$) From (002) peak analysis | Lithium Trapped (%) | Peak Area |
|---|---|---|---|
| Baseline | 0.21685 | - | 213 |
| 5-70% | 0.23285 | 2.3 | 238 |
| 15-80% | 0.25375 | 5.4 | 276 |
| 25-90% | 0.27215 | 8.1 | 289 |

The XRD study showed that the aged graphite anode electrode had a greater amount of lithium in the graphite sheet compared to the expected composition of $Li_{0.22}C_6$ in the baseline at discharge. The high amount of recyclable lithium trapped in the graphite sheets for the high SOCs correlated the capacity fade reported in Fig. 4.1. For instance for the cell aged at 25-90% SOC at 4C, had a capacity fade of 17.8% which had a 8.1% lithium trapped in the graphite sheets, compared to 7.8% and 2.3% respectively for the capacity fade and lithium trapped amount for the cell aged at 5-70% SOC.

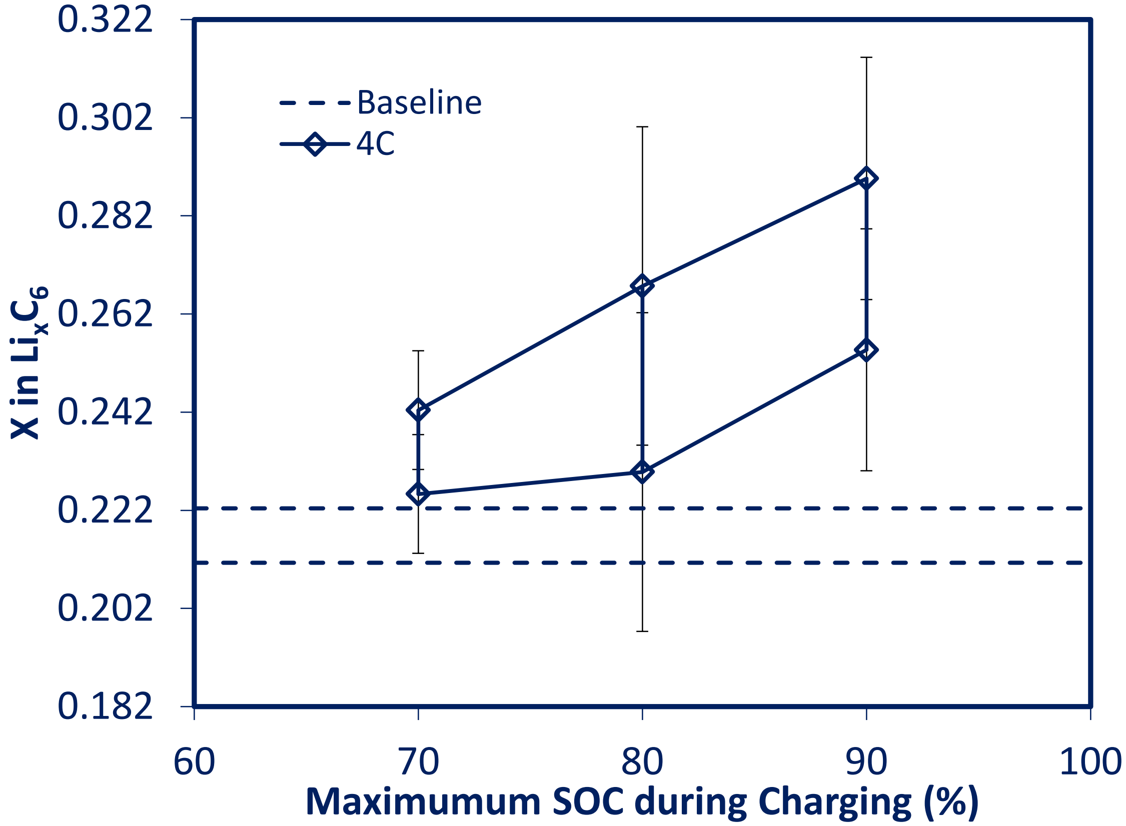

Figure 4. 17: An analysis of the lithium content x in LixC6 for the different SOC at cell

Table 4. 3: Lithium stoichiometry in the aged cells and corresponding d-spacing from analysis of the 002 peak from XRD analysis

| | d-spacing | X in $Li_xC_6$ | Literature | Peak area |
|---|---|---|---|---|
| Pristine graphite * | 3.3481 | 0 | *[176-178] | - |
| Baseline | 3.3499/3.3536 | 0.21/0.22 | 0.22[156-179] | 213 |
| 5-70% | 3.3471/3.3556 | 0.2253/0.2424 | | 238 |
| 15-80% | 3.3530/3.3608 | 0.2298/0.2677 | | 276 |
| 25-90% | 3.3588/3.3614 | 0.2547/0.2898 | | 289 |

## 4.5 Summary of Findings

- **High SOC (25-90% and 15-80%)**
- A thicker deposit layer formed on the surface of carbon particles.
  - There was a difference of 14µm of deposit thickness between the 25-90% and that of 15-80% SOC.
  - Increased in the charge transfer resistance attributed to thick deposit layer.
  - There was a direct link between the capacity fade during cycling and the progressive build-up deposit layer thickness.
  - With the 25-90% cycled cells recorded 17.8% capacity fade and deposit thickness of 56µm while the 15-80% recorded a capacity fade of 16.8% with a deposit thickness of 42µm.
- The loss of carbon particles adhesion was attributed to cycling the batteries at high charge rate of 4C due to large lithium concentration gradient that led to some particles isolation in the electrochemical process.

        - After 600 cycles carbon particles were detached were less than 8% the total surface area of the anode electrode surface area.
        - This particle loss could significantly increase for prolonged higher cycle numbers
        - The loss of carbon particles created a discontinuity in the electrical path from particle to particle.
        - A discontinuity in the electrical path and the isolation of the particles in the electrochemical process resulted in trapping of lithium in some particles after discharge.
        - Cells aged 25-90% SOC and 15-80% had a 8.1% and 5.4% lithium trapped in the graphite sheets respectively.

- **Low SOC (5-60% and 5-70%)**
- A thinner (26µm) deposit layer was formed compared to batteries were cycled at higher SOC.
    - Increased in the charge transfer resistance was lesser than that observed at high SOC attributed to a much thinner deposit layer.
    - A more than 100% difference in the capacity fade between the high SOC aged cells that of the lower SOC aged cells.
    - The cell cycled at 5-60% SOC had little degradation and was almost comparable to the capacity of the baseline batteries.
    - A considerable reduction in the loss of carbon particles adhesion at low SOC, with the 5-60% cycled cells recording a no loss

  - A lesser amount lithium trapped in the crystal structure of the graphite at low SOC, due less carbon detachment from the electrode matrix, which is consistent with capacity fade.

## Chapter 5

### 5.0 Effect of Charging Current

The porous anode electrode with its complicated geometry, when charged at high current (4C) causes different parts of the electrode to have different voltage drops. This implies that the intercalation process will no longer be uniform. Therefore on charging, parts of the electrode could reach Li deposition potentials, whereas other parts may not have reached the potential for the lowest intercalation stage.

In this chapter, the effects of charge rate on the various aging parameters identified in chapter 4 are presented. The 4C charge rate was chosen to accelerate the aging process, however at this high C-rate, $Li^+$ could either deposit as metallic lithium on the surface of the anode or be readily available for electrolyte decomposition reaction to form the surface film layer. There was the need to investigate how charge rate affected the formation and growth of the deposit layer, the loss of recyclable lithium and carbon particles as a function of the cycling battery potential:  at 25-90% and 5-70% SOC.

### 5.1 Capacity Fade of Aged Batteries

The capacity fade for the batteries cycled at the two SOC levels are shown in Figure 5.1. The $Q_{max}$ results indicated that reducing the charge rate while cycling the batteries at high SOC does not significantly reduced the irreversible capacity of the cell. At 4C, the batteries had 17.8% compared to a 15.7% fade at 2C. On the other hand, for the cells cycled at lower potential ( i.e. 5-70% SOC), the charge rate impacted significantly on the capacity, with a sharp drop in the capacity as the charge rate was increased to 4C. At low C-rate (2C), the cell’s capacity was comparable to the baseline cell of 15.7Ah (4.6%

loss). The observed capacity fade correlated with the impedance of the batteries for the two SOCs presented in the Figures 5.2. and 5.3

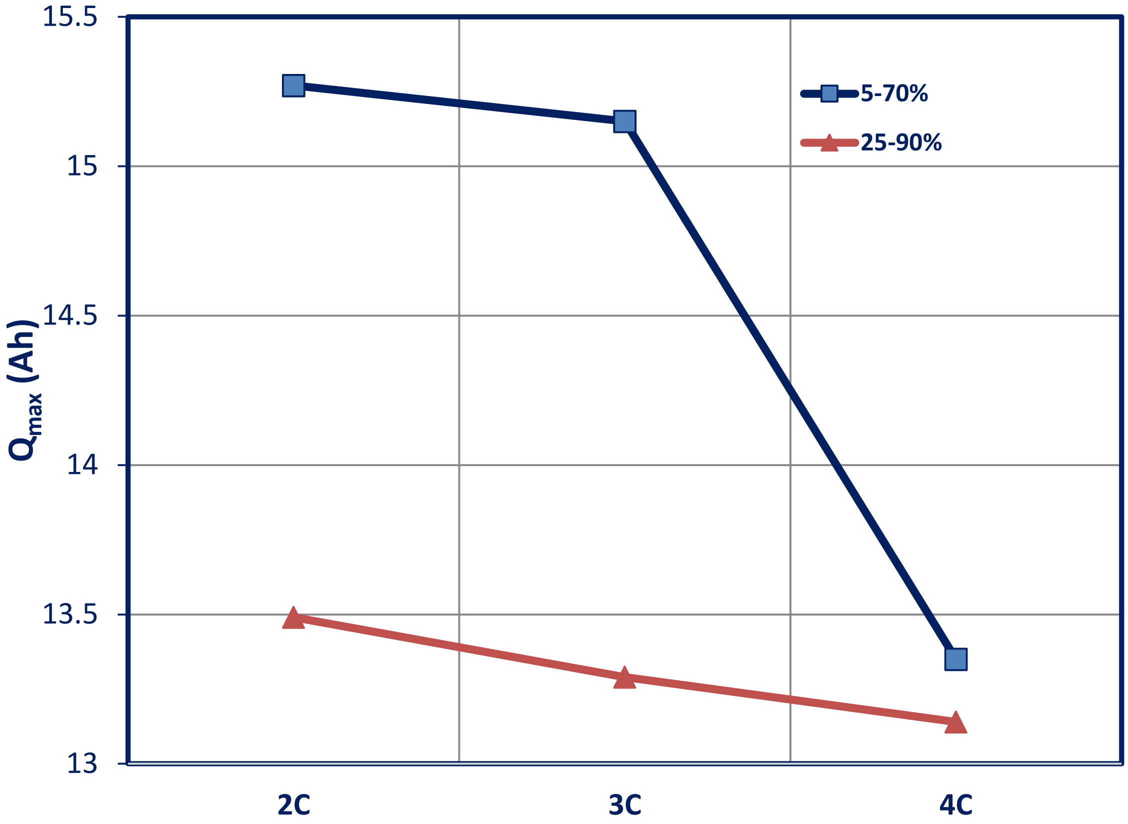

Figure 5.1: comparison of capacity fade for cells aged at 25-90% SOC and 5-70% SOC as a function for the charge rate.

For the 25-90%, the impedance increased progressively as the charge rate was increased from 2C to 4C. On the contrary, for batteries cycled at 5-70% SOC, there was no significant diffrence in the impedance between the 2C and 3C, while that for the 4C increased significantly which is consistent with the results from the capacity fade.

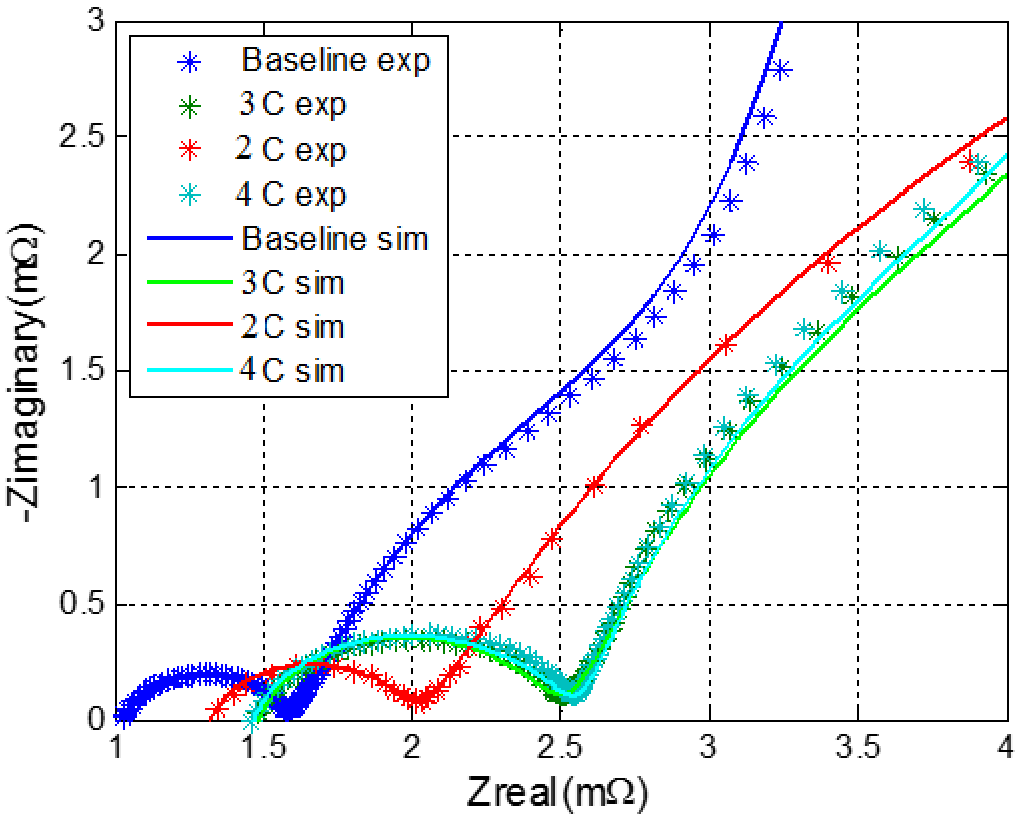

Figure 5.2: Impedance with fit from model for the cell at 25-90% SOC as a function of charge rate

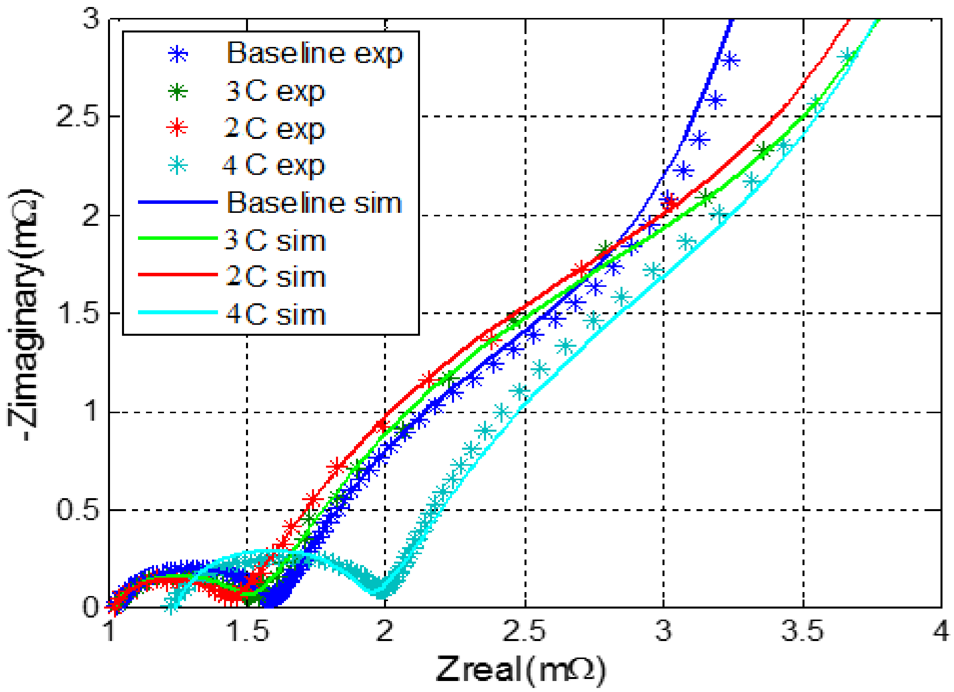

Figure 5.3: Impedance with fit from model at different charge rate for the 5-70% SOC

The extracted resistances from the equalvalent circit model: Ohmic, SEI , and charge transfer resistnace for the two SOCs are plotted in Figures 5.4 and 5.5 show a progressive increases in all the resistance. The charge transfer resistance again had highest increase as the charging current was increased. A comparison of the charge transfer resistance for the 25-90% SOC and that of the 5-70% SOC is plotted in Figure 5.6 for the diffrence charge rates. For the high SOC, the charge transfer resistance as a function of the charge rate was nearly flat thus did not vary much as the charge rate was increased. The 5-70% SOC recorded a sharp increase from 3C to 4C. The expalination for these observed increases in the charge transfer resistance will become apparent from the materials characterization the anode.

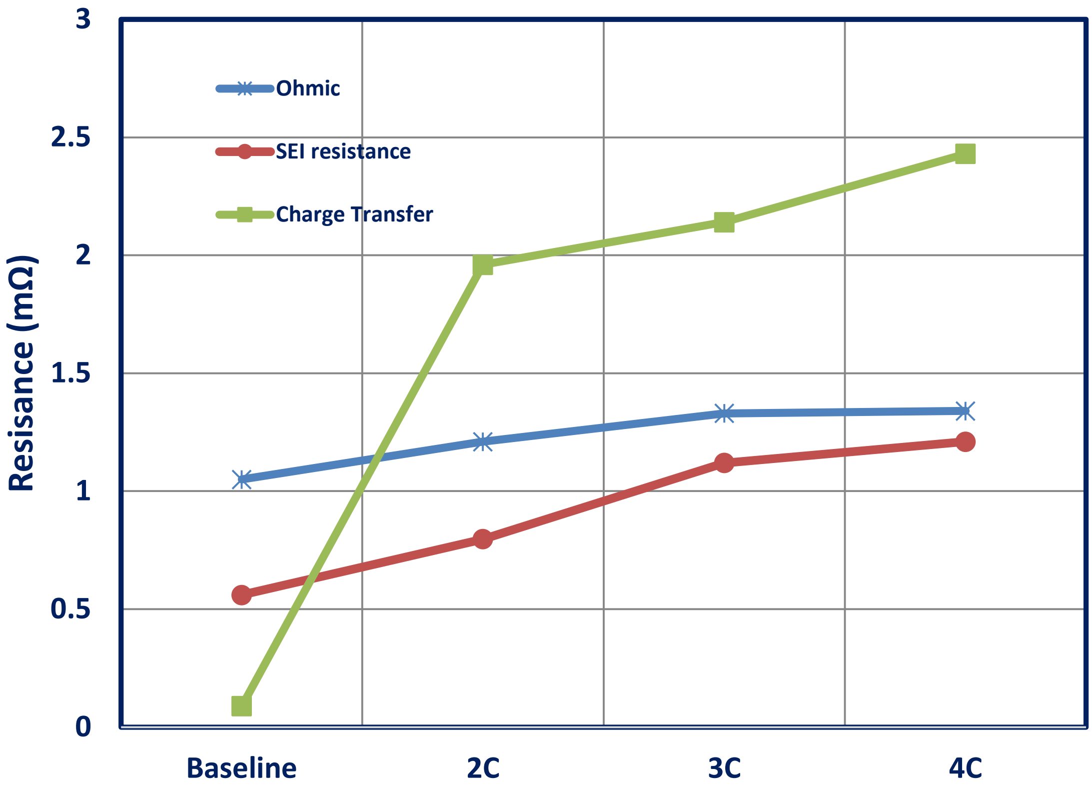

Figure 5.4: Extracted resistance from equivalent circuit model for cell aged at 25-90% SOC at different charge rate

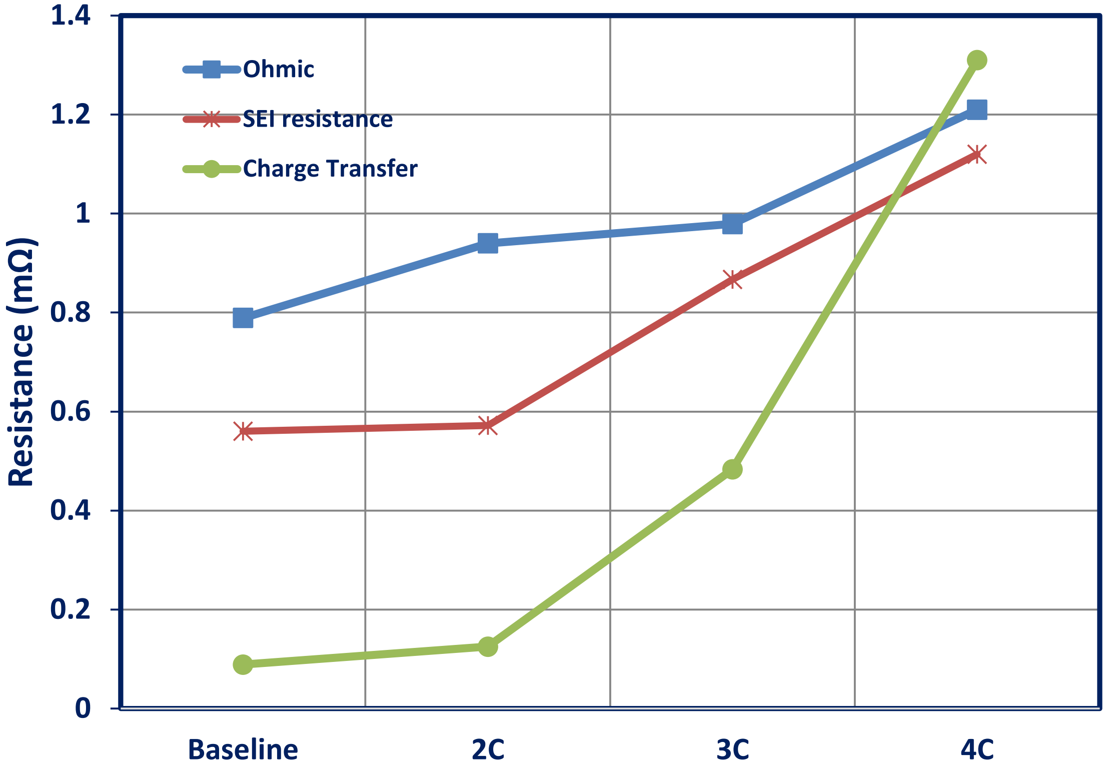

Figure 5.5: Extracted resistance from equivalent circuit model for cell aged at 5-70% SOC at different charge rate

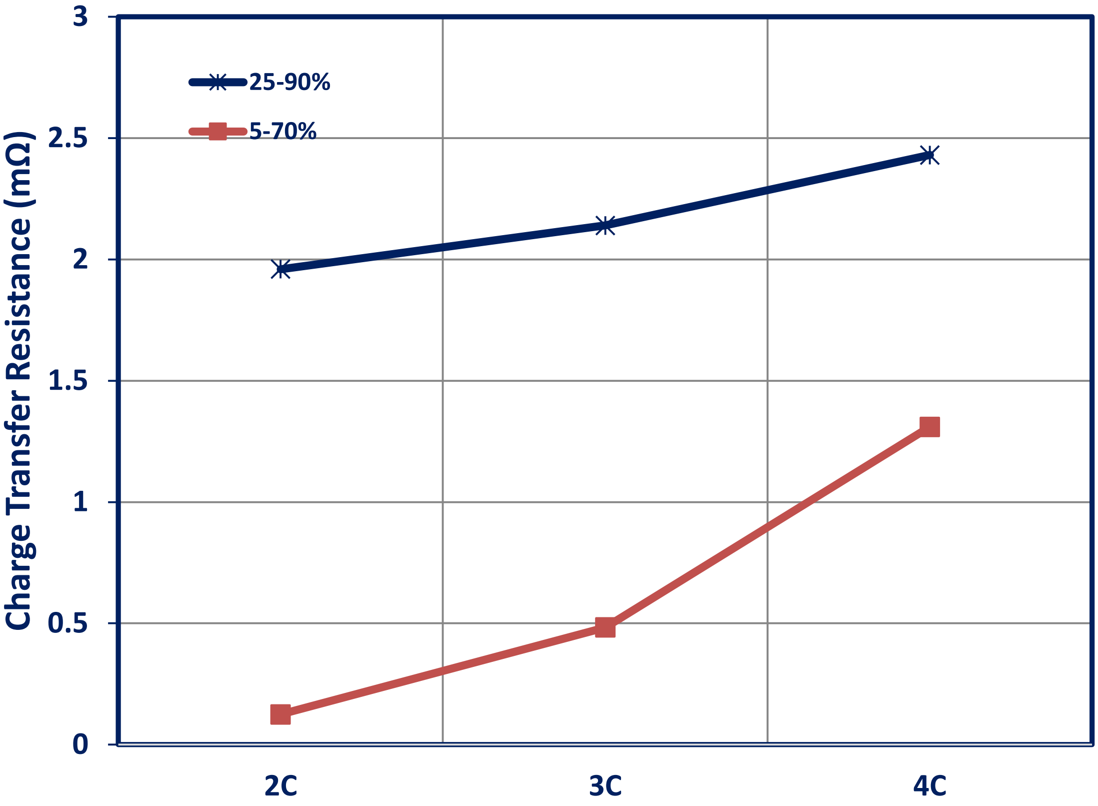

Figure 5.6: Comparison of the charge transfer resistance as a function for the charge rate for the 25-90% and 5-70% SOC range

## 5.2 Surface Layer Growth Characterization

The solvent reduction at the graphite electrode was the only electrode/electrolyte interaction in the cell. The oxidation side reaction on the cathode was considered negligible. This interaction accounted for the observed impedance and capacity fade in the batteries. Hence the charge consumed in the side reaction at the anode corresponds to the total capacity loss (irreversible and reversible capacity loss).

The side reaction on the anode/electrolyte interface produced reaction deposits on the surface of the electrode shown in Figures 5.7 and 5.8. The number of electrodes that had this deposit layer formed is as summarized in Table 5.1 was directly related to the potential and charge rate at which batteries were cycled. The constituents of the deposit layer were made up of chemical species such as: $Li_2CO_3$, $ROLiCO_3$, $Li_2O$, LiF and LiOH, same as those produced when the cell potential studies were carried out. For the cells cycled at 25-90% SOC, large agglomerates of deposits on the electrode were no different for 4C and 3C, while isolated agglomerate were seen on the surface as the charge rate was reduced to 2C (Fig. 5.7).

These results indicated that at high charge rate, which caused different parts of the electrode to have different voltage drop led to the continuous electrolyte reduction process that produced a deposit layer with variations in its thickness. In the case of the 5-70% SOC cycling at 4C, a comparable deposit agglomeration was observed as in the 25-90% for 3C and some isolated deposits whose thickness was about 12μm. For the cells cycled at 2C for the 5-70% SOC, the deposits were not obvious on the surface of the anode electrode at low magnification. At high magnification, the deposits on the carbon particles were thin and estimated to be between 1μm and 100nm (could not measure directly using the Annotation tool on the SEM). The thickness of these deposits layer for the different charge rate, as shown in Figures 5.9 and 5.10 (with the exception of 2C at the 5-70% SOC) at the two different SOCs are plotted in Figure 5.11.

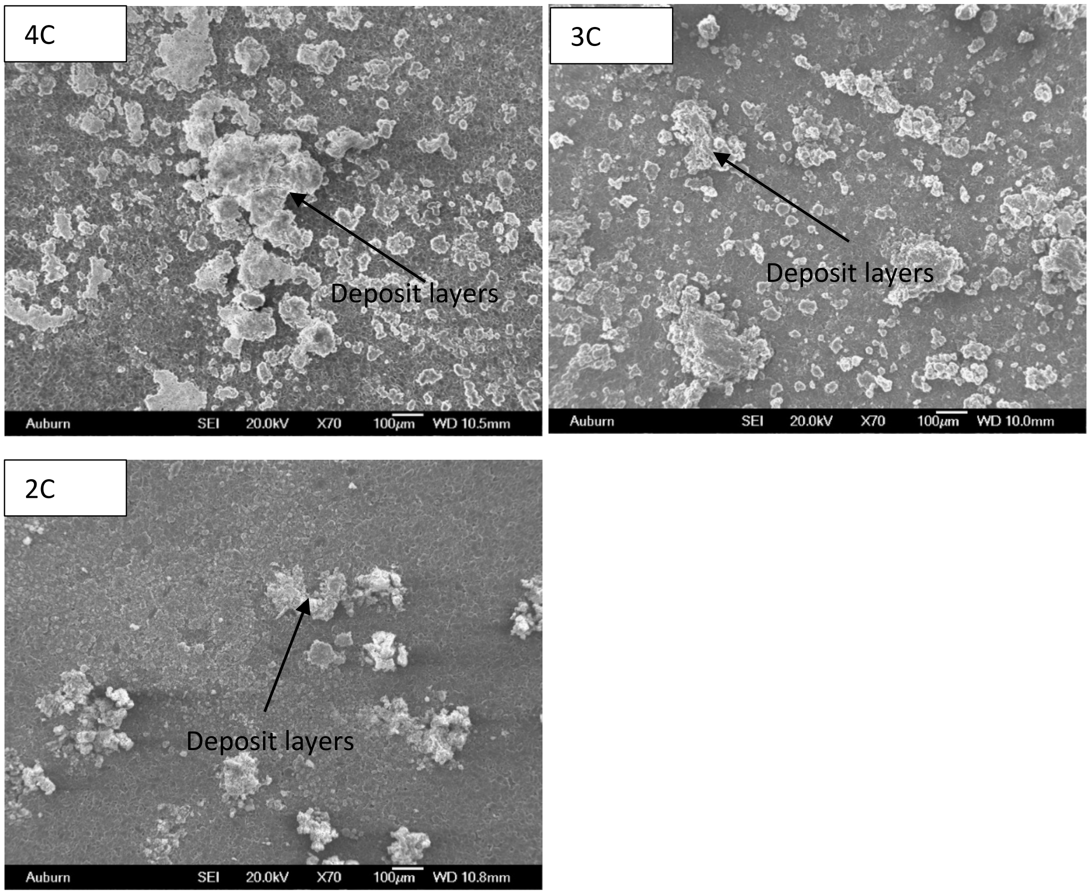

Figure 5.7: Surface distribution of deposit layer at different charge rate for cell aged at 25-90% SOC

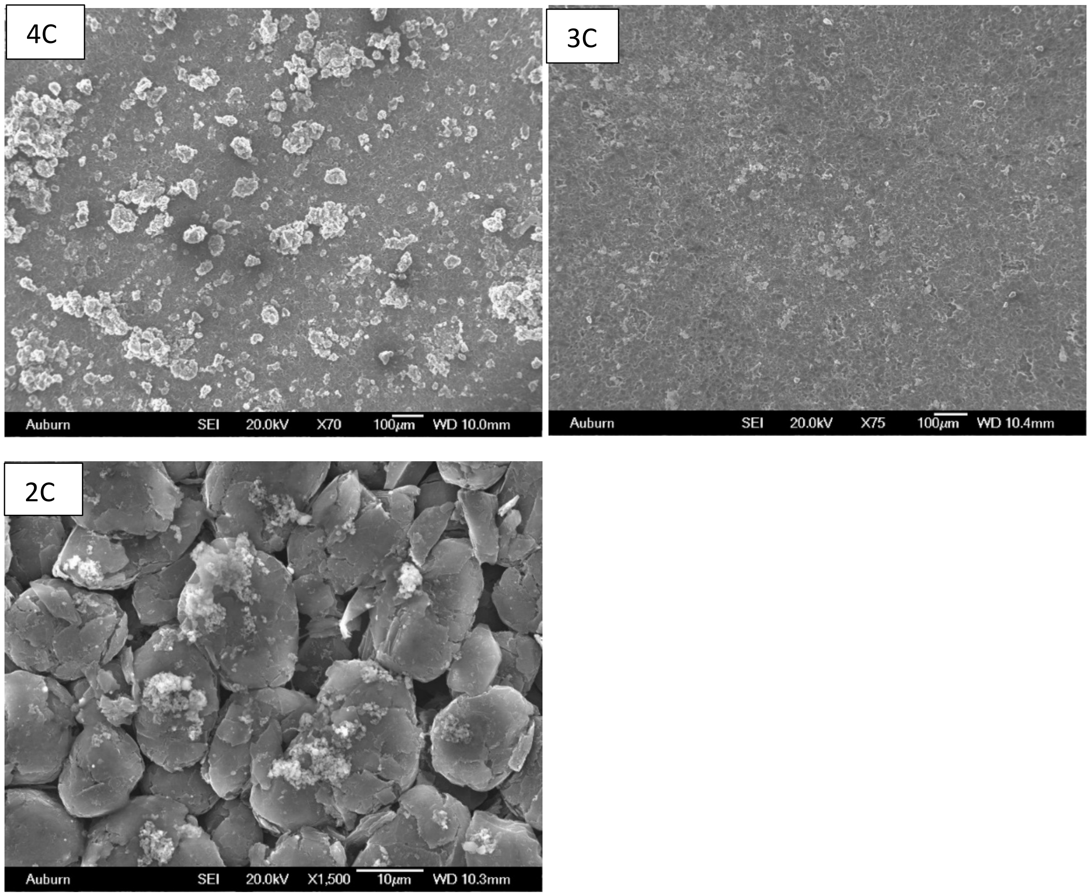

Figure 5.8: Distribution of the deposit layers on the electrode surface for the cell aged at 5-70% SOC at different charge rate.

Table 5.1: Summary of the number of electrodes affected for carbon loss/deposit layer out of a total of 17 anode electrodes in the battery pack.

| **Charge Current** | **Test Condition** | **Carbon Loss ( # electrodes affected)** | **Deposit layer ( # electrodes affected)** |
|---|---|---|---|
| 4C | 25-90% SOC | 14 | 17 |
| | 15-80% SOC | 8 | 17 |
| | 5-70% SOC | 6 | 8 |
| | 5-60% SOC | 3 | 2 |
| 3C | 25-90% SOC | 12 | 14 |
| | 5-70% SOC | 0 | 4 |
| 2C | 25-90% SOC | 8 | 6 |
| | 5-70% SOC | 0 | 0 |

In reducing the charge rate, there was a comparable reduction in the deposit thickness for the two different SOCs. These results also showed that cycling the cell at high SOC produced a considerable amount deposit thickness (37µm) even at low charge rate of 2C. While lowering the SOC (5-70%) and the charge rate to 2C produced a thinner deposit layer of less than 1µm thick. These deposits on the surface of the anode electrode acted as blocking agents to the porous anode electrode that contributed to the high interfacial resistance. The high charge transfer resistance along with the Ohmic and the SEI resistance that were observed (EIS results) for the two SOCs regimes, which increased as the charge rate was increased collaborated the growth of the deposit layer thickness. Thus the deposited layer on the carbon particles at the electrode/electrolyte interface caused significant increase the interfacial resistance.

The analysis of the interrelationship between the growth of the deposit layer, the resistance and the effect of charge rate (Fig. 5.12), showed a linear relationship between the deposit layer and the charge transfer resistance as a function of the charge rate. The SEI resistance, on the other, was significantly larger at high C-rate when the battery is charged at high SOC. Therefore, unlike the effect of state of charge discussed in section 4.0, where SEI resistance did not contribute significantly to the overall battery impedance with changing SOC, the SEI resistance does contribute considerably to the overall battery impedance only at the high SOC and charge rate.

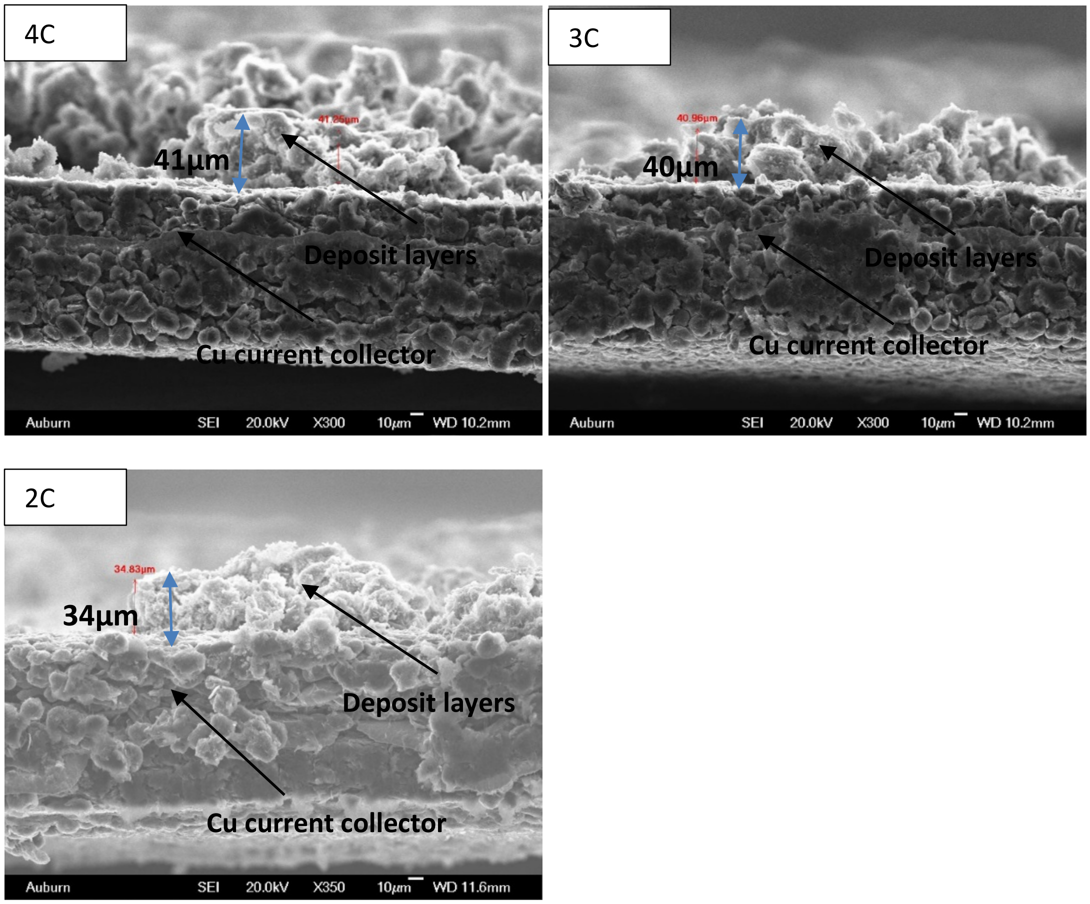

Figure 5.9: Cross sectional view of deposit layer on anode surface for different charge rate

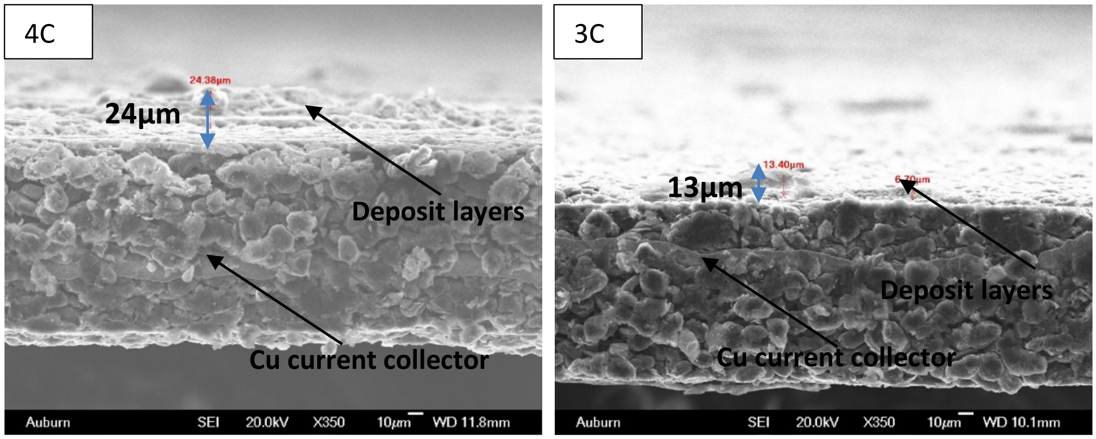

Figure 5.10: Cross sectional view of the deposit layer at different C-rate for the aged cell at 5-70% SOC

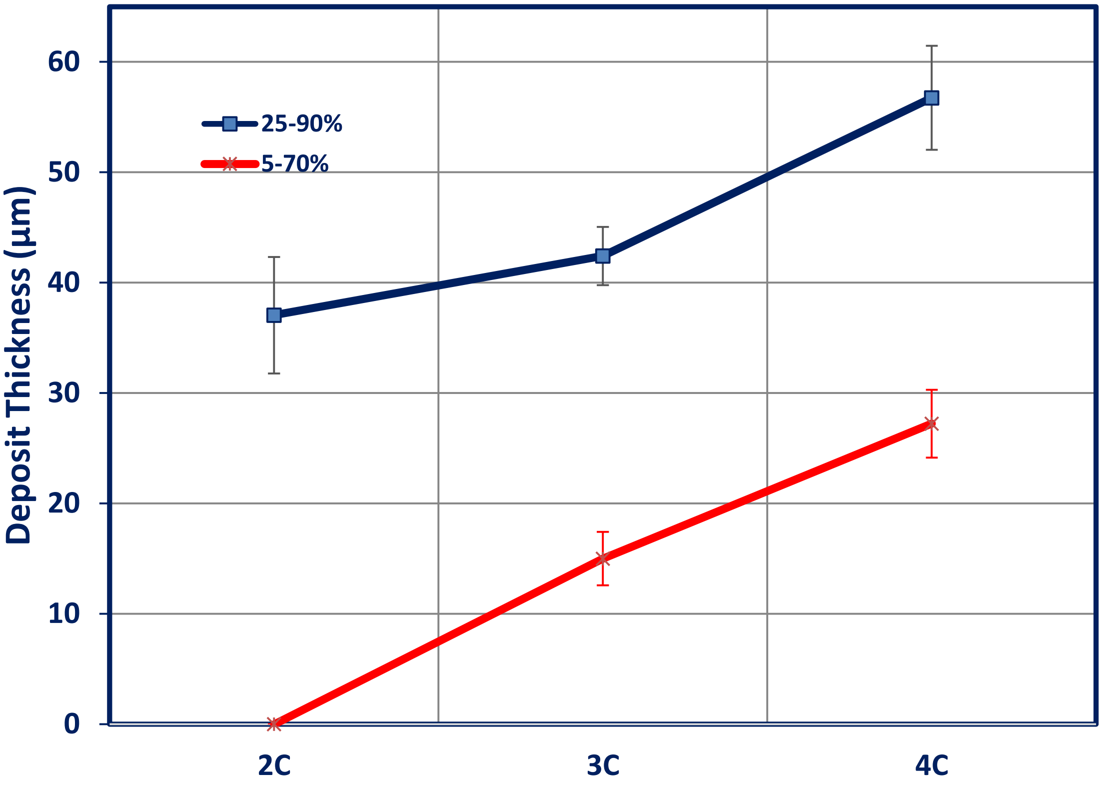

Figure 5.11: A comparison of deposit layer thickness at the different charge rate for the 25-90% SOC aged cell.

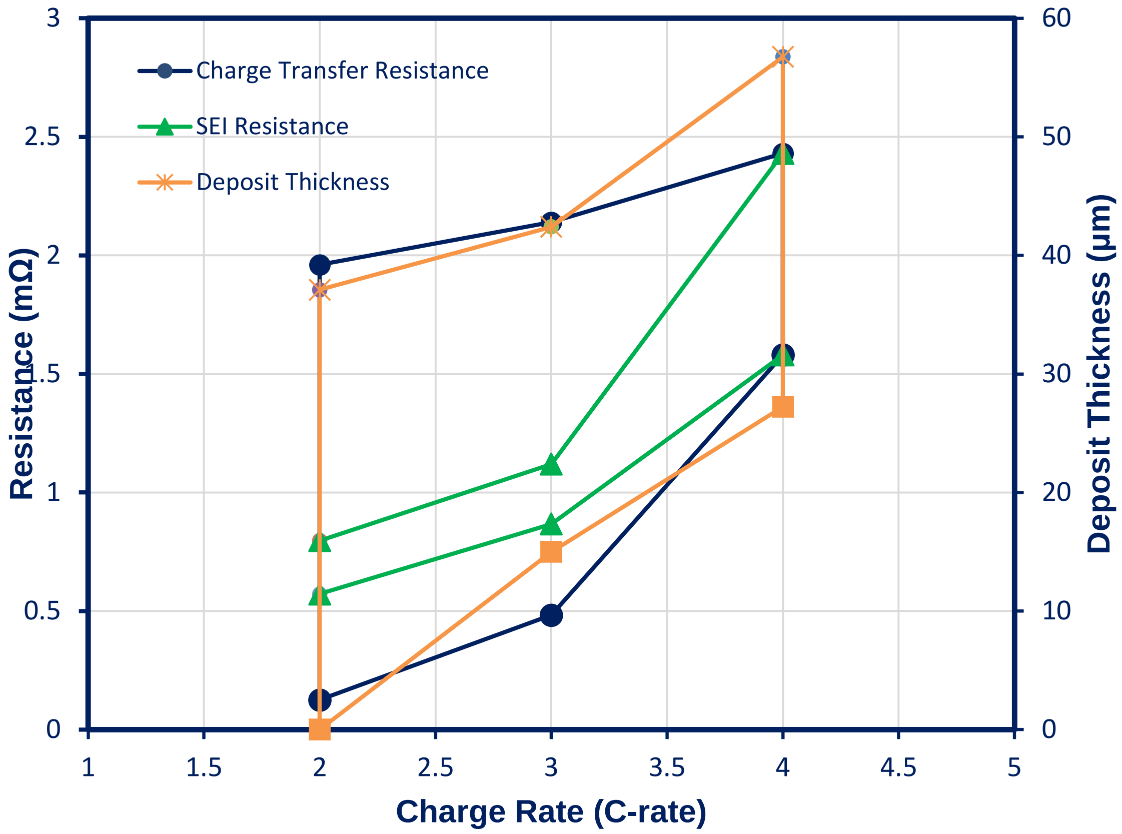

Figure 5.12: An analysis of the interrelationship between the charge rate, deposit layer growth, and the resistances in the battery

### 5.3 Loss of Carbon Particles on Electrode Surface

The rate at which the lithium ions were pushed into the crystal structure of the graphite electrode created some diffusion related stresses in the electrode. These stresses caused the expansion of the carbon particles during charging and a contraction at the discharge. These volume change measured using the LVDT is depicted in Figure 5.12 for the 25-90% SOC at 3C (rest of volume change data for the different SOCs and charge rates as shown in Appendix A). This volume change resulted in the loss of adhesion of the binding material between the particles and particle and the current collector. The loss of carbon adhesion was found to increase as the potential was increased as was reported in section 4.4.

In study of the effect of charge rate on the deposit layer formation for the two SOCs: 25-90% and 5-70%, it was observed that carbon loss decreased progressively as the charge rate was reduced. At 2C there was no loss in carbon particles adhesion (Fig 5.13), whereas there was a considerable thickness of the deposit (about 37μm) when the batteries were cycled at 25-90% SOC. While carbon loss was only observed at 4C when the cell is cycled at 5-70% SOC, cycling the batteries at 3C and 2C did not induce stress levels that could result in the loss of carbon adhesion in the electrode.

An analysis of the relationship between the loss of carbon particles and the trapped lithium in the graphite sheet (Fig. 5.19) showed a linear relation. The batteries that were cycled at 4C and 3C at 25-90% SOC loss a considerable amount of carbon particles. At 5.33% loss of carbon particles, a corresponding large amount of lithium was trapped in the graphite sheet compared to 3.3% loss at 4C for cells cycled at 4C at 5-70% SOC, where the lithium trapped did not significantly differ from those in the baseline graphite.

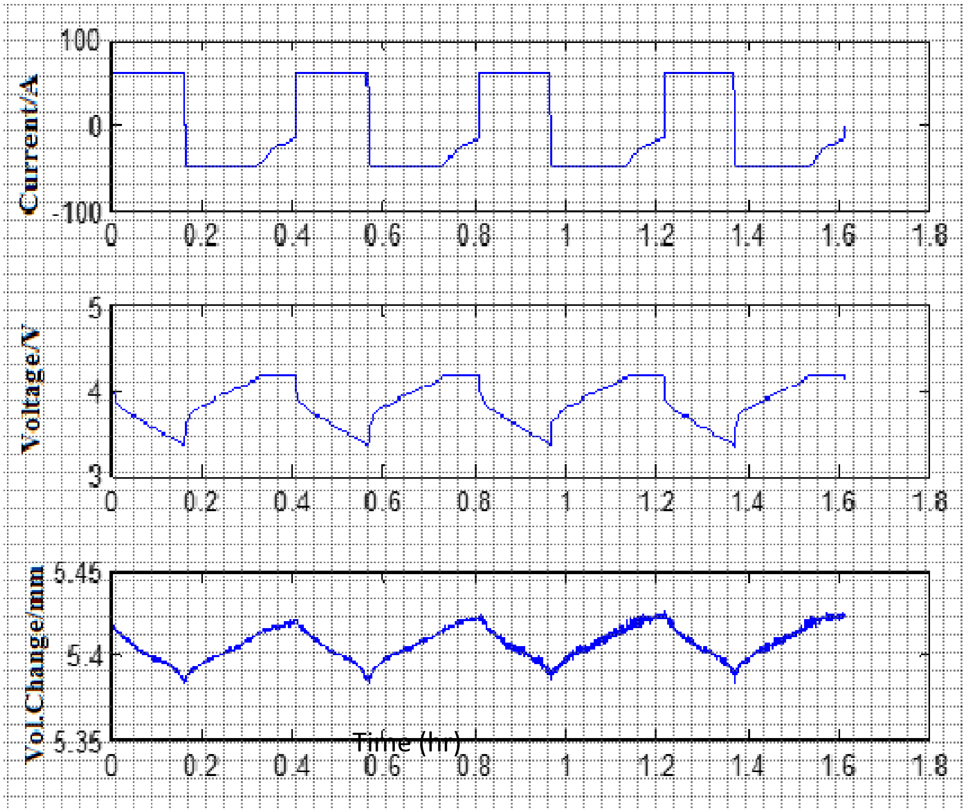

Figure 5.13: Voltage/ current profile with corresponding cell volume change during

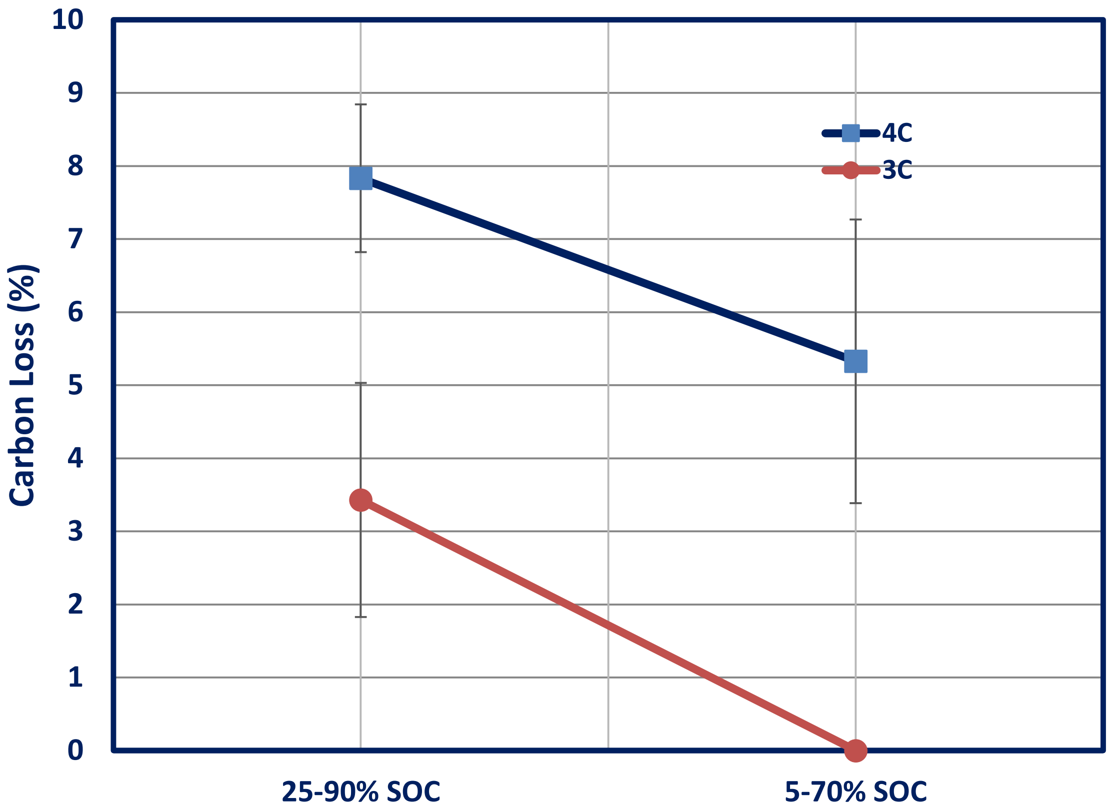

Figure 5. 14: Comparison of the carbon loss area as a function for the charge rate for the different SOC range

### 5.4 Characterization of the Loss Lithium Content

The X- ray diffraction for the aged anode had two new phases at $2\theta$ 64° and 78, in addition to those peaks patterns for the carbon and the copper current collector, similar to those observed in Figure 4.8 that was attributed to be those of LiF species from the deposit layer from the electrolyte decomposition products. To analyze the structural changes in the graphite electrode, the (002) peak (Fig 5.14/5.15) for the various charge rates for each of the states of charge (the rest of peaks are shown in Appendix B) were de-convoluted using the Lorenz function (peak fit software). As observed previously, the intercalation of lithium into the graphite structure tends to increase the d-spacing and shifted the (002) peak to lower $2\theta$ angles and the peak broadening was attributed to the presence of “trapped’ lithium in the graphene layers after the electrode was discharged to 2.5V (0% SOC).

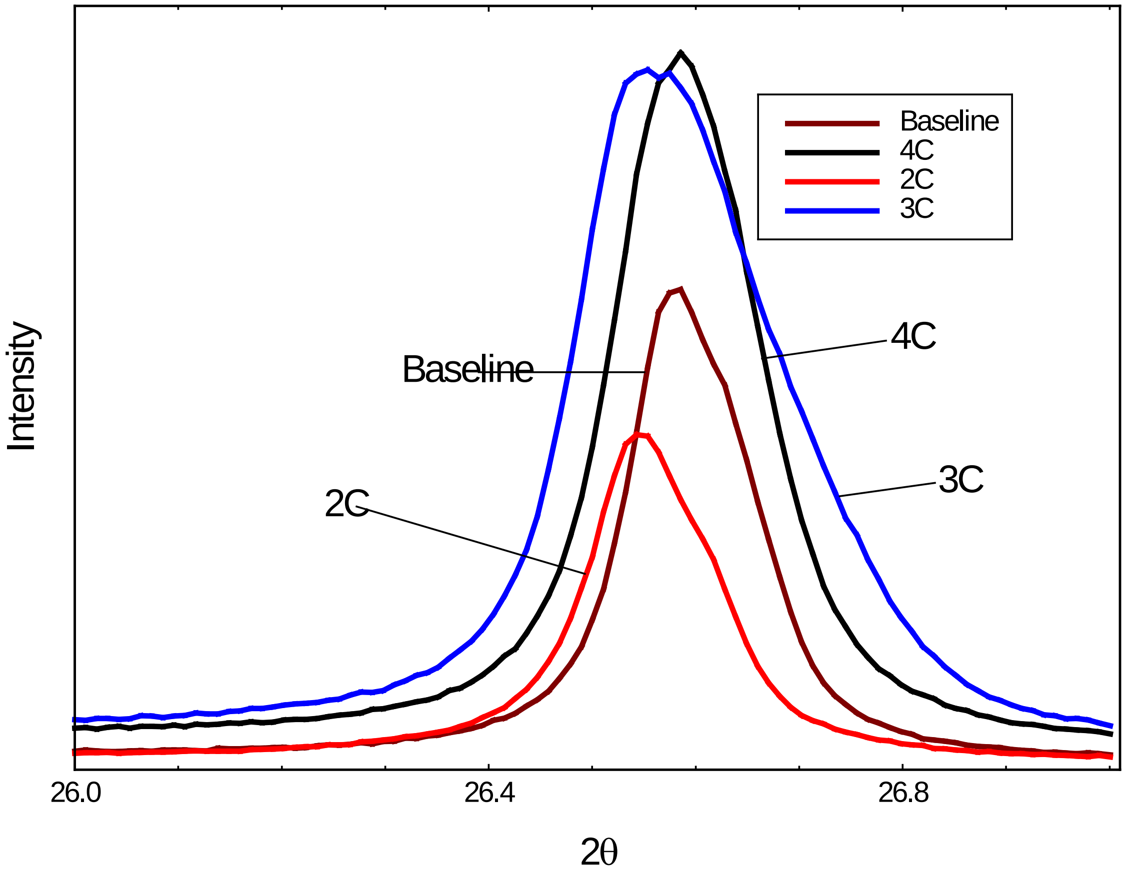

Figure 5.15: XRD spectra for the 002 peak for the 5-70% SOC at different charge rate

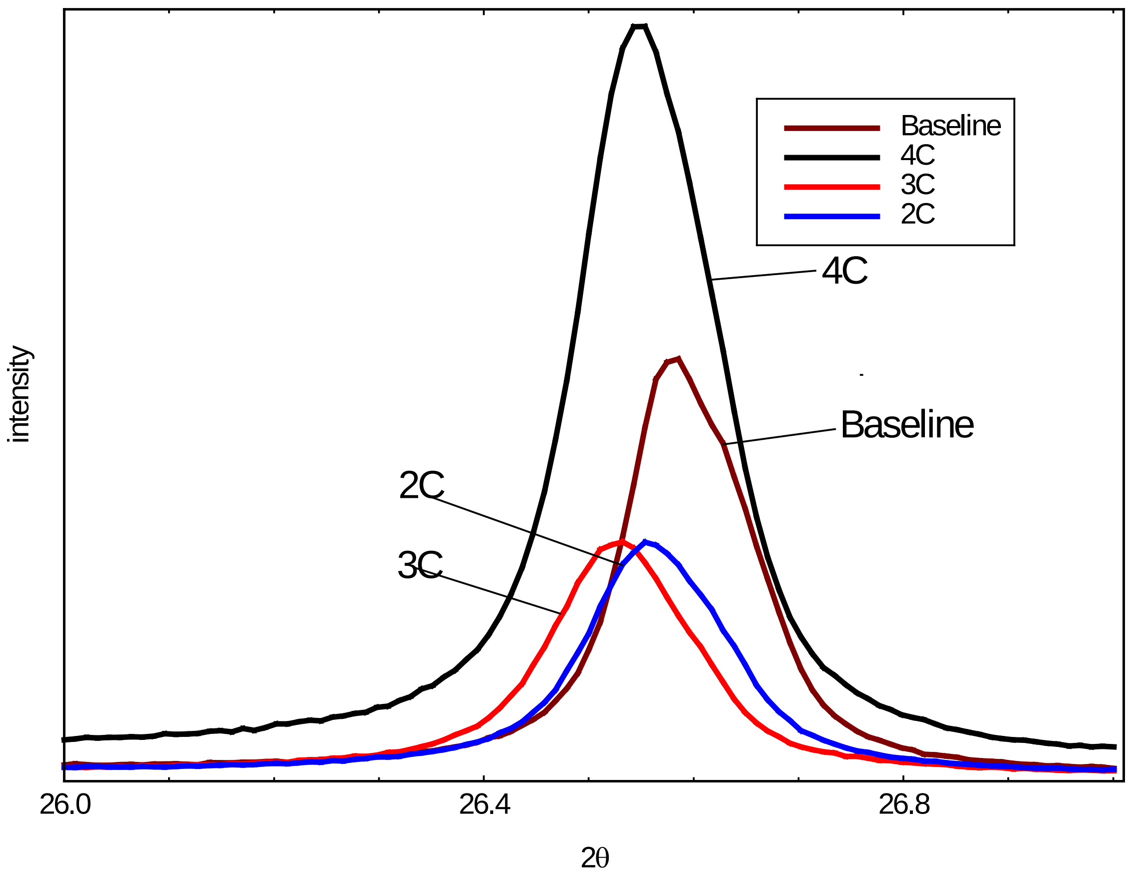

Figure 5.16: XRD spectra for the 002 peak for the 25-90% SOC at different charge rate

The de-convolution of the peaks for each of the states of charge showed the existence of a shoulder (Fig 5.16) and the peak broadening and the relative increase in intensity was attributed to the presence of two peaks within each peak. The d-spacing ($d_{002}$) and the corresponding lithium content for each de-convoluted peak within each test condition was determined from the lattice parameter calculation and plotted in Figures 5.17 and 5.18 respectively. The de-convoluted two peaks gave rise to a lower and upper $d_{002}$. The existence of the two d-spacing implied that some particles had higher lithium content than others in the graphite electrode matrix, hence the distribution of the lithium in the graphite was considered not uniform after the discharge process.

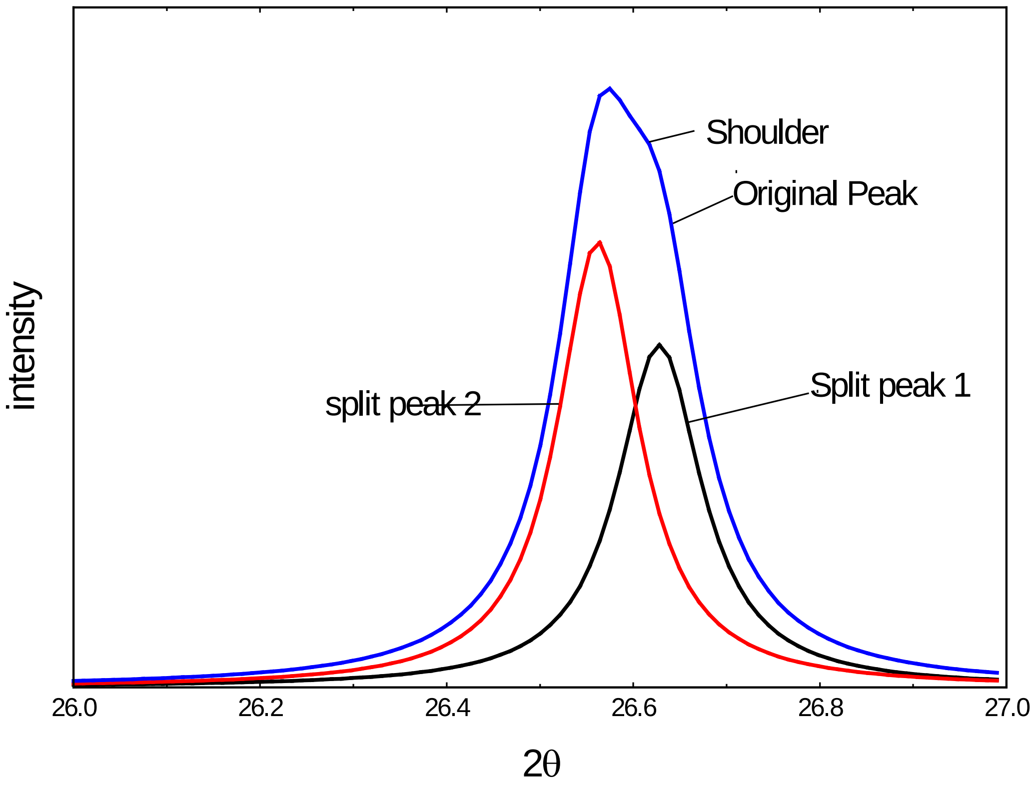

Figure 5. 17: XRD spectra for the de-convoluted peak for the (002) peak for the 25-90% SOC at 4C

The analysis of the $d_{002}$ for the high SOC (i.e. 25-90%) showed that the lower $d_{002}$ values were significantly above that of the upper $d_{002}$ for the baseline at an uncertainty of ±0.0014Å for batteries cycled at 3C and 4C charge rate. In addition, the upper $d_{002}$ values for batteries cycled at both high and low potentials at charge rate 3C and 4C were significantly higher compared to the upper $d_{002}$ for the baseline graphite electrode. On the other hand, for batteries cycled at low current (2C) charge rate; for the low potential, both the upper and lower $d_{002}$ values were statistically comparable to those of the baseline graphite electrode, while that for the high potential regime both the lower $d_{002}$ values and were significantly higher than the corresponding upper and lower $d_{002}$ values for the baseline.

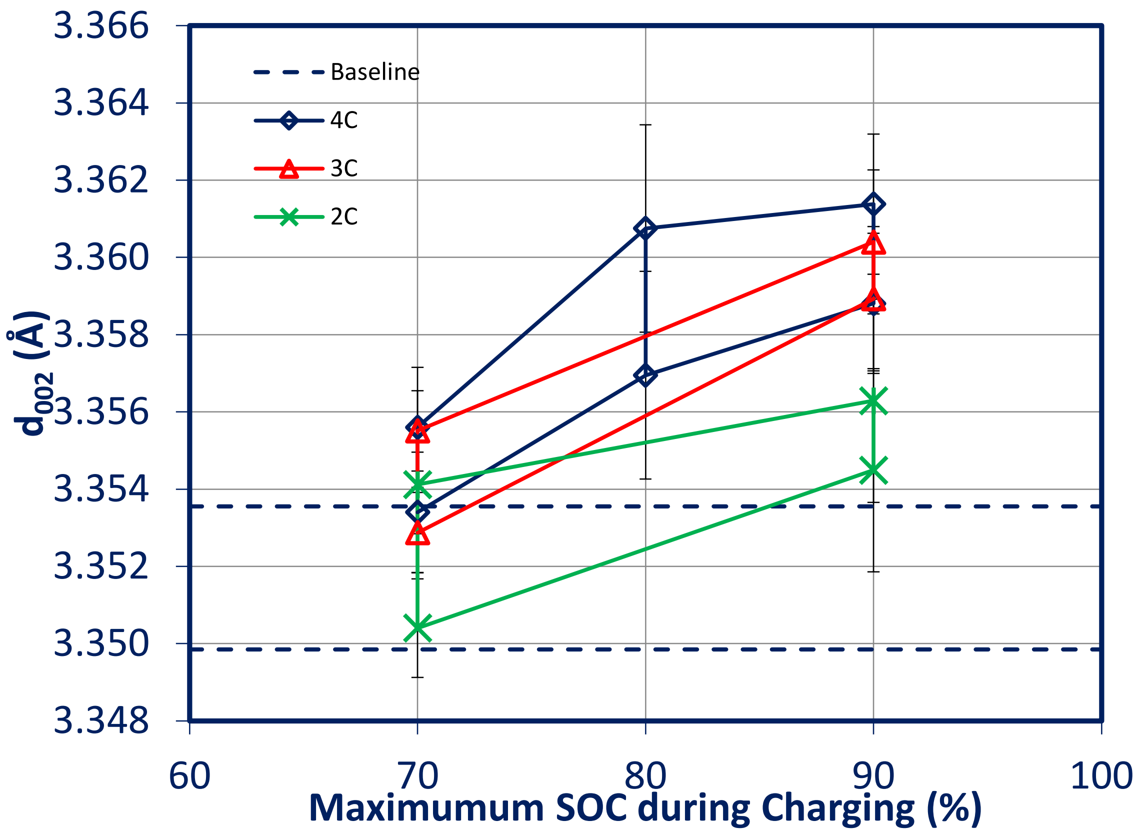

Figure 5.18: The d-spacing for the de-convoluted peaks as a function of SOC and charge rate.

The results from the d-spacing had direct bearing on the lithium content in the graphite structure after the cell discharge process as shown in Figure 5.18.

The amount of “trapped” lithium in the graphite layers after discharge were determined and tabulated in Table 5.2. The amount tends to increase for the high SOCs at 3C similar to that reported for the 4C. This similarity in the amount of lithium trapped in the graphite sheets for the high SOC for the 4C and 3C correlates with their capacity fade results ( i.e. 4C = 17.9% and 3C = 16.9% capacity fade). However, as the charge rate was reduced to 2C the of amount lithium trapped reduced considerably. This however, did not correlate with the loss in capacity at 2C, which was about 15.7%. This was attributed to two factors:(1) the formation of a thick deposit layer (37.1μm) and the associated resistance rise i.e. transfer and SEI resistance although the charge current was reduced, in addition to the considerable amount of lithium in the deposit. (2) A further analysis of the relationship between the carbon area and the trapped lithium content (Fig 5.19) in the graphite sheet gave an insight to the why the batteries had an increased in irreversible capacity in spite of a reduction of the charge rate. From the analysis in Fig 5.19, it was obvious that the lithium content trapped in the graphite was significantly higher than the baseline at 2C rate. This result is at variance with the earlier attribution of the trapped lithium as a result of the carbon loss due to electrical path discontinuity and isolation of the particles from the electrochemical process. At 2C rate, there was not loss of carbon particle adhesion, therefore a high lithium trapped in the graphite sheet could be due to the observed overpotential at high SOC as evident by the thick deposit layer.

| SOC | Charge rate | Weighted Average ( X in LixC6) | lithium Trapped(%) | |
|---|---|---|---|---|
| Baseline | - | 0.21685 | - | - |
| 5-70% | 3C | 0.23401 | 2.5 | |
| 25-90% | | 0.26905 | 7.6 | |
| 5-70% | 2C | 0.22595 | 1.3 | |
| 25-90% | | 0.23715 | 3.0 | |

In the case of the lower SOC, some particles had higher lithium content compared to the baseline (i.e. for the upper $d_{002}$), while in the some instances, especially the lower charge rate (2C), the lithium content was comparable to that existing in the baseline line structure. These results showed that for the lower SOC, cycling the batteries at lower charge resulted in most of the lithium content within the graphite reversed to the cathode during discharge. These findings correlated well with the capacity fade results for the 2C at 5-70%, where the battery loss about 0.5Ah (4.1%).

Table 5. 2: Weight average of Lithium in the graphite sheets and the percentage trapped from analysis of the 002 peak from XRD analysis

| SOC | Charge rate | Weighted Average ( X in $Li_xC_6$) | Lithium Trapped (%) | Peak Area |
|---|---|---|---|---|
| Baseline | - | 0.22 | - | 213 |
| 5-70% | 3C | 0.23 | 2.5 | 229 |
| 25-90% |  | 0.27 | 7.6 | 238 |
| 5-70% | 2C | 0.23 | 1.3 | 212 |
| 25-90% |  | 0.24 | 3.0 | 218 |

These trapped lithium ions were therefore isolated from the electrochemical process, which contributed to the high capacity fade of the batteries observed at high SOC. Therefore cycling the batteries at high SOC irrespective of the charge rate produced a significant surface deposit layer that contained a sizeable amount of lithium (XPS analysis), in addition to the trapped lithium within the graphite layers which did not get back to the cathode electrode during the discharge process.

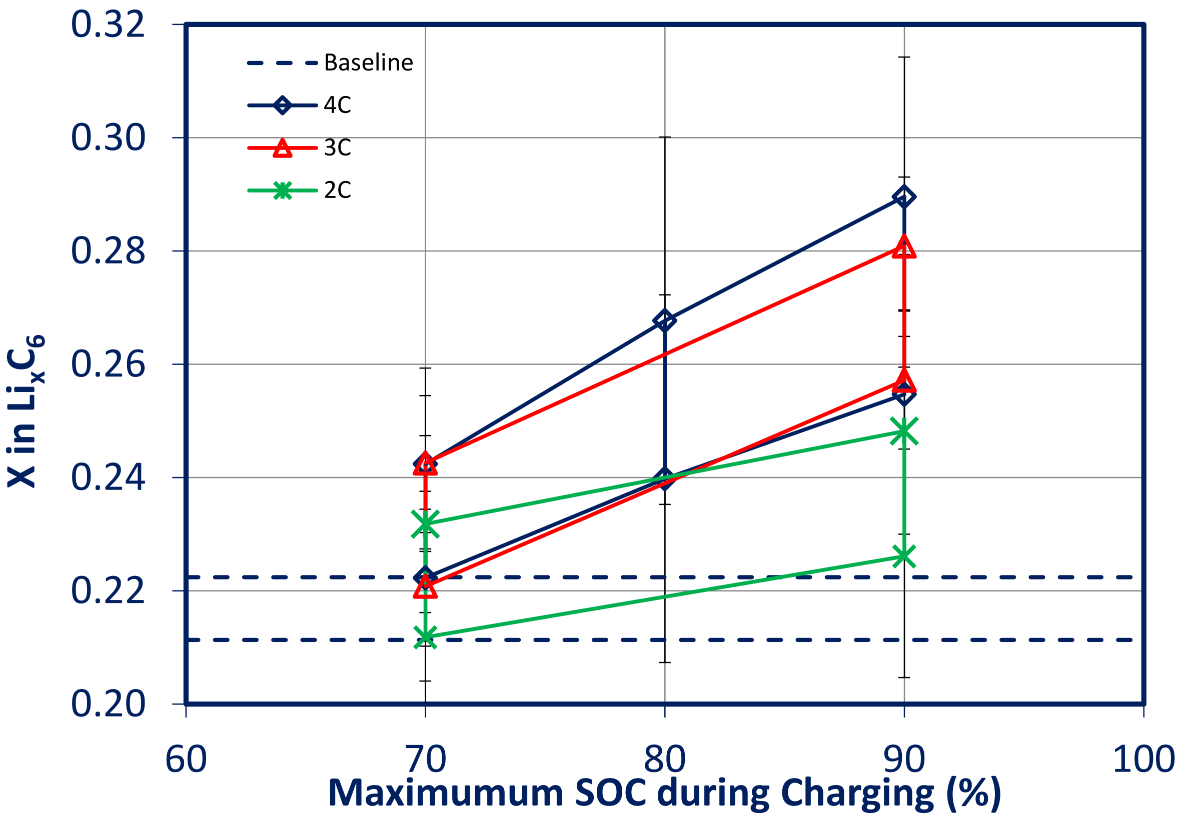

Figure 5. 19: Lithium content in the graphite layers as a function of SOC and charge rate

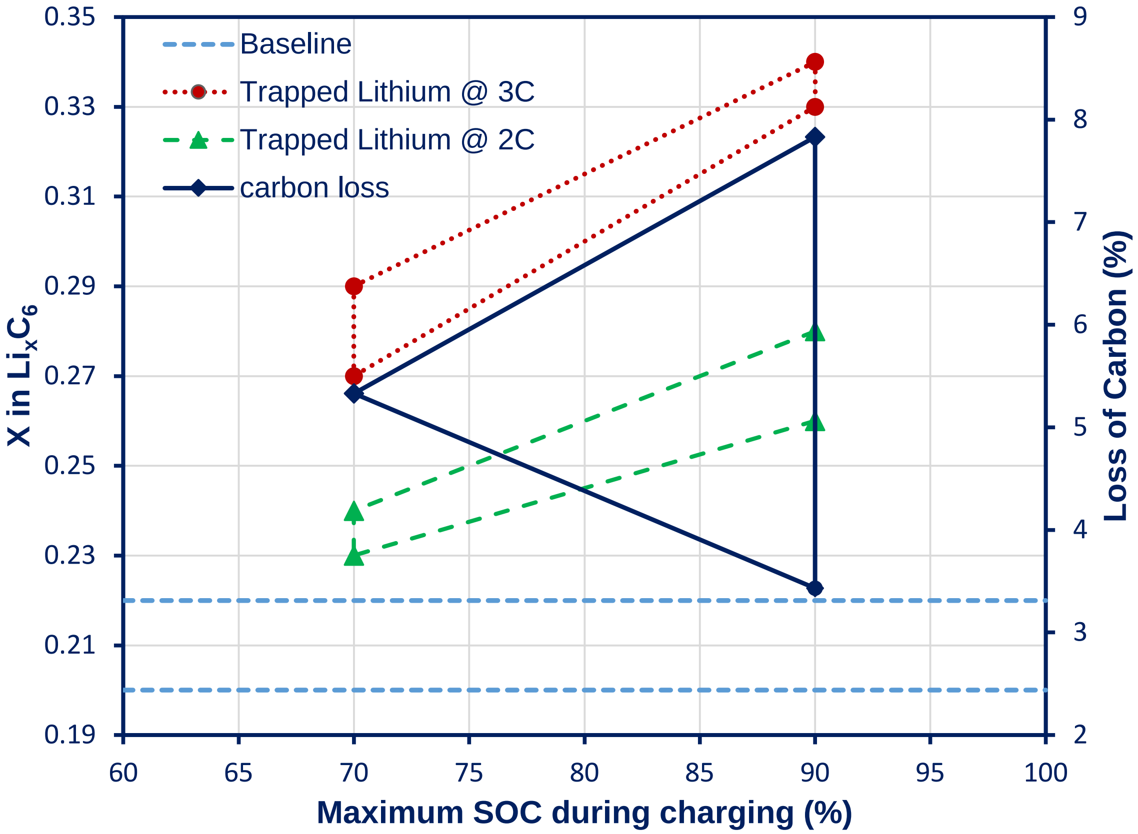

Figure 5. 20: A graph showing the relationship between the carbon at 4C/3C and the lithium content trapped in the graphite sheet after discharge

### 5.5 Summary of Findings

Low SOC (5-70% SOC)

- Cycling the cell at high charge rate (4C) increased significantly the irreversible capacity loss of the cell.
- At lower SOC of 5-70%, a low to moderate charge rate of 2C and 3C does not caused a significant capacity fade in the cell.
- At lower SOC, the deposit thickness was considerable thinner compared to the higher SOC as the charge rate is lowered, and record a less than 1µm at 2C
- The observed thin deposit layer was consistent with the low capacity fade.
- At low charge rate of 2C and 3C, there was less diffusion related stresses in the electrode matrix by a large gradient of lithium ion concentration at low potential thus no loss in carbon particles adhesion was recorded.
- At low SOC, cycling the batteries at lower charge resulted in most of the lithium content within the graphite reversed to the cathode during discharge.
- The low amount of lithium trapped in the graphite sheets was consistent with the capacity fade results for the 2C at 5-70%, where the battery loss about 0.5Ah (4.1%).

High SOC (25-90%)

- Varying the charge rate at high SOC does not significantly reduce the irreversible capacity of the battery.
- Higher SOC (25-90%) level significantly produce a thick deposit layer even when the charge rate is lowered.
- There was a considerable thickness of the deposit about 37µm when the batteries were cycled at 25-90% SOC at the same charge rate.
- The diffusion related stresses that caused the carbon loss decreased progressively as the charge rate was reduced.
- At higher SOC, regardless of the current rate, a substantial amount of lithium was trapped between the graphite sheets which did not get to the cathode electrode during the discharge process.

- The trapped lithium ions were isolated from the electrochemical process, which contributed to the high capacity fade recorded for the batteries at high potential.

# Chapter 6

## Conclusions

Increasing the battery cycling potential and charging rate was deleterious to the lithium ion battery, such a charging protocol depletes the recyclable lithium via trapping of lithium in the crystal structure of the graphite at the end of discharge and initiates the formation of deposit layer at the electrode/electrolyte interface that affected the lithium kinetics at the electrode/electrolyte interface. This layer contained a considerable amount of lithium that was consumed during its formation, which essentially reduces the amount of recyclable lithium involved in the electrochemical process. The high cycling potential coupled with high charge rate created a large lithium concentration gradient that leads to some particles detachment from the current collector and eventually isolated in the electrochemical process. However, only 8% of carbon particles were detached from the total surface area of the composite electrode matrix after 600 cycles for the highest SOC level (25-90%) and much lesser for the low potential range. This particle carbon area loss could significantly increase at prolong higher cycle numbers.

A correlation between the batteries capacity fade during cycling and the progressive growth of the deposit layer thickness, depletion of the recyclable lithium via trapping in the graphite sheets, and the loss of graphite active material was established.

The results showed that reducing the charge rate while cycling the batteries at high potential did not reduce the irreversible capacity loss of the lithium ion batteries. There was significantly thick deposit layer on the electrode surface even when the charge rate was reduced to 2C (i.e. about 32μm). The amount of lithium that was trapped in the graphite layers also did not differ as the charge rate was reduced. However, the diffusion induced carbon loss in the composite electrode matrix, decreased progressively as the charge rate was reduced due to the reduction in the lithium concentration gradient in the electrode during the intercalation/de-intercalation process.

A significant reduction in the irreversible capacity of the batteries was observed when the battery was cycled at low potential and reduced charge rate. The capacity of the batteries aged at low potential and medium charge rate (i.e. 3C and 2C) were comparable to the baseline after 600 cycles. This low degradation was attributed to less lithium trapped in the graphite sheet at the end of discharge - most of the lithium content within the graphite sheets were reversed to the cathode electrode and a thin deposit layer formed at the electrode/electrolyte interface as the charge rate was lowered.

From these results, it is therefore concluded that cycling batteries at low to moderate state of charge and a low to moderate charge rate of 2C and 3C will prolong battery capacity retention. This charging protocol produced less battery injurious degradation mechanism thus produced a high batteries capacity retention compared to cycling at high potential.

# Chapter 7

## Recommendation for Future works

To further enhance the understanding of the potential on the formation of the deposit layer resulting from the electrolyte side reaction, an in situ study would offer an insight in the mechanism and the critical battery potential at which the decomposition reaction is initiated. During the insertion/de-insertion of lithium into the cathode/anode requires that the redox potential of the cathode and that of the anode lie within energy gap of the electrolyte to maintain a thermodynamic stability in order to avoid unwanted reduction or oxidation of the electrolyte. The suggested further research will be aimed at answering the scientific question whether cycling the battery at high potential puts the battery out of this window that resulted in the excessive deposition of the deposit layer? To achieve this, the changes the polarization potential in each electrode during charging/discharging should be investigated using an electrochemical thermodynamic measurement system (eg. ETMS-1000). To carry out this, most of the electrochemical thermodynamic measurement systems use smaller battery making the large format pouch battery lithium ion battery not suitable. Therefore a coin cell with the pouch cell chemistry should be designed for this purpose.

An effective SEI layer prevents the occurrence of further electrolyte reduction on the carbon electrode. High battery potential led to the formation of a thick deposit layer (i.e. 52μm). The second scientific question arising from the study will be to investigate whether cycling batteries at high potential breaks down the SEI layer leading to the increase in electrolyte decomposition reaction. A quantitative analysis of the growth of the SEI layer could therefore be carried out. The challenge in studying the SEI on the anode electrode using the TEM has always been the samples preparation; we proposed two methods of sample preparation to overcome this challenge: use of focused ion beam and the ion milling.

## Bibliography

[1]. M.S Whittingham, "Material challenges facing electrical energy storage," *MRS Bull* Vol. 33(4), pp.411-419, 2008.

[2]. A. Patil, V. Patil, W.D. Shin, J. W.Choi , D. S. Paik, and J. Yoon, "Issues and challenges facing rechargeable thin film lithium batteries," Mater. Res. Bull, vol. 43, pp. 1913-1942.2008.

[3]. A.K. Shukla, T.P. Kumar, "Materials for the next generation lithium ion batteries," *Curr. Sci.* vol.94, pp.314-331, 2008.

[4]. J.Shim, R. Kostecki, T. Richardson, X. Song, and K. A Striebel, "Electrochemical analysis for cycle performance and capacity fading of a lithium-ion battery cycled at elevated temperature," *J. Power Sources*, vol.112, pp. 222-230, 2002.

[5]. R. Kostecki, J. Lei, F. McLarnon, J. Shim, and K. Striebel, "Diagnostic evaluation of detrimental phenomena in high-power lithium-ion batteries," *J. Electrochem. Soc*. Vol.153, pp. A669, 2006.

[6]. M. Safari, and C. Delacourt, "Aging of a commercial graphite $LiFePO_4$ cell," *J. Electrochem. Soc.* Vol. 158, pp. A1123, 2011.

[7]. J.P. Fellner, G.J. Loeber, and S.S. Sandhu, "Testing of lithium-ion 18650 cells and characterizing/predicting cell performance," *J. Power Sources*, vol. 81, pp. 867- 871, 1999.

[8]. M.C. Smart, B.V.Ratnakumar, S. Surapudi, Y. Wang, X. Zhang, and S.G.Greenbaum, A. Hightower, C.C. Ahn, B. Fultz, "Irreversible capacities of graphite in low temperature electrolytes for lithium-ion batteries," *J. Electrochem. Soc*., vol.46,pp. 3963-3969, 1999.

[9]. P.L.Moss, G. Au, E.J. Plichta, and P. J. Zheng, "Study of capacity fade of lithium-ion polymer rechargeable batteries with continuous cycling," *J. Electrochem. Soc*., vol. 157(1) , pp. A1, 2010.

[10]. G. Sarre, P. Balanchard, and M. Broussely, "Aging of lithium-ion batteries," *J. Power Sources,* vol. 127, pp.65-712, 2004.

[11]. N.N. Sinha, A.J. Smith, J.C. Burns, J.Gaurav, K.W. Eberman, E. Scott, J.P. Gardner, and J.R. Dahn, "The use of elevated temperature storage experiments to learn about parasitic reaction in wound $LiCoO_2$/graphite cells," *J. Electrochem. Soc.*, vol.158, pp. A1194, 2011.

[12]. D.P. Abraham, J.L.Knuth, D.W.Dees, and I. Bloom, "Performance degradation of high power lithium ion cells- electrochemistry of harvested electrodes," *J. Power Sources*, vol. pp.170, 465–475, 2007.

[13]. M. Dolle, L. Sannier, B. Beaudion, and M. Trentin, "Live scanning electron microscope observation of dendrite growth in lithium polymer cells," *J. Electrochem. Soc*. vol. pp. 5, 286–289, 2002.

[14]. F. Ornini, D.A. Pasquier, B Beaudion, J.M. Tarason, and M. Trentin, "In situ scanning electron microscope observation of interfaces within plastic lithium batteries," *J. Power Sources,* vol.76,pp. 19–29, 1998.

[15]. R.A. Leising, M.J. Palazzo, E.S. Takeuchi, and K.J. Takeuchi, "A study of the overcharge reaction of lithium-ion batteries," *J. Power Sources*, vol. 97, pp. 681–683, 2001.

[16]. M. E. Spahr, H. Wilhelm, F. Joho, J.C Panitz, J. Wambach, P. Novak, and N. Dupont-Pavlovsky, "Purely Hexagonal Graphite and the Influence of Surface Modifications on Its Electrochemical Lithium Insertion Properties," *J. Electrochem. Soc. vol.* 149, pp A960-966, 2002.

[17]. N.Takami, A.Satoh, M. Hara, and T. Ohsaki, "Structural and kinetic characterization of Lithium intercalation into carbon anodes for secondary lithium batteries," *J. Electrochem. Soc*. vol. 142, pp. A371, 1995.

[18]. A.Funabiki, M. Inaba, Z. Ogumi, S. Yuasa, J. Otsuji, and A. Tasaka, "Impedance Study on the electrochemical lithium intercalation into natural graphite powder," *J. Electrochem. Soc.* Vol. 145pp. A 172, 1998.

[19]. L.Liu, and M. N. Obrovac, "Structural changes in LiAlSi during electrochemical cycling batteries and energy storage," *J. Electrochem. Lett.* vol.1(1), pp. A10, 2012.

[20]. K. Sato, M. Noguchi, A. Demachi, N. Oki, and M. Endo, "A mechanism of lithium storage in disordered carbons," Science, vol. 264, pp. 556-558

[21]. K.Tokumitsu, H. Fujimoto, A. Mabuchi, and T. Kasuh, "Structural characterization and electrochemical properties of non-graphitizable carbons for a lithium ion battery," *J. Power Sources*, vol. 90, pp. 206-213, 2000.

[22]. K.Tokumitsu, H. Fujimoto, A. Mabuchi, and T. Kasuh, "High capacity carbon anode for Li-ion battery, a theoretical explanation," *Carbon*, vol. 37, pp. 1599-1605,1999.

[23]. X. Wu, H. Li, L. Chen, and X. Huang, "Agglomeration and the surface passivating film of Ag nano-brush electrode in lithium batteries," *Solid State Ionics*, vol. 149 pp. 185– 192, 2002.

[24]. G.V. Zhuang, P.N. Ross, H.Yang, K. Xu, and T. R Jow, "Lithium methyl carbonate as a reaction product of metallic lithium and dimethyl Carbonate," *J. Electrochem. Solid-state Lett*. Vol. 9(2) pp. A64, 2006.

[25]. J.S Bridel, S.Grugeon, S. Laruelle, J. Hassoun, P. Reale, B. Scrosati, and J.M Tarascon,"Decomposition of ethylene carbonate on electrodeposited metal thin film Anode," *J. Power Sources,* vol. 195, pp. 2036–2043, 2010.

[26]. A.Wursig, H. Buqa, M. Holzapfel, F. Krumeich, and P. Novaka, "Film formation at positive electrodes in lithium-Ion batteries," *J. Electrochem. Solid-State Lett*, vol.8 (1), pp. A34, 2005.

[27]. N. Kircheva, S.Genies, D. Brun-Buisson, and P.X Thievel, "Study of solid electrolyte interface formation and lithium intercalation in Li-Ion batteries by acoustic emission," *J. Electrochem. Soc.*,vol. 159(1), pp.)A18, 2012.

[28]. K. Kanamura, S. Shiraishi, H. Takezawa, and Z.Takehara, "XPS Analysis of the surface of a carbon electrode intercalated by lithium Ions," *Chem. Mater*.vol. 9, pp. 1797-1804, 1997.

[29]. X. Wu, H. Li, L. Chen, and X. Huang, "Agglomeration and the surface passivation film of Ag nano-brush," *Solid State Ionics*, vol.149 pp. 185– 192, 2002.

[30]. Li, H. Li, Z. Wang, L. Chen, and X. Huang, "The study of surface films formed on SnO anode in lithium rechargeable batteries by FTIR Spectroscopy," *J. Power sources*, vol.107, pp. 1-4, 2002

[31]. R. Dedryvère, H. Martinez, S. Leroy, D. Lemordant, F. Bonhomme, P. Biensan, and D.Gonbeau, "Surface film formation on a carbonaceous electrode: Influence of the binder chemistry," *J. Power Sources*, vol. 174 pp. 462–468, 2007.

[32]. K. Takei, K. Kumai Y. Kobayashi, H. Miyashiro, T. Iwahori, T. Uwai, and H. Ue, "An X-ray photoelectron spectroscopy study on the surface film," *J. Power Sources,* 54 vol. pp. 171-174, 1995.

[33]. K. Kumai, H. Miyashiro, Y. Kobayashi, K. Takei, and R. Ishikawa, “Gas generation mechanism due to electrolyte decomposition in commercial lithium-ion cell,” *J. Power Sources*, vol. 81,pp. 715–719, 1999.

[34]. E.L Littauer, and K.C Tsai, “Anodic behavior of lithium in aqueous electrolytes: mechanical passivation,” *J. Electrochem. Soc*., vol. 123(7), pp. A964,1976.

[35]. M. Holzapfel, F. Alloin, and R. Yazami, “Calorimetric investigation of the reactivity of the passivation film on lithiated graphite at elevated temperatures,” *Electrochimica Acta,* vol. 49, pp. 581–589, 2004.

[36]. J.O. Besenhard, M. Winter, J.Yang, and W. Biberacher, “Filming mechanism of lithium-carbon anodes in organic and inorganic electrolytes,” *J. Power Sources,* vol. 54 pp. 228-231, 1995.

[37]. B. Ravdel, K.M. Abraham, R. Gitzendanner, J. DiCarlo, B. Lucht, and C. Campion, “Thermal stability of lithium-ion battery electrolytes,” *J. Power Sources,* vol 119, pp. 805–810, 2003.

[38]. D. Aurbach, M. Moshkovich, Y. Cohen, and A. Schechter, “The study of surface film formation on noble-metal electrodes in alkyl carbonates/Li salt solutions, using simultaneous in situ AFM, EQCM, FTIR, and EIS”, *Langmuir,* vol.15, pp. 2947-2960, 2010.

[39]. S.K Jeong, M. Inaba, R. Mogi, Y. Iriyama, A.Takeshi, and Z. Ogumi, “Surface film formation on a graphite negative electrode in lithium-ion batteries: Atomic Force Microscopy study,” *Langmuir,* vol.17, pp.8281-8286, 2001.

[40]. M. R. Wagner, P. R. Raimann, A. Trifonova, K.-C. Moeller, J. O. Besenhard, and M. Winter, “electrolyte decomposition reactions on Tin- and graphite-based anodes,” *Electrochem. Solid-State Lett.* vol. 7 (7), pp.A201, 2004.

[41]. S.K Jeong, M. Inaba, Y. Iriyama, T. Abe, and Z. Ogumi, “AFM study of surface film formation on a composite graphite electrode,” *J. Power Sources*, vol.119, pp.555–560, 2003.

[42]. S.B Lee, and S. Pyun, “The effect of electrolyte temperature on the passivity of solid electrolyte interphase formed on a graphite electrode,” *Carbon,* vol. 40, pp. 2333-2339, 2002.

[43]. G.V Zhuang, K. Xu, T.R Jow, and P.N Ross, “Analysis of the chemical composition of the passive film on Li-Ion battery anodes using attentuated total reflection,” *J. Electrochem. Solid State lett.*, vol.7(8) ,pp. A224,2004.

[44]. D. Rahner, “The role of anions, solvent molecules and solvated electrons in layer formation processes on anode materials for rechargeable lithium batteries,” *J. Power Sources*, vol. 81 pp. 358–361, 1999.

[45]. L. E Ouatani, R. Dedryvère, J.-B. Ledeuil, C. Siret, P. Biensan, J. Desbrières, and D. Gonbeau, “Surface film formation on a carbonaceous electrode: Influence of the binder chemistry,” *J. Power Sources*, vol. 189 pp.72–80, 2009.

[46]. S. Shiraishi, K. Kanamura, and Z. Takehara, “Study of the Surface Composition of Highly Smooth Lithium Deposited in Various Carbonate Electrolytes,” *Langmuir*, vol. 13pp. 3542-3549,1997.

[47]. Y. Domi, M. Ochida, S. Tsubouchi, H. Nakagawa, T. Yamanaka, T. Doi,T. Abe, and Z. Ogumi, “Surface Film Formation on the Edge Plane of HOPG for Lithium-Ion Batteries,” *J. Phys. Chem. C.*, vol. 115, pp.25484–25489, 2011.

[48]. H. Wang, Y. Jang, B. Huang, R.D. Sadoway, and Y.M Chiang, “TEM study of electrochemical cycling-induced damage and disorder in $LiCoO_2$ cathodes for rechargeable lithium batteries,” *J. Electrochem. Soc.*, vol.146, pp.A473-480, 1999

[49]. E.Yair, “The correlation between the cycling efficiency, surface chemistry and morphology of Li electrodes in electrolyte solutions based,” *Electrochem. Solid-State Lett.*, vol. 2 (5), pp 212-214, 1999.

[50]. G.V. Zhuang, and P. N. Ross, “Analysis of the chemical composition of the passive film on Li-Ion battery anodes using attentuated total reflection,” *Electrochem. Solid-State Lett.*, vol. 6 (7), pp. A136, 2003.

[51]. E.L Littauer, and K.C Tsai, “Anodic behavior of lithium in aqueous electrolytes: mechanical passivation,” *J. Electrochem. Soc.*, vol. 123(7), pp. A964,1976.

[52]. K. Takei, K. Kumai, Y. Kobayashi, H. Miyashiro, T. Iwahori, T. Uwai, and H. Ue, “An X-ray photoelectron spectroscopy study on the surface film on carbon black anode in lithium secondary cells,” *J. Power Sources*, vol. 54 pp. 171-174, 1995.

[53]. M. Dolle, S. Grugeon, B. Beaudion, L. Dupont, and J-M. Tarascon, “In situ TEM study of the interface of the carbon/electrolyte,” *J. Power sources*, vol. 97, pp. 104-106, 2001.

[54]. C.A. Caldas, M.C. Lopes, and I.A. Carlos, “The role of FeS and $(NH_4)_2$ $CO_3$ additives on the pressed type Fe electrode,” *J. Power Sources*, vol. 74 pp.108–112, 1998

[55]. M. Ota, S. Izuo, K. Nishikawa, Y. Fukunak, E. Kusaka, R. Ishii, and J.R. Selman, “Measurement of concentration boundary layer thickness development during lithium electrodeposition onto a lithium metal cathode in propylene carbonate,” *J. Electroanalytical Chem*.,vol. 559 pp. 175-183, 2003.

[56]. M.B Pinson, and M. Z. Bazant, “Theory of SEI formation in rechargeable batteries: capacity fade, accelerated and lifetime prediction,” *J. Electrochem. Soc*., vol. 160(2), pp.A243,2013.

[57]. Y. Domi, M. Ochida, S. Tsubouchi, H. Nakagawa, T. Yamanaka, T. Doi,T. Abe, and Z.Ogumi, “In Situ AFM Study of Surface Film Formation on the Edge Plane HOPG for Lithium-Ion Batteries,” *J. Phys. Chem. C*., vol.115, pp. 25484–25489, 2011.

[58]. D. Zane, A. Antonini, and M. Pasquali, “A morphology study of SEI film on graphite electrode,” *J. Power source*, vol. 97, pp.146-150, 2001.

[59]. A.Z. Shekhtman, “Peculiarities of lithium-cation kinetics through passivation the surface of lithium electrodes,” *J. Power Sources*, vol.54, pp. 433-434, 1995.

[60]. A.M. Andersson, M. Herstedt, A.G. Bishop, and K. Edstrom, “The influence of Lithium salt on the interfacial reactions controlling the thermal stability of graphite anodes,” *Electrochimica Acta*, vol. 47 pp.1885-1898,2002.

[61]. W.S Song, G.V Zhuang, and P.N Ross, “Surface film formation on $LiNi_{0.8}Co_{0.15}Al_{0.05}O_2$ cathodes using ATR-IR spectroscopy,” *J. Electrochem. Soc.*, vol.151(8), pp.A1162, 2004.

[62]. B. Fleutot , H. Martinez, B. Pecquenard, J.B. Ledeuil, A. Levasseur, and D. Gonbeau, “Surface film morphology (AFM) and chemical features (XPS) of cycled $V_2O_5$ thin films in lithium micro-batteries,” *J. Power Sources*, vol.180, pp. 836–844, 2008.

[63]. D. Rahner, S. Machill, and K. Siury, “Passivity of lithium in organic solvents”, *J. Power Sources*, vol. 68 pp. 69-74, 1997.

[64]. C.R. Yang, Y.Y. Wang, and C.C. Wan, “Composition analysis of the passive film on the carbon electrode of a lithium-ion battery with an EC-based electrolyte,” *J. Power Sources*, vol. 72, pp. 66–70, 1998.

[65]. L. E Ouatani, R. Dedryvère, J.-B. Ledeuil, C. Siret, P. Biensan, J. Desbrières, and D. Gonbeau, “Surface film formation on a carbonaceous electrode: Influence of the binder chemistry,” *J. Power Sources*, vol.189, pp. 72–80, 2009.

[66]. D.Lu, M. Xu, L. Zhou, A. Garsuch, and B.Lucht, “Failure mechanisms of graphite/$LiNi_{0.5}Mn_{1.5}O_4$ cells at high voltage and elevated temperature,” *J. Electrochem. Soc.*, vol. 160(5), pp.A3138, 2013.

[67]. J.S. Gnanaraj, R.W Thompson, S.N Iaconatti, and J.F DiCarlos, “Formation and growth of surface films on graphitic anode materials for Li-Ion batteries,” *J. Electrochem. Solid state Lett*. vol. 8(2) pp.A128, 2005.

[68]. X. Wu, H. Li, L. Chen, and X. Huang, “Agglomeration and the surface passivation film of Ag nano-brush,” *Solid State Ionics*, vol. 149 pp.185– 192, 2002.

[69]. M. Kassem, and C. Delacourt, “Postmortem analysis of calendar-aged graphite/$LiFePO_4$ Cells,” *J. Power Sources*, vol. 235 pp. 159-171, 2013.

[70]. H. Maleki, G. Deng, A. Anani, and J. Howard, “Thermal Stability Studies of Li-Ion Cells and Components,” *J. Electrochemical Soc*., vol. 146 (9), pp.A3224, 1999.

[71]. M. Safaria, and C. Delacourt, “Aging of a Commercial Graphite/$LiFePO_4$ cell batteries and energy storage,” *J. Electrochemical Soc*., vol.158 (10), pp.A1123, 2011.

[72]. M. Lu, H. Cheng, and Y. Yang, “A comparison of solid electrolyte interphase (SEI) on the artificial graphite anode of the aged and cycled commercial lithium ion cells”, *Electrochim Acta*, vol. 53, pp.3539-3546, 2008.

[73]. G.V Zhuang, H. Yang, B. Blizanac, and P. N. Ross Jnr., “A study of electrochemical reduction of ethylene and propylene carbonate electrolyte on graphite using ATR-FTIR spectroscopy,” *J. Electrochem. Solid State Lett.* vol. 8(9), pp. A411, 2005.

[74]. Y. Domi, M. Ochida, S. Tsubouchi, H. Nakagawa, T. Yamanaka, T. Doi,T. Abe, and Z. Ogumi, "In Situ AFM study of surface film formation on the edge plane of HOPG for Lithium-Ion batteries," *J. Phys. Chem. C.*, vol. 115, pp.25484–25489, 2011.

[75]. J. S. Gnanaraj, R. W. Thompson, S. N. Iaconatti, J. F. DiCarlo, and K. M. Abraham,"Formation and growth of surface films on graphitic anode materials for Li-Ion Batteries," *J. Electrochem. Solid-State Lett.*, vol. 8 (2), pp. A128, 2005.

[76]. H.Ota, Y. Sakata, J. Sasahara, and E.Yasuwa, "Characterization of lithium electrode in lithium Imides/ethylene carbonate and cyclic ether electrolytes," *J. Electrochem.Soc*., vol. 151(3), pp.A437, 2004.

[77]. C. Tran, J. Kafle, X.Q Yang, and D. Qu, "Increased discharge capacity of a Li-air activated carbon cathode produced by preventing carbon surface passivation," *Carbon*, vol. 49, pp.1266 –1271, 2011.

[78]. D. Aurbach and M. Mashkovich, "A Study of Lithium deposition-dissolution processes in a few selected electrolyte solutions by electrochemical quartz," *J. Electrochem. Soc*., Vol. 145( 8), pp.A2629, 1999.

[79]. H. Nakahara, S.Y Yoon , T. Piao, F. Mansfeld, and S. Nutt, "Analysis of the passive surface film on a graphite electrode charged in polysiloxane-based electrolyte," *J. Power Sources*, vol. 158 pp.591–599, 2006.

[80]. N. Dupré, J.F Martin, J. Degryse, V. Fernandez, P. Soudan, and D. Guyomard, "Aging of the $LiFePO_4$ positive electrode, interface in electrolyte," J. Power Sources, vol. 195, pp. 7415-7425, 2010.

[81]. S. Xiaong, K. Xie, Y. Diao, and X. Hong, "Characterization of the solid electrolyte interphase on lithium anode for preventing the shuttle mechanism in lithium-sulfur batteries," *J. Power sources*, vol. 246 pp.840-845, 2014.

[82]. D.P. Abraham, M.M. Furczon, S.-H. Kang, D.W. Dees, and A.N. Jansen, "Effect of electrolyte composition on initial cycling and impedance characteristics of lithium-ion cells," *J. Power Sources*, vol. 180 pp. 612–620, 2008.

[83]. J. Vetter, P. Novak, M.R. Wagner, C. Veit, K.C. Moller, J.O. Besenhard, M. Winter, M. Wohlfahrt-Mehrens, C. Vogler, and A. Hammouche, "Ageing mechanisms in lithium-ion batteries," *J. Power Sources,* vol. 147 pp.269-281, 2005.

[84]. H. Maleki, G. Deng, A. Anani, and J. Howard, "Thermal Stability Studies of Li-Ion Cell and Components," *J. Electrochemical Soc*., vol.146 (9), pp.A3224, 1999.

[85]. C. Huang, S. Zhuang, and F.Tu, "Electrode/electrolyte interfacial behaviors of LiCoO2/mixed graphite Li-Ion cells during Operation and Storage," *J. Electrochem. Soc.*, vol.160 (2), pp. A376, 2013.

[86]. R. Dedryvère, H. Martinez, S. Leroy , D. Lemordant, F. Bonhomme, P. Biensan, and D. Gonbeau, "Surface film formation on electrodes in a LiCoO2/graphite cell: A step by step XPS study," J. *Power Sources*, vol.174 pp. 462–468, 2007.

[87]. Y. Okamoto, "Ab Initio Calculations of Thermal Decomposition Mechanism of LiPF6-Based Electrolytes for Lithium-Ion Batteries," *J. Electrochem. Soc*. vol.160 (2) pp. A404, 2013.

[88]. P.Novak, M. Lanz, D. Allia, B. Rykart, J. Paniz, and O. Haas, "The complex electrochemistry of graphite electrodes in lithium-ion batteries," *J. Power Sources*, vol. 97, pp. 39–46, 2001.

[89]. F.Joho, and P. Nova´k, "SNIFTIRS investigation of the oxidative decomposition of organic-carbonate-based electrolytes for lithium-ion cells," *Electrochimica Acta*., vol.45 pp.3589–3599, 2000.

[90]. Y. Yamada, Y. Iriyama, T. Abe, and Z. Ogumi, "Kinetics of lithium ion transfer at the interface between graphite and liquid electrolyte: effects of solvent and surface film," *Langmuir*,vol. 25(21), pp. 12766-12770, 2009.

[91]. C. L. Campion,W. Li, W.B. Euler, B.L. Lucht, B. Ravdel, J.F. DiCarlo, R. Gitzendanner, and K. M. Abraham, Suppression of Toxic Compounds Produced in the decomposition of Lithium-Ion battery electrolytes," *J. Electrochem. Solid-State Lett.*, vol. 7(7), pp. A194, 2004.

[92]. S. Leroy, Hartinez, R. Dedryvere, D. Lemordant, and D. Goneau, "Influence of the lithium salt nature over the surface film formation on a graphite electrode in Li-ion batteries," *Appl. Surf. Sci.* vol. 253, pp. 4895-4905, 2007.

[93]. A. Schechter, and D. Aurbach, "X-ray Photoelectron spectroscopy study of surface films formed on Li electrodes freshly prepared in Alkyl carbonate solutions," *Langmuir*, vol. 15, pp.3334-3342,1999.

[94]. M. Broussely, P.H Biensan, F. Bonhomme, P.H Balnchard, S. Herreyre, K. Nechev, and R.J Staniewicz, “Main aging mechanisms in lithium ion batteries,” *J. Power Sources*, vol. 146, pp. 90-96, 2005.

[95]. H. Yamada, Y. Watanabe, and I. Moriguchi, T. Kudo, “Rate capability of lithium intercalation into nano-porous graphitized carbon,” *Solid State Ionics*,vol. 179, pp. 1706-1709, 2008.

[96]. M.Wolfgang, C. Lu, and P. Novak, “Morphology of the solid electrolyte interphase of the graphite: a dependency of the formation current,” *J. Electrochem. Soc.*, vol.158, pp. A1478, 2011.

[97]. H. Wang, Y. Jang, B. Huang, R.D. Sadoway, and Y.M Chiang, “EM Study of electrochemical cycling-induced damage and disorder in $LiCoO_2$ cathode for rechargeable Lithium batteries,” *J. Electrochem. Soc*., vol.146, pp.A473, 1999.

[98]. Z. Lu, Y. Li, and Y. Guo, “Thermal behavior and decomposition kinetics of six electrolyte salts by thermal analysis,” *J. Power Sources*, vol. 156, pp. 555–559,2006.

[99]. E. Endo, K.Tanaka, and K. Sekai, “Initial reaction in the reduction decomposition of electrolyte solutions,” *J. Electrochem. Soc*., vol.147 (11), pp. A4029, 2000.

[100]. S.Wilken, P. Johansson, and P. Jacobsson, “Infrared spectroscopy of instantaneous decomposition products of $LiPF_6$-based lithium battery electrolytes,” *Solid State Ionics*, vol. 225 pp. 608–610, 2012.

[101]. C.L. Campion, W. Li, and B.L. Lucht, “Thermal decomposition of $LiPF_6$-based electrolytes for Lithium-Ion batteries,” *J. Electrochem. Soc*., vol.152 (12), pp. A2327, 2005.

[102]. S.E. Sloop, J.B. Kerr, and K. Kinoshita, “The role of Li-ion battery electrolyte reactivity in performance decline and self-discharge,” *J. Power Sources*, vol. 119 pp. 330–337, 2003.

[103]. S.W Song, and S.W. Baek, Surface layer formation on Sn anode: “ATR FTIR spectroscopic characterization,” *Electrochimica Acta*, vol. 54 pp. 1312–1318, 2009

[104]. K.Tasaki, K. Kand, S.Nakamura, and M. Ue, "Decomposition of $LiPF_6$ and stability of $PF_5$ in Li-Ion battery electrolytes density functional theory and molecular dynamics Studies," *J. Electrochem. Soc.*, vol.150 (12), pp. A1628, 2003.

[105]. L.Terborg, S. Weber, F. Blaske, S. Passerini, M. Winter, K. Uwe, and S. Nowak, "Investigation of thermal aging and hydrolysis mechanisms in commercial lithium ion battery electrolyte," *J. Power Sources,* vol. 242 pp.832-837, 2013.

[106]. T. Kawamura, S. Okadaa, and J. Yamaki, "Decomposition reaction of $LiPF_6$-based electrolytes for lithium ion cells," *J. Power Sources*, vol. 156 pp.547–554, 2006.

[107]. Y.G Ryu, and S. Pyun, "Passivation kinetics of surface films formed on a graphite electrode inorganic lithium salt solution as a function of salt anion type," *J. Electroanalytical Chem*., vol. 433, pp. 97-105, 1997.

[108]. K. Kumai, T. Ikeya , K. Ishihara, T. Iwahori, N. Imanishi,Y.Takeda, and O.Yamamoto,"Degradation mechanism due to decomposition of organic electrolyte in Li/$MoS_2$, cells during long cycling," *J. Power Sources*, vol.70 pp.235-239, 1998.

[109]. S. E. Sloop, J. K. Pugh, S. Wang, J. B. Kerr, and K. Kinoshita, "Chemical reactivity of $PF_5$ and $LiPF_6$ in ethylene carbonate/dimethyl carbonate Solutions," *J. Electrochem. Solid-State Lett.,*, vol. 4(4), pp. A42, 2001.

[110]. W. Li, C. Campion, B.L. Lucht, B. Ravdel, J.Dicarlo, and K.M Abraham, "Additives for stabilising $LiPF_6$ based electrolyte against thermal decomposition," *J. Electrochem. Soc.*, vol. 152(7), pp. A1361, 2005.

[111]. P. Röder, N. Baba, K.A. Friedrich, and H.-D. Wiemhöfer, "Impact of delithiated $LiFePO_4$ on the decomposition of $LiPF_6$-based electrolyte studied by accelerating rate calorimetry," *J. Power Sources*, vol. 236, pp. 151-157, 2013.

[112]. K. Edstrom, A.M Anderson, A. Bishop, L. Framsson, and J. Lingren, "Carbon electrode morphology and thermal stability of the passivation layer," *J. Power Sources, vol.* 97, pp. 87-91, 2001.

[113]. M.Endo, C. Kim, K.Nishimura, T. Fujino, and K. Miyashita, “Recent development of carbon materials for Li Ion batteries,” *Carbon*, vol. 38, pp. 183-197,2000.

[114]. B.V. Ratnakumar, and M.C. Smart, “Lithium plating behavior in lithium-ion Cells,” *J. Electrochem. Soc. Trans.*, vol. 25, pp. 241-252, 2010.

[115]. S.Brown, K.Ogawa, Y. Kumeuchi, S. Enomoto, M. Uno, H.Saito, S. Yoshisugu, D. Abraham, and G. Lindberg, “Cycle life evaluation of 3 Ah Li$x$Mn$_2$O$_4$-based lithium-ion secondary cells for low-earth-orbit satellites,” *J. Power Sources,* vol. 185, pp. 1444–1453, 2008.

[116]. R. Kostecki, J. Lei, F. McLarnon, J. Shim, and K. Striebel, “Diagnostic evaluation of detrimental phenomena in high-power lithium-ion batteries,” *J. Electrochem. Soc*.vol. 153, pp. A669, 2006.

[117]. M. Safari, and C. Delacourt, “Aging of a commercial graphite LiFePO4 cell,” *J. Electrochem. Soc.*, vol. 158, pp. A1123, 2011.

[118]. N.N. Sinha, A.J. Smith, J.C. Burns, J. Gaurav, K.W. Eberman, E. Scott, J.P. Gardner, and J.R. Dahn, “The use of elevated temperature storage experiments to learn about parasitic reaction in wound LiCoO$_2$/graphite cells,” *J. Electrochem*. vol. 158, pp.1194–1201, 2011.

[119]. N.N. Sinha, T.H. Marks, H.M. Dahn, A.J. Smith, J.C.Burn, D.J.Coyle, J.J.Dahn and J.R. Dahn, “The rate of active lithium loss from a soft carbon negative electrode as a function of temperature, time and electrode potential,” *J. Electrochem. Soc.*, vol.159, pp.1672–1681, 2012.

[120]. P.Novak, M. Lanz, D. Allia, B. Rykart, J.Paniz, and O. Haas, “The complex electrochemistry of graphite electrodes in lithium-ion batteries,” *J. Power Sources,* vol. 97, pp. 39–46, 2001.

[121]. H.Wang, Y. Jang, B. Huang, R.D. Sadoway, and Y.M Chiang, “TEM study of electrochemical cycling-Induced damage and disorder in LiCoO$_2$ Cathodes for rechargeable Lithium Batteries,” *J. Electrochem. Soc.* vol. 146, pp.A473, 1999.

[122]. A.R. Leising, M.J. Palazzo, S.E. Takeuchi, and J.K. Takeuchi, “Abuse testing of Lithium-Ion batteries characterization of the overcharge reaction of LiCoO$_2$/Graphite Cells,” *J. Electrochem. Soc.*, vol. 148, pp. 838–844, 2001.

[123]. M. Lanz, and P. Novak, “DEMS study of gas evolution at thick graphite electrodes for lithium-ion batteries: The effect of the ϒ-butyrolactone,” *J. Power Sources, ,* vol. 102, pp. 277–282, 2001.

[124]. M.C. Smart, and B.V. Ratnakumar, “Effects of electrolyte composition on lithium plating in lithium-ion cells,” *J. Electrochem. Soc*., vol. 158, pp. A379, 2011.

[125].H. Honbo, K. Takei, Y. Ishii, and T. Nishida, “Electrochemical properties and Li deposition morphologies of surface modified graphite after grinding,” *J. Power Sources* , , vol. 189, pp. 337–343, 2009.

[126]. M. Rosso, T. Gobron, C. Brissot, J.N. Chazalviel, and S. Lascaud, “Onset of dendritic growth in lithium/polymer cells,” *J. Power Sources,* vol. 97, pp. 804–806, 2001.

[127]. F.Ornini, D.A. Pasquier, B. Beaudion, J.M. Tarason, and M. Trentin, “In situ scanning electron microscope observation of interfaces within plastic lithium batteries,” *J. Power Sources,* vol. 76,pp. 19–29, 1998.

[128]. R.A. Leising, M.J. Palazzo, E.S. Takeuchi, and K.J. Takeuchi, “A study of the overcharge reaction of lithium-ion batteries,” *J. Power Sources*, vol. 97, pp. 681–683, 2001.

[129]. W.Kim, and W. Yoon, “Observation of dendritic growth on Li powder anode using the optical cell,” *Electrochim. Acta*, vol. 50, pp. 541–545, 2004.

[130]. E. Markervich, G. Salitra, M.D. Levi, and D. Aurbach, “Capacity fading of Lithiated graphite electrodes studied by a combination of electroanalytical methods, Raman spectroscopy and SEM,” *J. Power Sources*, vol. 146, pp. 146–150,2005.

[131]. M. Hossein, D.Guoping, A.Anaba, and J. Howard, “Thermal stability studies of Li-Ion cells and components,” *J. Electrochem. Soc*., vol. 146, pp. A3224, 1999.

[132]. Y.Chang, H. Li, L.Wu, and T. Lu, “Irreversible capacity loss of graphite electrode In lithium-ion batteries,” *J. Power Sources*, vol. 68, pp. 187–190, 1997.

[133]. A.J. Smith, M. Hannah, and J.R. Dahn, “Long-term low rate cycling of $LiCoO_2$ graphite Li-ion cells at 55°C,” *J. Electrochem. Soc.vol.* 159, pp.705–710, 2012.

[134]. D.P. Abraham, E.M. Reynolds, E. Samman, A.N. Jansen, and D.W. Dees, “Aging characteristics of high-power lithium ion cells with $LiNi_{0.8}Co_{0.15}Al_{0.05}O_2$ and $Li_{4/3}Ti_{5/3}O_4$ electrodes,” *Electrochim. Acta*, vol. 51, pp. 502–510, 2005.

[135]. M. Ochida, Y. Domi, T. Doi, S. Tsubouchi, H. Nakagawa, T. Yamanaka, T. Abe, and Z. Ogumi, “Influence of manganese dissolution on the degradation of surface films on edge plane graphite negative-electrodes in lithium -ion batteries,” *J. Electrochem. Soc.*, vol.159, pp. A961, 2012

[136]. K. Kumaresan, O. Guo, P. Ramada, and R.E. White, “Cycle life performance of lithium-ion pouch Cells,” *J. Power Sources*, vol. 158, pp. 679–688, 2006.

[137]. D.P. Abraham, J. Liua, C.H. Chen, Y.E. Hyung, M. Stolla, N. Elsena, S. MacLaren, R. Twesten, R. Haasch, and E. Sammann, “Diagnosis of power fade mechanisms in high-power lithium-ion cells,” *J. Power Sources*, vol. 119, pp. 511–516, 2003.

[138]. L. Bodenes, R. Dedryvere, H. Martinez, F. Fischer, C. Tessier, and J.P. Peres, “Lithium-ion batteries working at 85°C: Aging phenomena and electrode/electrolyte interfaces studied by XPS,” *J. Electrochem. Soc. vol.* 159, pp. A1739, 2012.

[139]. S. Lee, and S. Pyun, “The effect of electrolyte temperature on the passivity of the solid Electrolyte interphase formed on a graphite,” *Carbon*, vol. 40, pp. 2333–2339, 2002.

[140]. G. Ning, B. Haran, and B.N. Popov, “Capacity fade of lithium ion batteries cycled at high discharge rates,” *J. Power Sources*, vol. 117, pp. 160–169, 2003.

[141]. B. Markovsky, A. Rodkin, Y.S. Cohen, O. Palchik, E. Levi, D. Aurbach, H.-J. Kim, and M. Schmidt, “The study of capacity fading processes of Li-ion batteries: Major factors that play a role,” *J. Power Sources, vol.* 119–121, pp. 504–510, 2003.

[142]. J.W. Braithwaite, A. Gonzales, G. Nagasubramanian, S.J. Lucero, D.E. Peebles, J.A. Ohlhausen, and W.R. Cieslak, “Corrosion of lithium-ion battery current collectors,” *J. Electrochem. Soc.* vol.146, pp.A448, 1999.

[143].J.S. Kim, and Y.T. Park, “Characteristics of surface films formed at a mesocarbon Microbead electrode in a Li-ion battery,” *J. Power Sources*, vol. *91*, pp.172–176, 2000.

[144]. J. Li, E. Murphy, J. Winnick, and A.P. Kohl, "The effect of pulse charge on cycling characteristics of commercial lithium-ion batteries," *J. Power Sources,* vol. 102, pp. 302–309, 2001.

[145]. M. Broussely, S. Herreyre, B. P. Kasztejna, P. Nechev, and K. Staniewicz, "Aging mechanisms in Li ion cells and calendar life predictions," *J. Power Sources,* vol. 97, pp. 13–21, 2001.

[146]. J. Li, E. Murphy, J. Winnick, and P.A. Kohl, "Studies on the cycle life of commercial lithium ion batteries during the charge-discharge cycling," *J. Power Sources,* vol. 102, pp. 294–301, 2001.

[147]. D. Aurbach, B. Markovsky, Y. Talyossef, G. Salitra, H. Kim, and S. Choi, "Studies of cycling behaviour, ageing, and interfacial reactions of $LiNi_{0.5}Mn_{1.5}O_4$ and carbon electrode for lithium-ion 5-V cells," *J. Power Sources,* vol. 162, pp. 780–789, 2006.

[148]. C. Keun, R. Yin, S. Shin, Y. Lee, W. Choi, and Y. Kim, "Electrochemical properties and gas evolution behavior of overlithiated $Li_2NiO_2$ as cathode active mass for rechargeable Li ion batteries," *J. Electrochem. Soc.* vol. 159, pp A887, 2012.

[149]. V. Agubra and J. Fergus, "Lithium Ion Battery Anode Aging Mechanisms," *Materials,* vol. 6, pp. 1310-1325, 2013,

[150]. K.Nakura, Y. Ohsugi, M. Imazaki, K. Ariyoshi, and T. Ohzuku, "Extended cycle Life of lithium-ion batteries consisting of lithium insertion electrodes: cycle efficiency versus Ah efficiency," *J. Electrochem. Soc.* vol. 158, pp. A1243, 2011.

[151]. J. Shim, and K. Striebel, "Characterization of high-power lithium-ion cells during constant cycling: Part I cycling performance and electrochemical diagnostics," *J. Power Sources,* vol. 122, pp.188–194, 2003.

[152]. J.Shim, R. Kostecki, T. Richardson, and X. Song, "Striebel, Electrochemical analysis for cycle performance and capacity fading of a lithium-ion battery cycled at elevated temperature," *J. Power Sources, vol.* vol. 112, pp.222–230, 2002.

[153]. I. Belharouak, G. Koening, T. Tan, H. Yumoto, and N. Ota, "Performance Degradation and gassing of $Li_4Ti_5O_{12}/LiMn_2O_4$ lithium-ion cells," *J. Electrochem. Soc.* vol. 159, pp. A1165, 2012.

[154]. M.D. Levi, C.Wang, J.S. Gnanara, and D. Aurbach, “Electrochemical behavior of graphite anode atelevated temperature in organic carbonate solution,” *J. Power Sources,* vol. 119, pp. 538–542, 2003.

[155]. P. Ramadass, B, Haran, R, White, and B N. Popov, “Capacity fade of Sony 18650 cells cycled at elevated temperatures Part I. Cycling performance,” *J. Power Sources,* vol.112, pp. 606–613 2002.

[156]. B. Haran, R. White, and B.N. Popov, “Capacity fade of Sony 18650 cells cycled at elevated temperatures Part II. Capacity fade analysis,” *J. Power Sources*, vol. 112, pp. 614–620, 2002.

[157]. Y.Zhang, and C.Wang, X. Tang, “Cycling degradation of automotive $LiFePO_4$ lithium-ion battery,” *J. Power Sources*, vol. 196, pp. 1513–1520, 2011.

[158]. L.Yang, M. Takahashi, and B. Wang, “A study on capacity fading of lithium-ion battery with a manganese positive electrode during cycling,” *Electrochim. Acta*, vol. 51, pp. 3228–3234, 2006.

[159]. J.Shim, and A.K. Striebel, “The dependence of natural graphite anode performance on electrode density,” *J. Power Sources,* , vol. 130, pp. 247–253, 2004.

[160]. Y.Lai, Z.Cao, S.Haishen, Z. Zhang, X.Chen, H. Lu, M. Jia, and J. Li, “Influence of Fe(II) species in electrolyte on performance of graphite anode for lithium-ion Batteries,” *J. Electrochem. Soc.*, vol. 159, pp. A1961, 2012.

[161]. K. Rhodes, M.Kirkham, R.Meisner, M.C.Parish, and N. Dudney, “Novel cell Design for combined in situ acoustic emission and x-ray diffraction study during electrochemical cycling of batteries,” *Rev. Sci. Instrum.*, vol. 82, pp. 75–107, 2011,

[162]. S.C. Nagpure, B.Bhushan, S. Babu, and G. Rizzoni, “Scanning spreading resistance characterization of aged Li-ion batteries using atomic force microscopy,” *Scripta Mater*, vol.60, pp.933–936, 2009

[163]. T. Ohzuku, A.Ueda, N. Yamamoto, and I. Yasunobu, “Factor affecting the capacity retention of lithium-ion cells,” *J. Power Sources*, vol.54, pp.99–102, 1995

[164]. S.K.Jeong, M.Inaba, A.Takeshi, and Ogumi, Z. “Surface film formation on graphite negative electrode in lithium-ion batteries,” *J. Electrochem. Soc*., vol.148, pp. A989, 2001.

[165]. S.R.Silvakkumar, and J.Y. Nerkar, “Rate capability of graphite materials as negative electrodes in lithium ion capacitors,” *Electrochim. Acta,* vol. 55, pp. 3330–3335, 2010.

[166]. B.Simon, S.Flandrois, K.Guerin, A.Ferrier-Bouvier, I.;Teulat, and P. Biensan, “On the choice of graphite for lithium ion batteries,” *J. Power Sources,* vol. 81, pp. 312–316, 1999.

[167]. P.Ridgway, H.Zheng, A.F.Bello, X.Song, S.Xun, J.Chong, and B. Vincent, “Comparison of cycling performance of lithium ion cell anode graphites,” *J. Electrochem. Soc.* vol. 159, pp. A520, 2012.

[168]. A.M. Anderson, K. Edstrom, and J.O. Thomas, “Characterization of the ambient and elevated temperature performance of graphite electrode”, *J. Power Sources,* vol.81–82, pp. 8–12, 1999.

[169]. A. N Richard and O.K Ronald, “Infrared spectra of inorganic compound,” *academic press, new York and London*, pp. 351-361 1971.

[170]. S.I Pyun, and Y.G Ryu, “In-situ spectroelectrochemical analysis of the passivating surface film formed on a graphite electrode during the electrochemical reduction of lithium salts and organic carbonate solvent,” *J. Electroanal. Chem*. vol. 455, pp.11, 1998

[171]. M. Masaki, K. Dokko, and K. Kanamura, “Dynamic behavior of surface film on $LiCoO_2$ thin film electrode,’ *J. Power Sources,* vol.177**,** pp. 184-193, 2008.

[172]. D. Aurbach, and E.E Yair, “The study of Li-graphite intercalation processes in several electrolyte systems using in situ X-ray diffraction,” *J. Electrochem. Soc.,* vol.142, pp. A1746, 1995.

[173]. N. Takami, A. Satoh, M.Hara, and T. Ohsaki, “Structural and kinetic characterization of lithium Intercalation into carbon anodes for secondary lithium batteries,” *J. Eleetrochem. Soc.*, vol.142, pp.A371, 1995.

[174]. J. M. Tarascon, and D. Guyomard, The $Li_{1+x}Mn_2O_4$/C rocking-chair system: a review,” *Electrochimica Acta*, vol.38 pp.1221-1231,1993.

[175]. B. Xu, M. S. Wu, G. Liu, and C. Y. Ouyang, “Understanding the effect of the layer-to-layer distance on Li-intercalated graphite,” *J. Appl. Phys.* Vol. 111, pp. 124-325, 2012.

[176]. J. R. Dahn, R. Fong, and M.J Spoon, “Suppression of staging in lithium-Intercalate carbon by disorder in the host,” *Physical Review B*, vol. 42, pp. 6424-3432, 1990.

[177]. Z. X. Shu, R. S. McMillan, and J. J. Murray, “Electrochemical intercalation of Lithium into graphite,” *J. Electrochem. Soc*., vol.140, pp. A922, 1993.

[178]. K. Persson, Y. Hinuma, S. Y Meng, A. Van der Ven, and G. Ceder, “Thermodynamic and kinetic properties of the Li-graphite system from first-principles calculations,” *Physical Review B.,* vol. 82, pp.125416 -125425, 2010.

[179]. C.Huang, S. Zhuang, and F. Tu, “Electrode/Electrolyte Interfacial behaviors of $LiCoO_2$/mixed graphite Li-Ion cells during operation and storage,” *J. Electrochem Soc.* vol. 160, pp. A376, 2013.

[180]. P. Arora, R.E, White, and M. Doyle, “capacity fade mechanism and side reaction in the lithium ion batteries,” J. Electrochem. Soc., vol. 145(10), pp. 3647, 1998.

[181]. E. Peled, “The electrochemical behavior of alkali and alkaline earth metals in nonaqueous battery systems—The solid electrolyte interphase model,” J. Electrochem. Soc., vol. 126(12), pp. 2047-2051, 1979.

# Appendix A

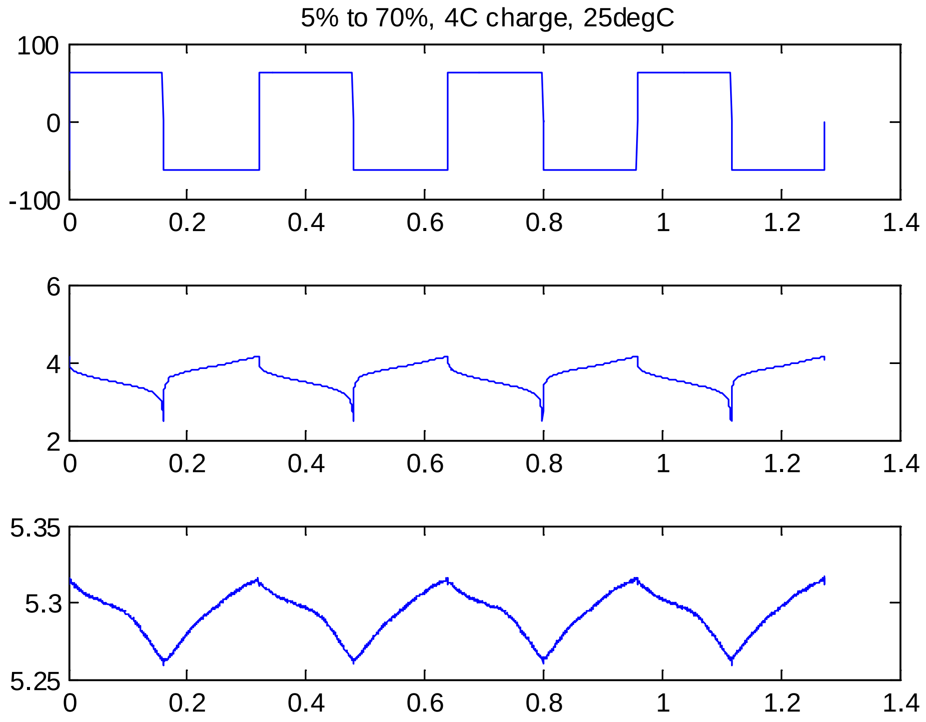
5% to 70%, 4C charge, 25degC
100
0
-100
6
4
2
5.35
5.3
5.25
0
0.2
0.4
0.6
0.8
1
1.2
1.4

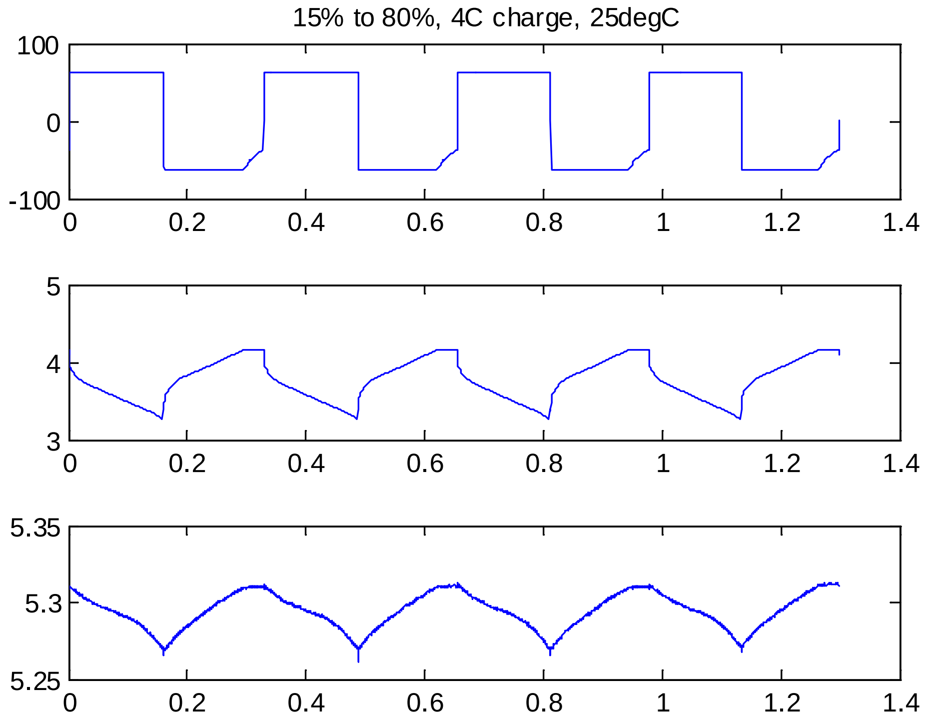
15% to 80%, 4C charge, 25degC
100
0
-100
5
4
3
5.35
5.3
5.25
0
0.2
0.4
0.6
0.8
1
1.2
1.4

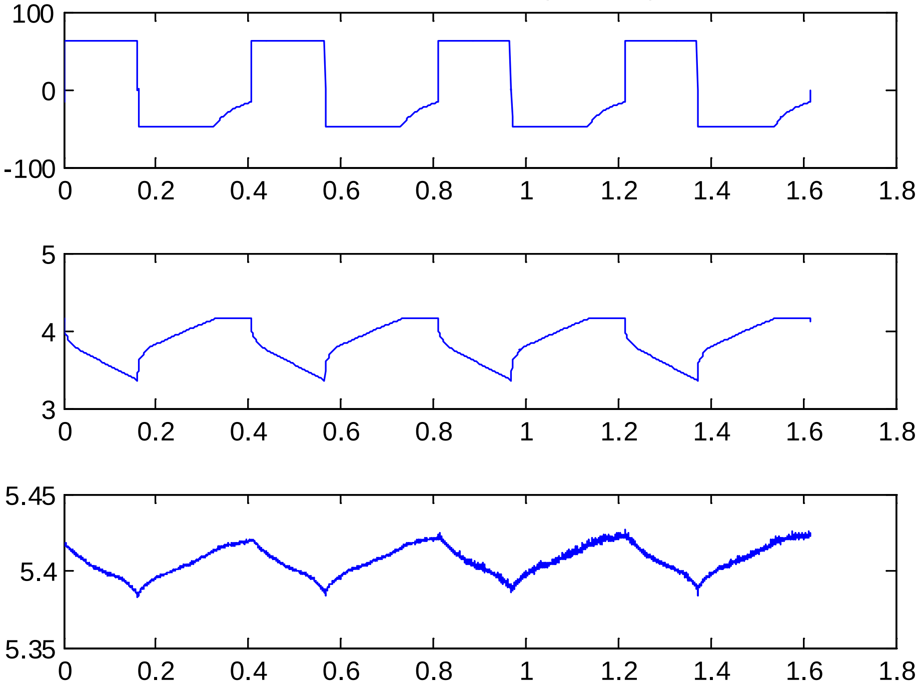
25% to 90%, 3C charge, 25degC

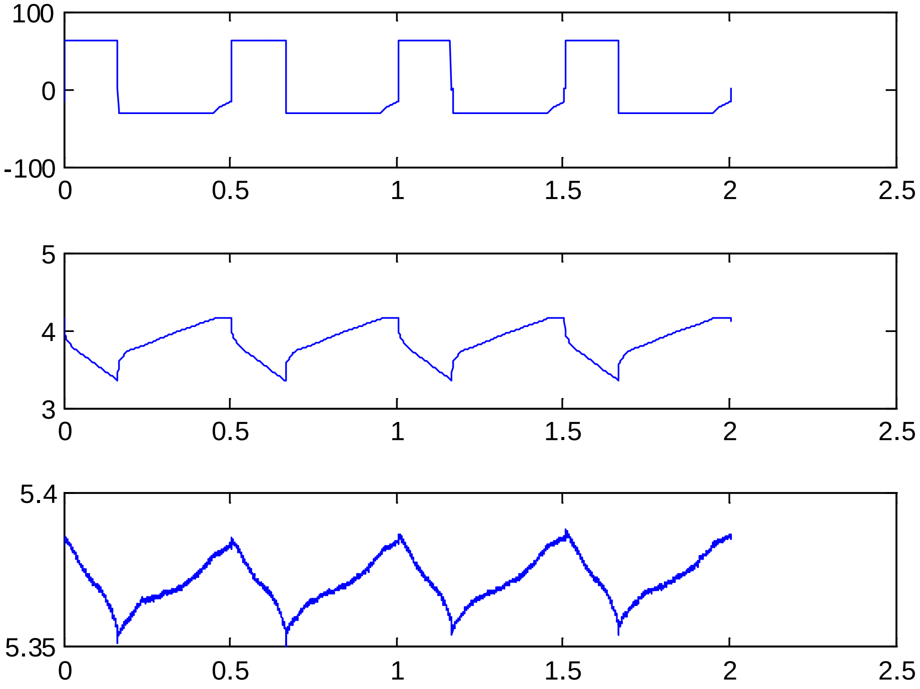
25% to 90%, 2C charge, 25degC

# Appendix B

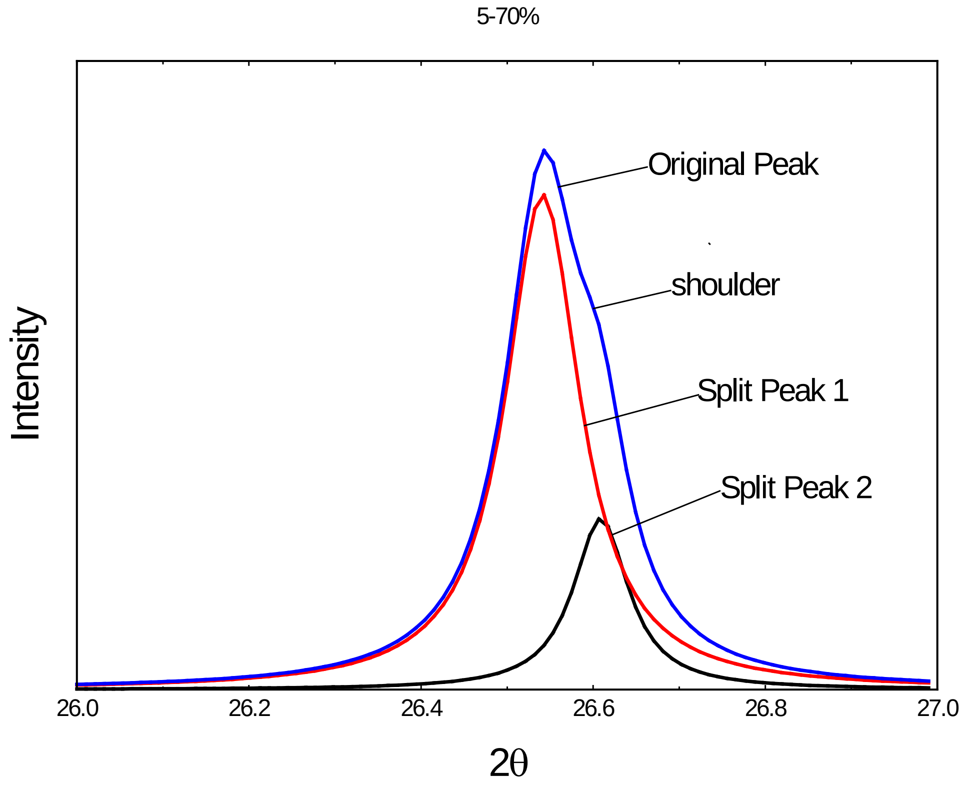

De-convoluted peak for the 2C 5-70% SOC.

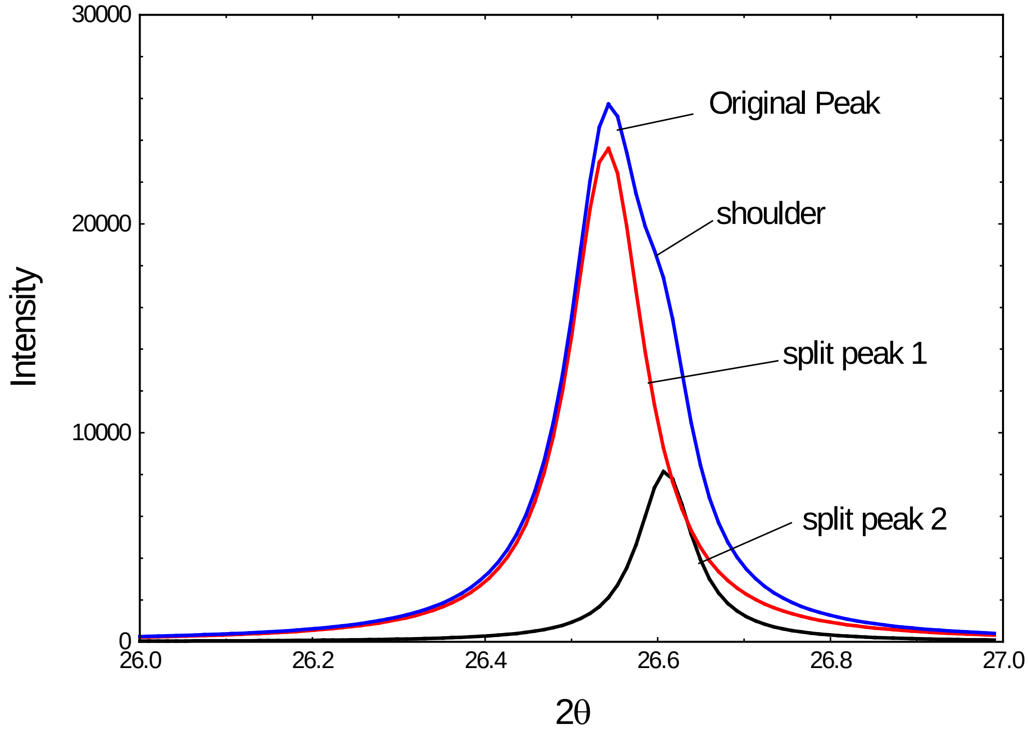

De-convoluted peak for the 3C 5-70% SOC.

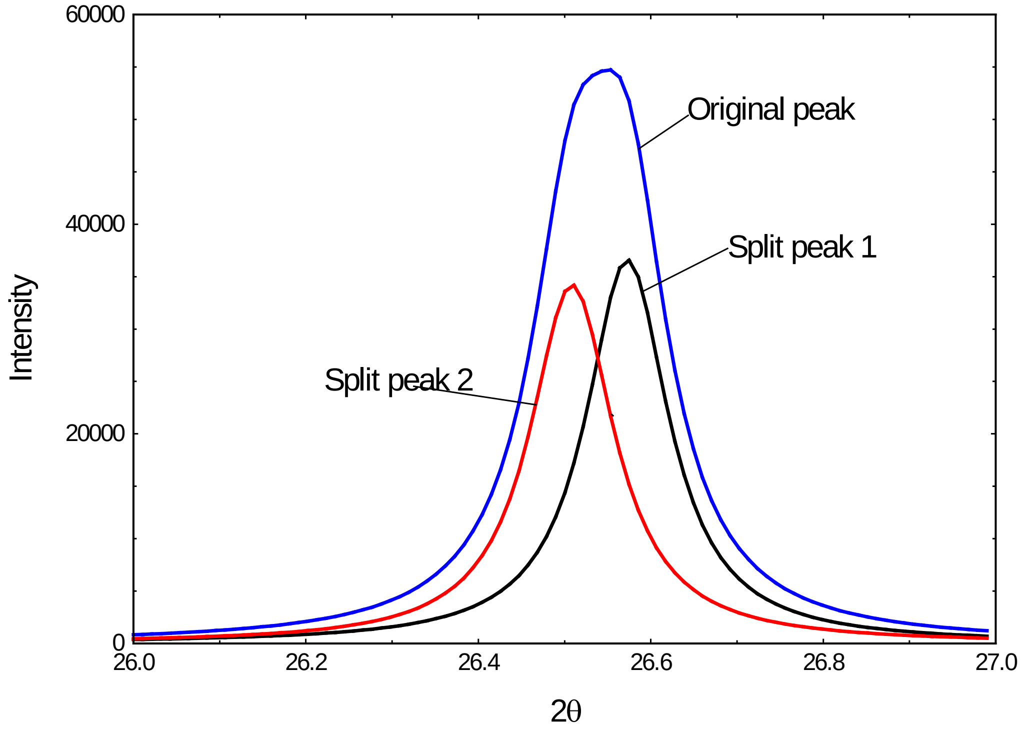

De-convoluted peak for the 4C 15-80% SOC

**Appendix C**: Scatter diagram of each six data points for the measured deposit thickness representing the first three electrodes for each of the different SOCs at 4C charge rate

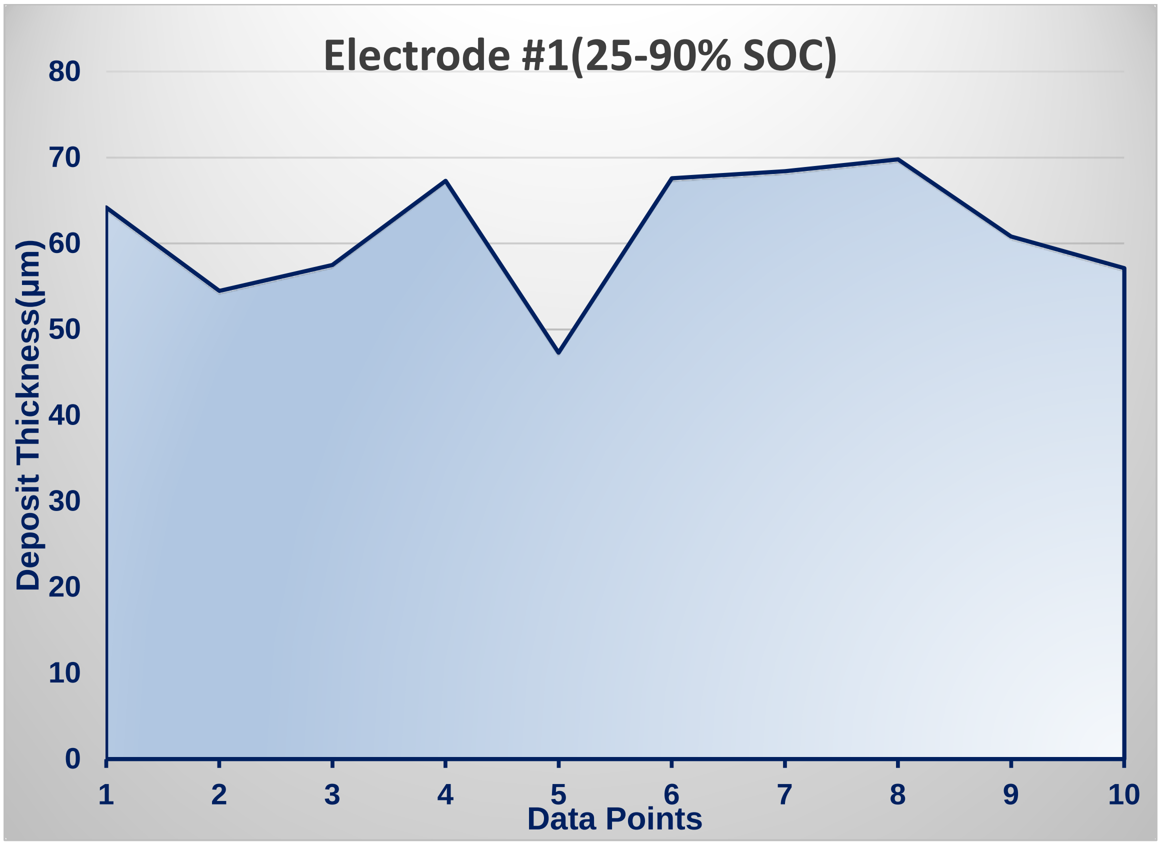

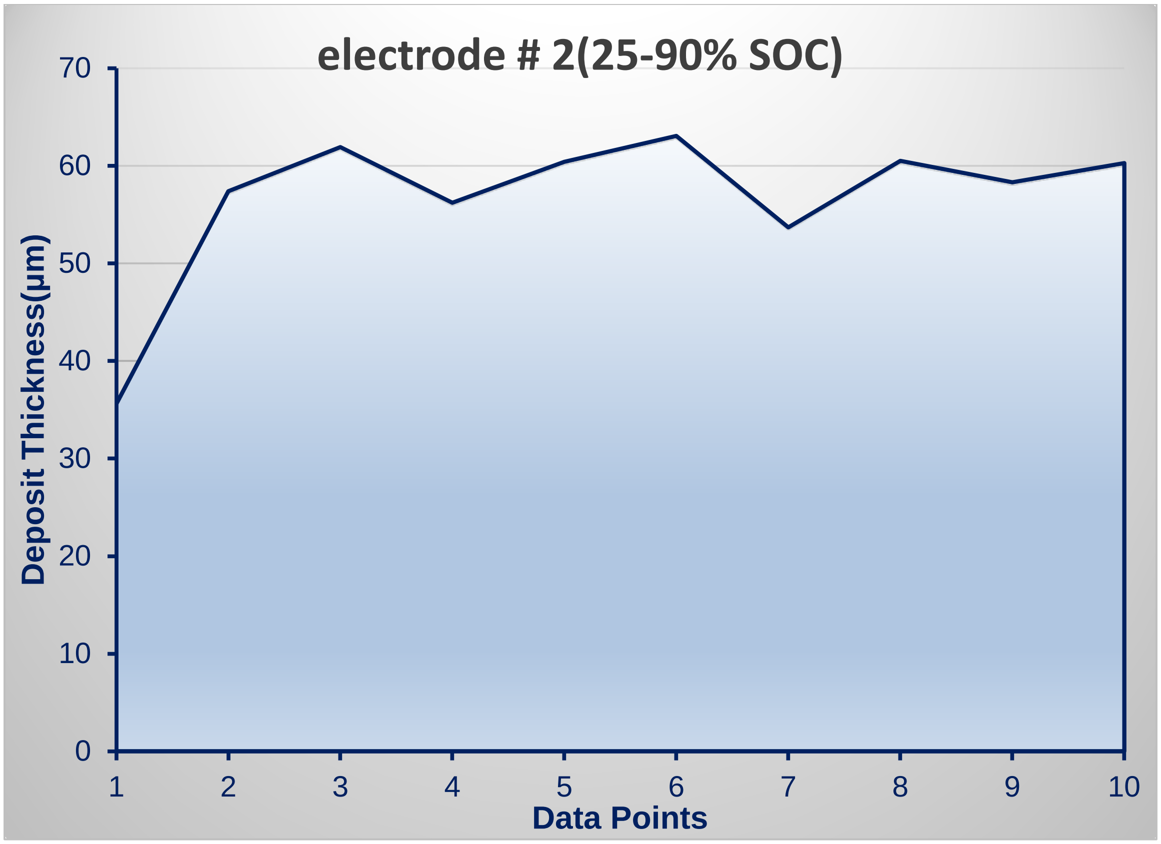
electrode # 2(25-90% SOC)
Deposit Thickness(µm)
70
60
50
40
30
20
10
0
1
2
3
4
5
6
7
8
9
10
Data Points

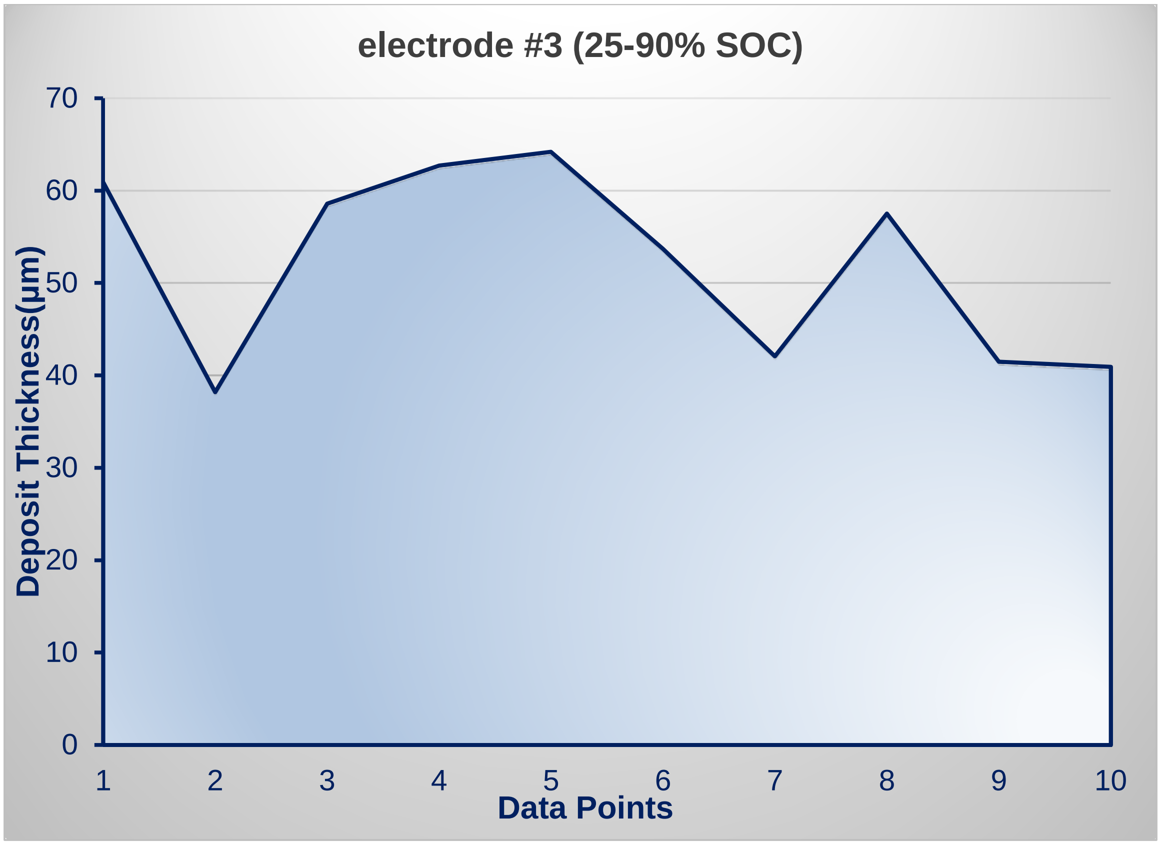
electrode #3 (25-90% SOC)
Deposit Thickness(µm)
70
60
50
40
30
20
10
0
1
2
3
4
5
6
7
8
9
10
Data Points

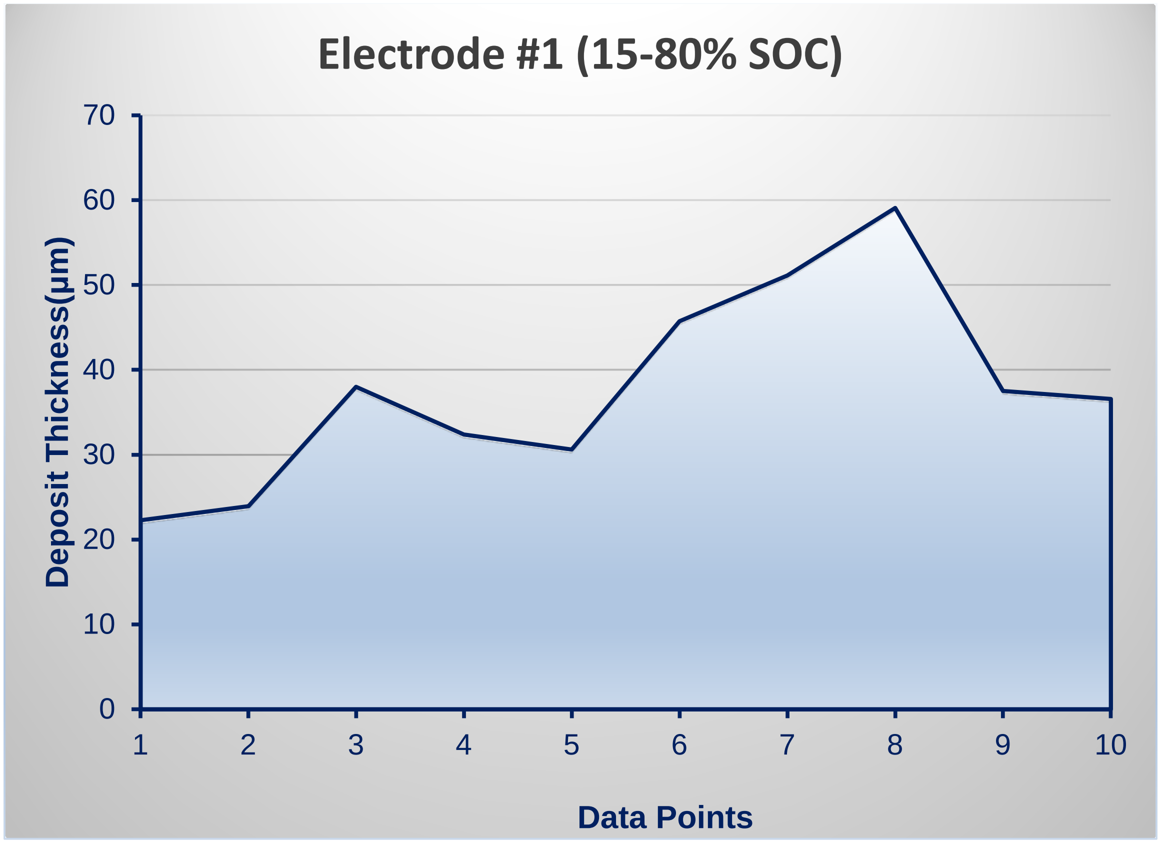
Electrode #1 (15-80% SOC)
Deposit Thickness(µm)
0
10
20
30
40
50
60
70
1
2
3
4
5
6
7
8
9
10
Data Points

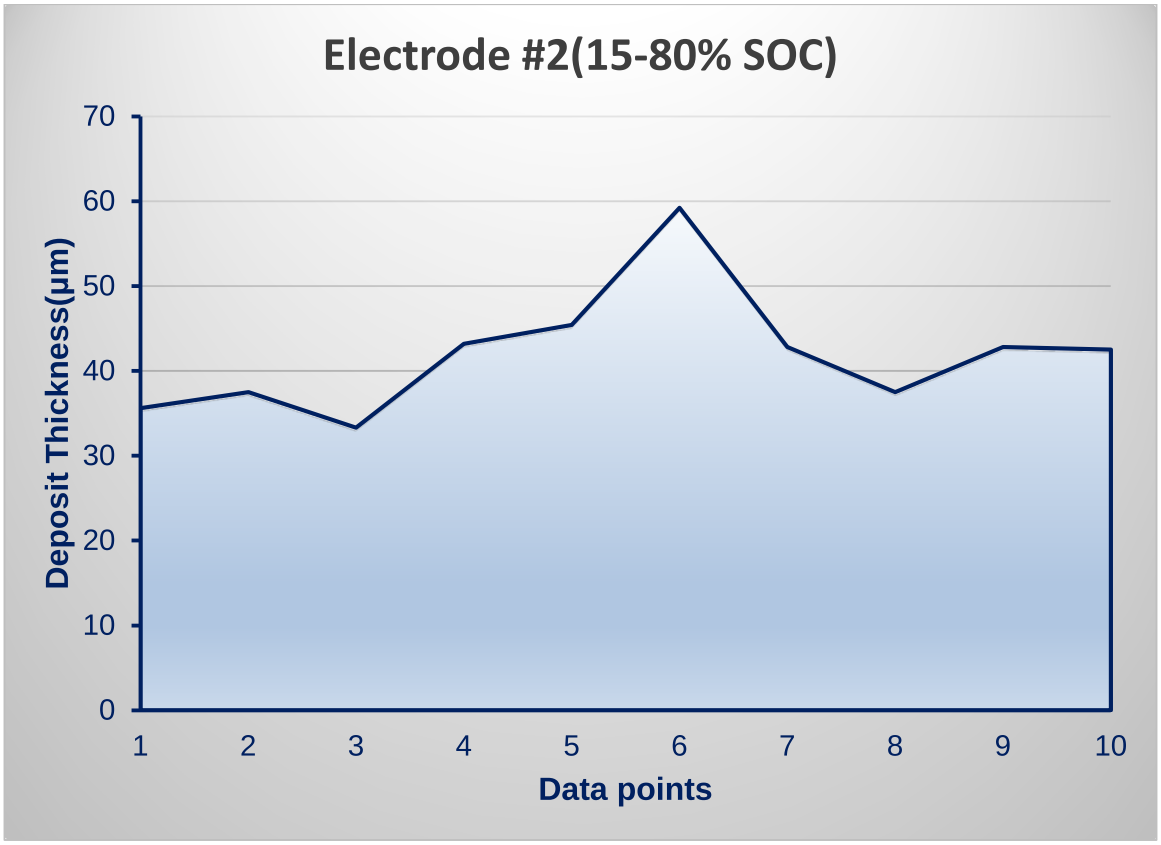
Electrode #2(15-80% SOC)
Deposit Thickness(µm)
0
10
20
30
40
50
60
70
1
2
3
4
5
6
7
8
9
10
Data points

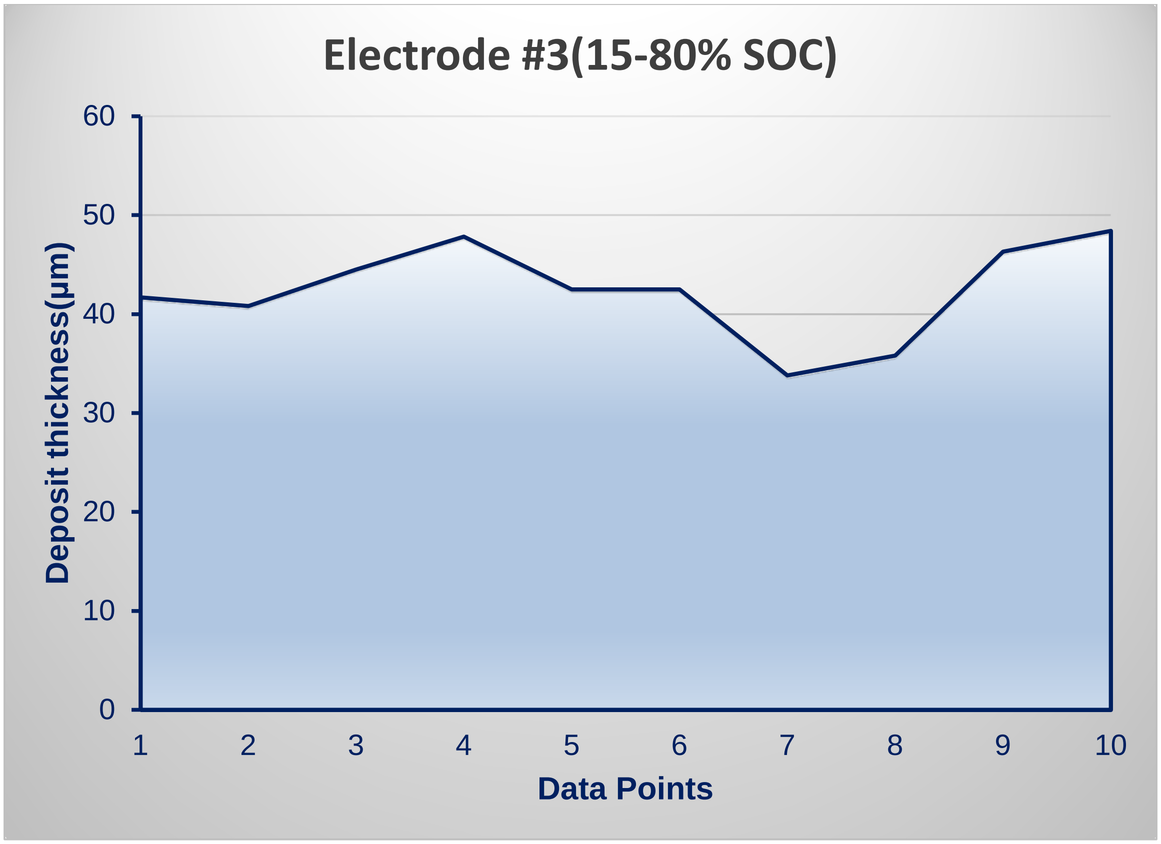
Electrode #3(15-80% SOC)
Deposit thickness(µm)
0
10
20
30
40
50
60
1
2
3
4
5
6
7
8
9
10
Data Points

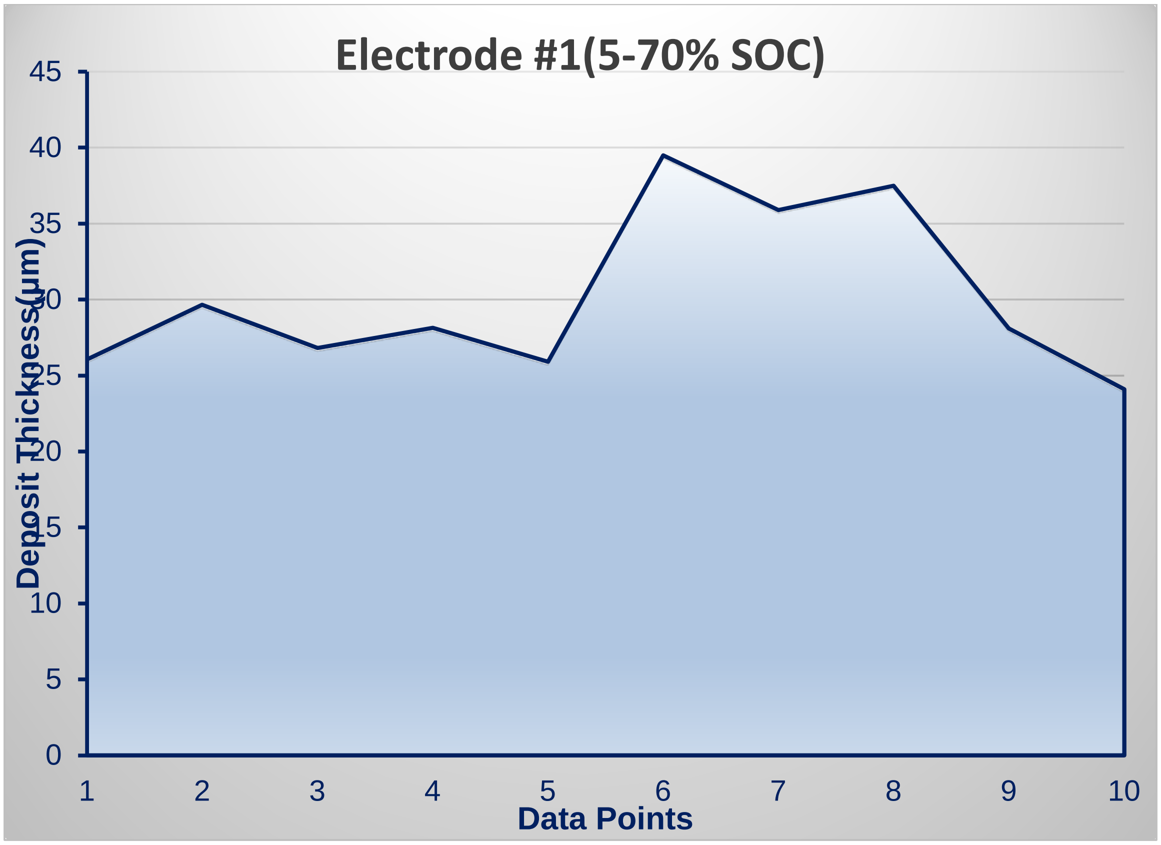
Electrode #1(5-70% SOC)
Deposit Thickness(µm)
0
5
10
15
20
25
30
35
40
45
1
2
3
4
5
6
7
8
9
10
Data Points

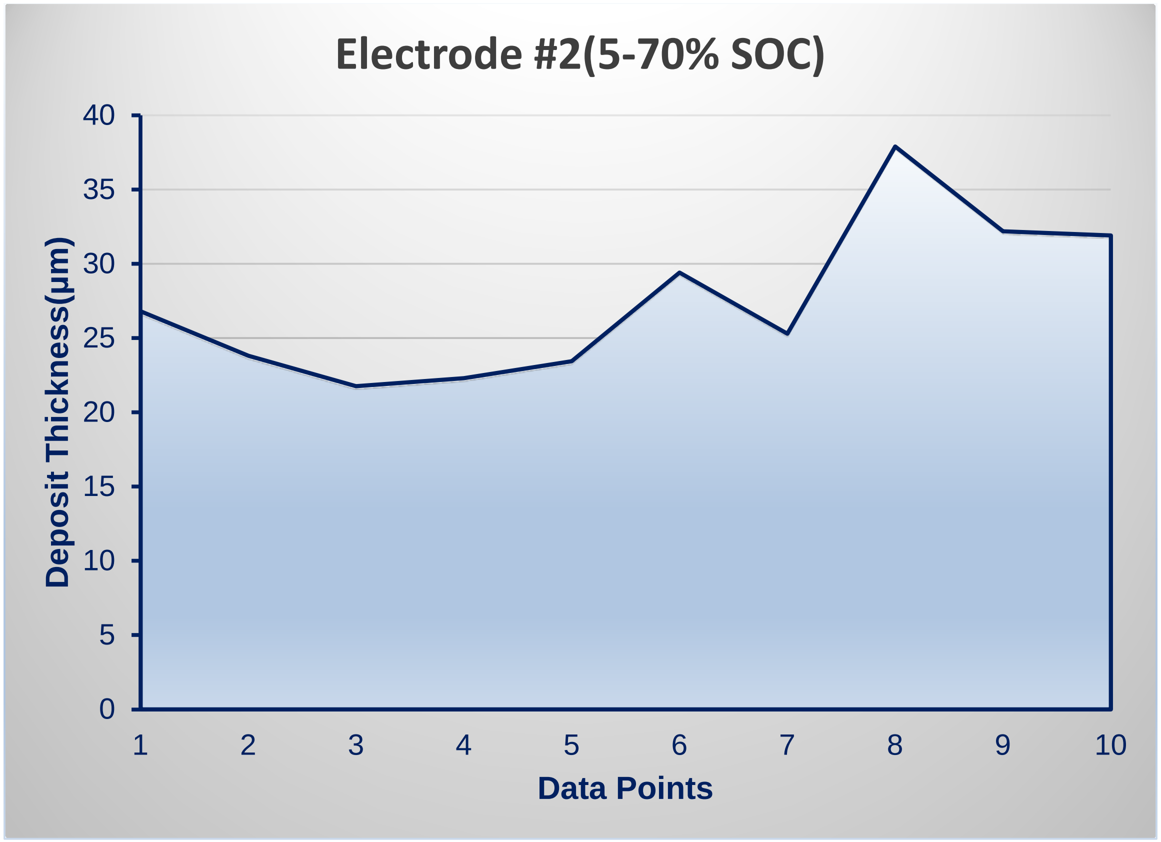
Electrode #2(5-70% SOC)
Deposit Thickness(μm)
40
35
30
25
20
15
10
5
0
1
2
3
4
5
6
7
8
9
10
Data Points

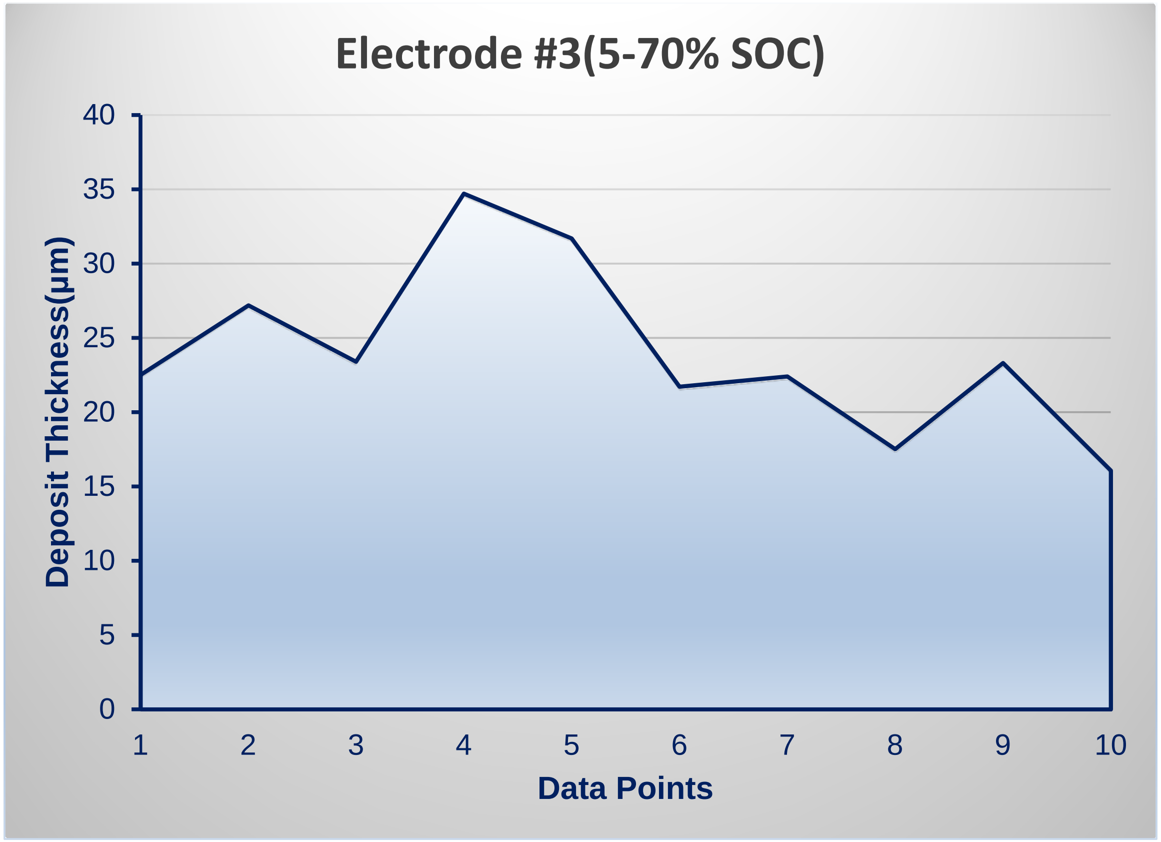
Electrode #3(5-70% SOC)
Deposit Thickness(μm)
40
35
30
25
20
15
10
5
0
1
2
3
4
5
6
7
8
9
10
Data Points